

Studies of Hard Scattering in Photoproduction at the *ep* Storage Ring HERA with the H1 Detector

DISSERTATION

zur Erlangung des Doktorgrades
des Fachbereichs Physik
der Universität Hamburg

vorgelegt von

Armen Bouniatian

aus Yerevan

Hamburg
1995

Gutachter der Dissertation:

Prof. Dr. G. Heinzelmann
Prof. Dr. B. Naroska

Gutachter der Disputation:

Prof. Dr. E. Lohrmann
Prof. Dr. B. Naroska

Datum der Disputation:

6. Dezember 1995

Sprecher des Fachbereichs Physik und
Vorsitzender des Promotionsausschusses:

Prof. Dr. B. Kramer

Abstract

This thesis presents the analysis of hard interaction processes in quasi-real photoproduction. The data have been recorded with the H1-detector at electron-proton collider HERA in 1993. The analysis used an integrated luminosity of about 290 nb^{-1} . The results correspond to a kinematical range $Q^2 < 0.01 \text{ GeV}^2$, $0.25 < y < 0.7$ and $150 < \sqrt{s_{\gamma p}} < 250 \text{ GeV}$.

The inclusive jet differential cross-section has been measured as a function of jet transverse energy, E_T^{jet} , and pseudorapidity, η^{jet} . Leading order QCD Monte-Carlo calculations, which include both resolved and direct photon processes, initial and final state leading logarithm parton showers, and additional interactions of spectator partons in the resolved photon-proton collisions, describe in general the shape and magnitude of the measured η^{jet} and E_T^{jet} distributions.

Events with no hadronic energy flow in a large interval of pseudorapidity in the proton direction have been observed in photon-proton interactions. These events are interpreted as photon diffractive dissociation. In these events features which can be attributed to hard parton scattering have been found, namely production of high p_T particles and jets. Results are compared with Monte-Carlo calculations which assume hard scattering between partons in the photon and in the Pomeron.

Kurzfassung

In dieser Arbeit wird eine Analyse harter Prozesse in quasi-realer Photoproduktion beschrieben. Die Daten wurden mit dem Detektor H1 am Elektron-Proton Speicherring HERA im Jahre 1993 genommen. Die verwendeten Daten stammen von einer integrierten Luminosität von ca. 290 nb^{-1} , und liegen in den kinematischen Bereichen $Q^2 < 0.01 \text{ GeV}^2$, $0.25 < y < 0.7$, und $150 \text{ GeV} < \sqrt{s_{\gamma p}} < 250 \text{ GeV}$.

In inklusiver Weise wurde der differentielle Jet Wirkungsquerschnitt als Funktion der transversalen Energie, E_T^{jet} , und der Pseudorapidität, η^{jet} , gemessen. Die Simulation einer QCD Störungsrechnung in führender Ordnung, unter Berücksichtigung von aufgelösten und direkten Photon Prozessen, von Anfangs- und Endzustandsstrahlung in Form von Partonschauern in führenden logarithmischen Termen, sowie von weiteren Wechselwirkungen der Spektatorpartonen in den aufgelösten Photon-Proton Kollisionen, beschreiben im allgemeinen Form und Größe der gemessenen E_T^{jet} und η^{jet} Verteilungen der Jets.

Wir finden auch eine Unterklasse von Ereignissen die gekennzeichnet ist durch das Fehlen jeglichen Energieflusses in einem großen Pseudorapiditäts Intervall in Richtung des auslaufenden Protons. Diese Ereignisse werden als diffraktive Dissoziation von Photonen an elastisch gestreuten Protonen interpretiert. In ihnen beobachten wir kinematische Eigenschaften, die harten Parton Streuprozessen zugeordnet werden können, nämlich die Erzeugung von Teilchen mit großem p_T , und von Jets. Die gemessenen Verteilungen werden mit der Simulation einer angenommenen harten Streuung zwischen Partonen aus dem Photon und dem Pomeron verglichen.

Contents

1	Introduction	3
2	HERA and the H1 detector	5
2.1	Electron–proton collider HERA	5
2.2	The H1-detector	7
2.2.1	Tracking	8
2.2.1.1	Drift chambers	8
2.2.1.2	Proportional chambers	10
2.2.1.3	Scintillators	11
2.2.2	The liquid argon calorimeter	11
2.2.3	The backward electromagnetic calorimeter	12
2.2.4	Luminosity system	13
3	Theoretical Overview	16
3.1	Kinematics of electron–proton scattering	16
3.2	Deep inelastic scattering	18
3.3	Physics with almost real photons	19
3.3.1	Photon–proton interactions	21
3.3.2	Inclusive jet cross–section	24
3.4	The photon structure function	28
3.5	Hard interactions in photon diffractive dissociation processes	32
3.6	Monte–Carlo models	36
3.6.1	PYTHIA	36
3.6.2	PHOJET	38
3.6.3	HERWIG	39
3.6.4	POMPYT	40

4	The Data Sample	42
4.1	Trigger	43
4.1.1	L1-trigger	44
4.1.2	L4-trigger or Filter farm	47
4.2	Reconstruction and event classification	49
4.3	Final selections	51
4.4	Background	53
5	Measurement of the Inclusive Jet Cross-Section in Photoproduction	56
5.1	Jet algorithm	56
5.2	Event sample	58
5.3	Jet shapes	60
5.4	The measurement of the inclusive jet cross-section	67
5.4.1	Trigger efficiency	68
5.4.2	Corrections	68
5.4.3	Systematic errors	70
5.4.4	Results and discussions	73
5.5	Conclusions	83
6	Observation of Hard Processes in Diffractive Scattering in Photoproduction	86
6.1	Rapidity gap events	86
6.2	Jets in rapidity gap events	95
6.3	Conclusions	102
7	Summary	103

Chapter 1

Introduction

Lepton–proton experiments have played a major role in our understanding of the structure of matter for the last 30 years. At the end of the sixties experiments with electron beams on proton targets performed at SLAC revealed that the proton had an internal structure [1]. It was suggested that the proton consists of pointlike objects, called partons [2]. The discovery of the partonic structure of nucleons and the subsequent observation of violation of Bjorken scaling laid solid foundations for the theory of strong interactions of quarks and gluons– quantum chromodynamics (*QCD*) [3].

The process of probing the internal structure of the proton with lepton beams, termed deep inelastic scattering (*DIS*), remains an essential tool for studying the partonic substructure of nucleon and for a reliable test of QCD. The first electron-proton collider in the world– HERA¹, where 26.7 *GeV* electrons collide with 820 *GeV* protons yielding an *ep* centre of mass (*CMS*) energy of about 300 *GeV*, opens a completely new kinematical domain to study deep inelastic scattering. Four–momentum transfer Q^2 up to 10^5 GeV^2 and x values down to about 10^{-4} at moderate Q^2 can be reached. Compared to fixed target experiments, this is an extension of the kinematical domain by almost two orders of magnitude in both x and Q^2 .

One of the main physics issues accessible with HERA is the study of photon-proton interactions at $Q^2 \approx 0$ over a wide centre of mass energy range of $\sqrt{s_{\gamma p}} \cong 60 - 270 \text{ GeV}$. This is one order of magnitude larger than the CMS energies achieved so far in fixed target experiments. Due to this increase in CMS energy hard scattering in photon–proton collisions becomes clearly visible. This leads to the production of jets, which can be used for detailed QCD tests and to derive information on the partonic structure of the photon, and in particular on its gluon content, about which very little is known at present. At these energies high mass diffractive dissociation processes in photoproduction can be studied as well. In addition, heavy quark flavours are expected to be copiously produced in photoproduction interactions, leading to an additional field of interest at HERA.

The studies of jet production in hard photon–proton interactions and search for hard processes in photon diffractive dissociation are the subjects of the present work. These analyses are based on the data collected in 1993 with the H1–detector.

¹Hadron-Electron-Ring-Anlage

In the chapter 2 the HERA machine and the H1-detector are briefly described. The theoretical overview of photon-proton interactions and the Monte-Carlo models used in analyses are presented in chapter 3.

The selection of a photoproduction event sample is described in chapter 4. Chapter 5 presents the measurements of the inclusive jet cross-section, and chapter 6 the analysis of the hard processes in the photon diffractive dissociation.

Chapter 2

HERA and the H1 detector

2.1 Electron–proton collider HERA

HERA is an electron-proton collider built at the DESY laboratory in Hamburg. The tunnel for HERA is situated 10 to 25 m under the surface of the earth. Two different magnet system (one superconducting and one conventional) guide the proton and electron beams respectively around separate storage rings 6.3 km in circumference. During the 1993 running period collisions of electrons and protons with energies 26.7 and 820 GeV resulted in a centre of mass energy of $\sqrt{s} = \sqrt{4E_e E_p} \approx 295 GeV$. This is equivalent to a 45 TeV electron beam impinging on a fixed target. The beams cross at four interaction regions, at two of them the experiments *H1* [4] and *ZEUS* [5] are placed.

Beam injection into HERA is done in several steps involving several pre-accelerators (see Fig.2.1). In HERA electrons and protons are accelerated and stored in two independent rings. In total, 1170 main dipole and quadrupole warm magnets are guiding the electrons and 646 superconducting magnets the protons. The bunch sizes are kept small in order to achieve high luminosity. The bunch length is about 1 cm for electrons and about 11 cm for protons. The designed beam width and height are about 0.27 mm and 0.036 mm respectively for electrons and about 0.27 mm and 0.08 mm for protons [6].

In 1993 HERA operated with 84 electron and 84 proton colliding bunches with a bunch spacing between crossing of 96 ns . In addition, there were 10 unpaired electron and 6 unpaired proton bunches. These *pilot* bunches are useful for measuring backgrounds due to the collision of an electron or proton with residual gas in the beam-pipe (beam-gas interactions) or with the beam-pipe wall (beam-wall interactions). The average beam currents were $\sim 7.7 mA$ for the electrons and $\sim 10.8 mA$ for the protons. The maximal achieved luminosity was $\sim 1.3 \times 10^{30} cm^{-2}s^{-1}$. The total integrated luminosity produced by HERA in 1993 was about 1 pb^{-1} .

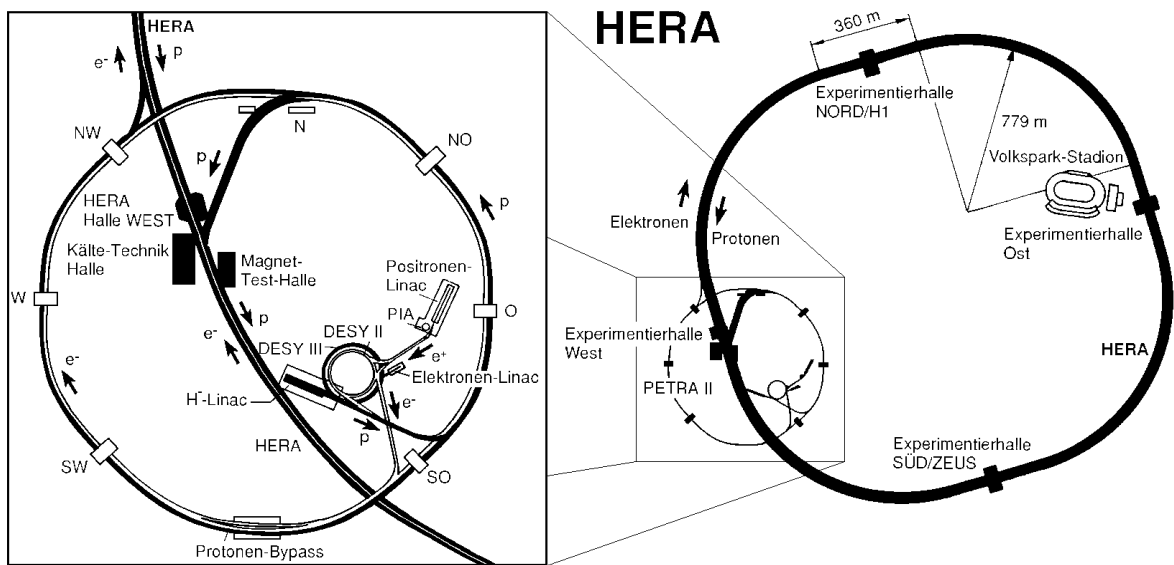


Figure 2.1: Electron-proton collider HERA.

2.2 The H1-detector

The H1 detector is designed to provide clear identification and precise measurement of electrons, muons and neutral particles together with very good performance in the measurement of jets with high particle densities. The main subsystems of the H1 detector are shown in Fig.2.2. In the H1-coordinate system the centre corresponds to the nominal ep interaction point, the z axis points in the proton beam direction, hereafter referred to as the forward, and the x axis is horizontal, pointing towards the centre of HERA.

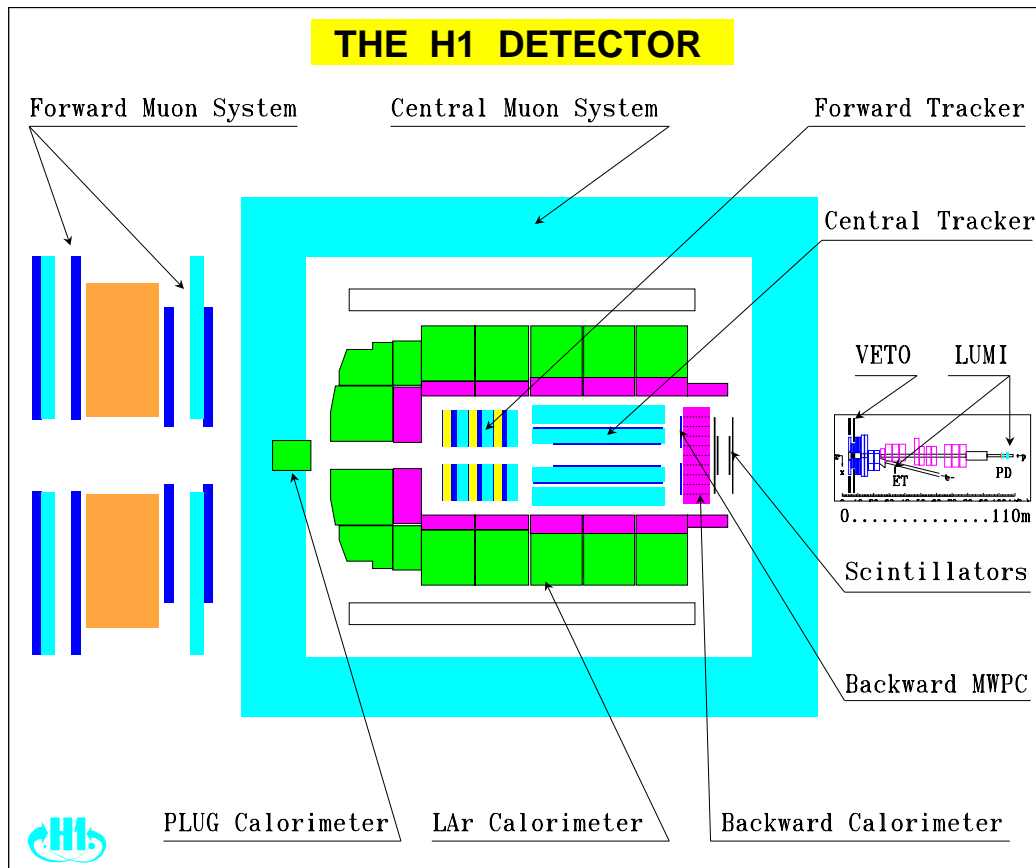


Figure 2.2: The H1 detector.

The tracking part of detector consists of a central and a forward tracking system, each containing different layers of drift chambers and trigger proportional chambers. The tracking region is surrounded by a fine grained liquid argon calorimeter consisting of an electromagnetic section with lead absorber and a hadronic section with steel absorber. A superconducting cylindrical coil with a diameter of 6 m and a length of 5.75 m provides the analyzing field of 1.15 T. A small calorimeter in the proton direction (PLUG) with copper absorber and silicon pad readout covers the region between the beam-pipe and the

liquid argon cryostat ($\theta < 4^\circ$). The lead scintillator backward electromagnetic calorimeter (BEMC) located in the electron direction behind the tracker covers $151^\circ < \theta < 177^\circ$. The iron return yoke of the magnet is laminated and filled with limited streamer tubes, which provide a rough calorimetric measurement of hadronic energy leaking out of the calorimeter (Tail Catcher), as well as identification of muon tracks. The muon tracks in the forward direction are analyzed in a supplementary toroidal magnet sandwiched between drift chambers. A luminosity or electron tagger system is placed at $z = -33.4$ m from the interaction point. The tagger marks the energy of an electron with very small scattering angle indicating photoproduction event. Taken in coincidence with a corresponding photon detector at $z = -102.9$ m upstream from the interaction point, monitors the luminosity by a bremsstrahlung process $ep \rightarrow ep\gamma$. Two scintillator walls in the backward direction are installed to recognize background produced by the proton beam upstream of the H1-detector.

A survey of detector parameters is given in Table 2.1. A detailed description of the H1 detector can be found elsewhere [4]. Below, the parts of the H1 detector which are relevant for the analyses presented here are briefly described. All numbers concerning the subdetector parameters and resolutions are taken from the reference [4].

2.2.1 Tracking

The tracking system of H1 (see Fig.2.3) provides simultaneously triggering, tracking reconstruction and particle identification for the event topology particular to HERA electron-proton collisions. To maintain good efficiency for triggering and reconstruction over the entire solid angle two mechanically distinct tracking detectors have been constructed, the central (CTD) and the forward (FTD) trackers. Each is optimized for tracking and triggering in its angular region. The FTD and CTD are linked together, aligned and installed into the calorimeter cryostat.

2.2.1.1 Drift chambers

Track reconstruction in the central region is based on the two large concentric drift chambers, CJC1 and CJC2, covering the polar angle range $15^\circ < \theta < 165^\circ$. The chambers have wires strung parallel to the beam axes (z -direction). The inner ring consists of 30 segments with 24 sense wires each, while the outer ring is divided into 60 segments equipped with 32 sense wires. A space point is measured with a resolution of $170 \mu\text{m}$ in the drift coordinate ($r\varphi$ plane) and, by charge division measurements, with a resolution of $\sim 1\%$ of the wire length in z . The parameter of tracks are obtained from up to 56 points on track, which are derived from the drift time measurements on different sense wires. Through the magnetic field, only tracks with transverse momentum $\gtrsim 0.15$ GeV will pass through both chambers. The momentum resolutions achieved are $\sigma_p/p^2 \lesssim 0.01$ GeV $^{-1}$ and $\sigma_\theta = 21$ mrad.

Two thin drift chambers, the central inner (CIZ) and central outer (COZ) z -chambers complement the measurement of charged track momenta in the central chambers. The

Calorimetry		
Main calorimeter: liquid Ar	Electromagnetic part	Hadronic part
Granularity	10 to 100 cm^2	50 to 2000 cm^2
Depth (number of channels)	20 to 30 X_0 (30784)	4.7 to 7 λ_{abs} (13568)
Resolution $\sigma(E_{e,h})/E_{e,h}$	$12\%/\sqrt{E_e} \oplus 1\%$	$\approx 50\%/\sqrt{E_h} \oplus 2\%$
Noise per channel	10 to 30 MeV	
Angular coverage	$4^\circ < \theta < 153^\circ$	
Backward calorimeter: Pb-scintillator		
Angular coverage – granularity	$151^\circ < \theta < 177^\circ$	$16 \times 16 cm^2$
Depth – resolution $\sigma(E_e)/E_e$	$22.5 X_0$ ($1 \lambda_{abs}$)	$10\%/\sqrt{E_e} \oplus 2\%$
Tail catcher: iron-streamer tubes		
Angular coverage	$4^\circ < \theta < 177^\circ$	
Depth – resolution $\sigma(E_h)/E_h$	$4.5 \lambda_{abs}$	$100\%/\sqrt{E_h}$
Plug calorimeter: Cu-Si		
Angular coverage – granularity	$0.7^\circ < \theta < 3.3^\circ$	$5 \times 5 cm^2$
Depth – resolution $\sigma(E_h)/E_h$	4.25λ ($44.6 X_0$)	$\approx 150\%/\sqrt{E_h}$
Electron tagger: Tl(Cl/Br)		
Angular coverage – granularity	$\theta > 179.7^\circ$	$2.2 \times 2.2 cm^2$
Depth – resolution $\sigma(E_e)/E_e$	$21 X_0$	$\approx 10\%/\sqrt{E_e} \oplus 1\%$
Tracking		
Coil: radius – field	$3 m - B = 1.15T, \Delta B/B \leq 2\%$	
Central tracking		
Angular – radial coverage	$25^\circ < \theta < 155^\circ$	$150 < r < 850 mm$
Jet chamber: spatial resolution	$\sigma_{r\varphi} = 170 \mu m$	$\sigma_z = 22.0 mm$
z -chambers: spatial resolution	$\sigma_{r\varphi} = 25$ and $58 mm$	$\sigma_z \approx 350 \mu m$
Momentum resolution	$\sigma_p/p^2 < 0.01 GeV^{-1}$	
Forward tracking		
Angular – radial coverage	$7^\circ < \theta < 25^\circ$	$120 < r < 800 mm$
Spatial resolution	$\sigma_{r\varphi} = 170 \mu m$	$\sigma_{x,y} = 210 \mu m$
Backward tracking		
Angular coverage – resolution	$155^\circ < \theta < 175^\circ$	$\sigma_{x,y} = 1 mm$
Trigger proportional chambers		
Angular coverage – channels	$7^\circ < \theta < 175^\circ$	3936
Muon detection		
Instrumented iron		
Angular coverage	$4^\circ < \theta < 171^\circ$	
Spatial resolution	$\sigma_{wire} = 3 - 4 mm$	$\sigma_{strip} = 10 - 15 mm$
Angular – momentum resolution barrel	$\sigma_\theta(\sigma_\varphi) = 15 mr$	$\sigma_p/p \approx 0.35$
Forward muon toroid		
Angular coverage – resolution	$3^\circ < \theta < 17^\circ$	$0.25 < \sigma_p/p < 0.32$
Overall size (x, y, z) – weight	$12 \times 15 \times 10 m^3$	2800t

Table 2.1: Summary of the H1-detector parameters. Energies are given in GeV .

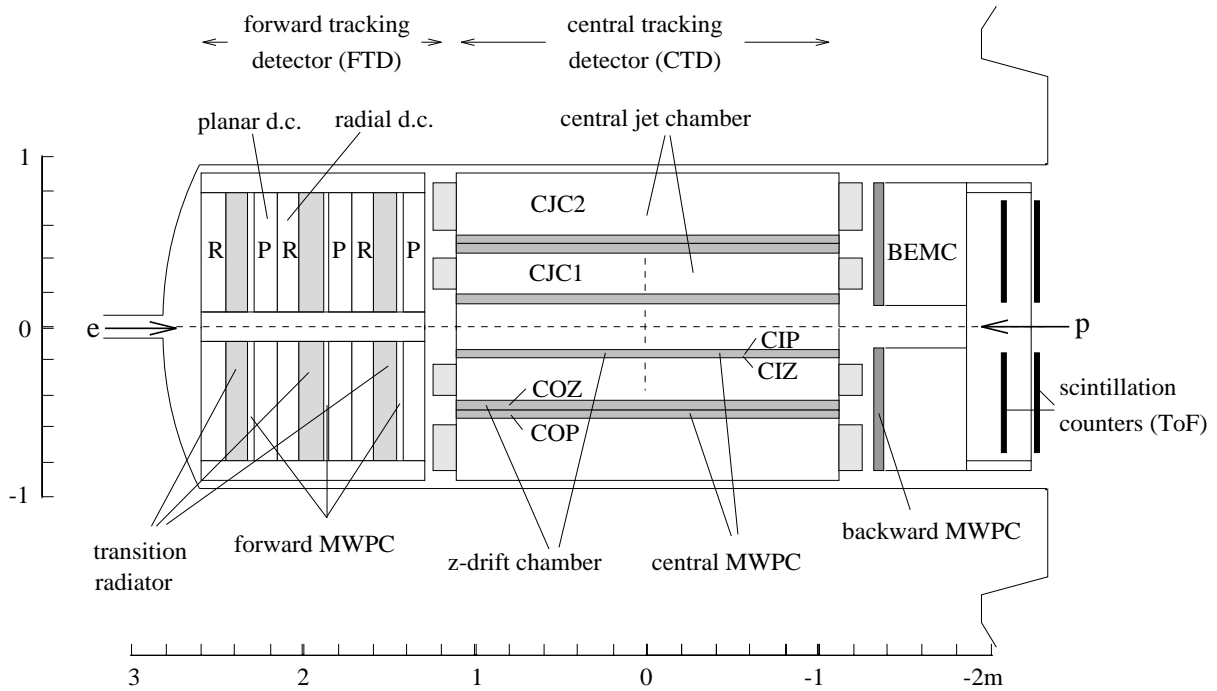


Figure 2.3: The side view of H1 tracking detectors.

CIZ chamber fits inside CJC1, and the COZ chamber fits in between CJC1 and CJC2. The sense wires are strung perpendicular to the beam axis. These two chambers deliver track elements with typically $300 \mu\text{m}$ resolution in z and $1\text{--}2\%$ of 2π in φ . Linking these track elements to those obtained from the jet chamber with accurate $r\varphi$ and moderate z -information gives the final accuracy on both the longitudinal as well as the transverse momentum components.

The forward tracking detector (FTD) provides an accurate measurement of charged particles in the forward direction $5^\circ < \theta < 30^\circ$, track information on individual particles within jets by means of transition radiation detection and a fast forward ray track trigger. It consists of three supermodules. Each supermodule includes three different orientations of planar wire drift chambers designed to provide accurate θ measurements, a multiwire proportional chamber (FWPC) for fast triggering, a passive transition radiator and a radial wire drift chamber which provides accurate $r\varphi$ (drift coordinate) information. The planar chambers contain parallel wires and provide homogeneous spatial resolution in the plane perpendicular to the beam direction, whereas in the radial chambers the wires radiate outwards from the beam pipe— all wires being strung perpendicular to the beam direction, and serve for precise momentum measurement.

2.2.1.2 Proportional chambers

Between 5° and 175° the solid angle seen from the interaction region is covered by multiwire proportional chambers. Six independent planes in the forward direction (FWPC) (see Fig.2.3), four in the central (CIP and COP) and four in the backward direction (BPC)

deliver a fast timing signal with a time resolution better than the separation of two succeeding HERA bunch crossings and provide moderately accurate space points for charged particle track reconstruction at the first level trigger. The backward region between 155° and 175° is covered by the backward multiwire proportional chamber (BPC), which has four different orientations of anode wire planes. The combination of 3 or 4 wires is used for space-point reconstruction with angular resolution of 0.5 mrad . The planar forward chambers (FWPC) are interspaced between the different forward drift chambers and are exposed to high particle rates increasing towards the beam pipe. The inner central proportional chamber (CIP) is closest to the interaction region and covers the largest solid angle. Since the main purpose of the FWPC, COP and CIP is to provide space points for the first level trigger, a pad segmented cathode readout was chosen. From the reconstructed tracks the event vertex is deduced. In order to remove background hits from uncorrelated noise and synchrotron radiation the trigger logic requests three or four space points per track (see also section 4.1.1).

2.2.1.3 Scintillators

Two scintillator arrays are located in the backward region (see Fig.2.2-2.3) and used to reject proton beam associated background at the first trigger level. The time of flight device (TOF) is located upstream of the interaction region, behind the backward electromagnetic calorimeter BEMC, at $z \approx -2 \text{ m}$, and consist of two scintillator hodoscope planes, sandwiched between $1 X_0$ (radiation length) of lead to absorb synchrotron radiation. The signals from photomultipliers are discriminated and strobed in three time windows: background, interaction and global, which are used in the first level trigger decision. The device as a whole has a resolution of 4 ns , while individual counters have a resolution of the order of 2 ns . Particles from proton induced background and from $e p$ collisions are separated in time by $\sim 13 \text{ ns}$.

In addition to the TOF device two double scintillator veto walls are installed at a distance of 6.5 and 8.1 m upstream from the interaction point. The smaller inner veto wall covers the near beam area ($100 \times 90 \text{ cm}^2$) down to a radius of 11 cm . Penetrating particles are then identified in coincidences between two scintillators with a time resolution of $\pm 3 \text{ ns}$. The large outer veto wall with an area of about $5 \times 4 \text{ m}^2$ overlaps the inner veto wall and nearly all of the liquid argon calorimeter. An iron wall of 5 cm thickness separates all scintillator pairs of the outer wall. The coincidence resolution of such pairs is $\pm 8 \text{ ns}$.

2.2.2 The liquid argon calorimeter

The liquid argon calorimeter (LAr) surrounds the tracker and covers the polar angular range between 4 and 153° . The liquid argon calorimeter is segmented into an electromagnetic part and a hadronic part and placed inside the magnet. This allowed to minimize both the amount of dead material in front of the electromagnetic calorimeter for optimal energy resolution and the overall size of the calorimeter. The total thickness of the electromagnetic calorimeter varies between 20 and 30 radiation lengths (X_0), the total depth

of the calorimeter varies between 4.5 and 8 interaction lengths (λ), depending on polar angle.

The segmentation along the beam axis is in eight “wheels” (see Fig.2.2). One single large cryostat houses all wheels. Each of the six barrel wheels is segmented in φ into eight identical “stacks”. The two forward wheels are each mechanically assembled as two half rings. Each stack in turn is divided into an electromagnetic section with lead as absorber material, starting at a radius of 86 cm, followed by a hadronic section made of welded stainless steel absorber plates with independent read-out cells inserted between the plates. All z cracks (boundaries between the different wheels) are perpendicular to the beam axis. The electromagnetic part has φ cracks (boundaries between stacks within a wheel) pointing to the interaction point, and the φ cracks in subsequent hadronic sections are inclined in φ and therefore guarantee a hermetic calorimeter. The gaps between the absorber plates are equipped with highly segmented read-out structures. The granularity of the read-out cells is based on the requirement of good separation of electromagnetic and hadronic showers. A total of 45000 read-out channels result for the entire LAr calorimeter, out of which 30800 are situated in its electromagnetic part. Typical noise levels in the readout channels are between 10 and 30 MeV, depending on the channel capacity.

An extensive calibration program with test beams at CERN using the different types of H1 calorimeter stacks provided the basic calibration constants for the calorimeter [7]. The energy resolution $\sigma(E)/E$ obtained for electrons is between 10% and 13%/ \sqrt{E} (E in GeV) with a constant term below 1%. The H1 LAr calorimeter is non compensating. The response for hadrons is about 30% less than for electrons. Therefore an additional correction has to be applied to the signal obtained on the electromagnetic scale. The obtained energy resolution for hadrons is about 50%/ \sqrt{E} with a constant term below 2%. These results have been basically confirmed at HERA using cosmic rays and deep inelastic scattering events. The absolute scales of the energy response have been verified with charged particles by comparing their momentum measured in the central tracker with the associated energy deposited in the calorimeter. The deep inelastic scattering events where the scattered electron and the hadronic jet are detected both in the LAr calorimeter were used for a direct comparison of the hadronic and electromagnetic energy measurement exploiting p_T balance. These analyses established that the overall hadronic energy scale and resolution are understood to within $\pm 5\%$ and $\pm 10\%$ respectively.

2.2.3 The backward electromagnetic calorimeter

The backward ($-z$) region of the H1 detector is instrumented with an electromagnetic lead-scintillator sandwich calorimeter. The calorimeter elements (stacks) of the BEMC are mounted in an aluminum barrel with a diameter of 162 cm. Together with the central tracking system the barrel rests on rails mounted on the inner wall of the liquid Argon cryostat. The BEMC is located at a distance of 144 cm from the nominal interaction point. Scattering angles θ from 150° to 177° are covered with full azimuthal acceptance. The acceptance of the rear part of the liquid argon calorimeter sets in at 153° so that an almost continuous transition between the two calorimeter types is achieved. BEMC

consists of 88 calorimeter stacks aligned parallel to the beam line, each with a depth of $22.5 X_0$, corresponding to one hadronic absorption length. 56 stacks have a quadratic cross-section of 16 by 16 cm^2 . The remaining ones are of trapezoidal and triangular shapes. Each stack is read out by four PIN photodiodes.

The energy resolution of the BEMC for electromagnetic showers has been determined as $\sigma(E)/E \sim 10\%/\sqrt{E}$ with a constant term of 4%. From an analysis of DIS events an uncertainty in the absolute energy scale of about 2% has been derived. Interacting hadrons deposit typically 30% of their energy in the BEMC. About 30% of all hadrons do not interact in the calorimeter. A satisfactory hadronic resolution of $\sim 80\%/\sqrt{E}$ has been achieved. The hadronic energy scale in the BEMC is assumed to be known to 50%.

2.2.4 Luminosity system

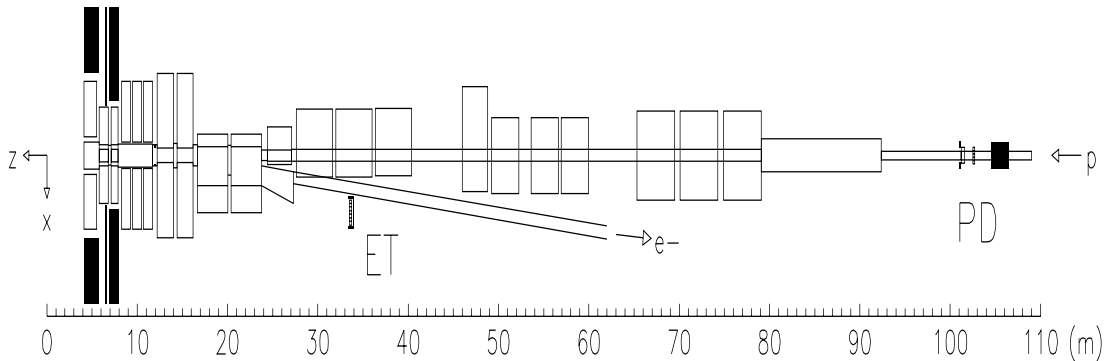


Figure 2.4: H1-luminosity system.

The luminosity system serves several purposes. Its main task is a fast relative luminosity measurement. It also provides electron beam monitoring for the HERA machine, absolute luminosity measurement in the interaction region, tagging of photoproduction events and energy measurement for electrons scattered under small angles and for photons from initial state radiation. The luminosity is determined from the rate of Bethe-Heitler events $ep \rightarrow ep\gamma$ [9]. The main source of background is bremsstrahlung from the residual gas in the beam pipe, $eA \rightarrow eA\gamma$. At design luminosity these events are expected at 10% of the $ep \rightarrow ep\gamma$ rate, but can be subtracted using data from electron pilot bunches. The luminosity is calculated as

$$L = \frac{R_{tot} - (I_{tot}/I_0)R_0}{\sigma_{vis}}$$

where R_{tot} is the total rate of the bremsstrahlung events, R_0 is the rate in the electron pilot bunches, I_{tot} , I_0 are the corresponding electron beam currents and σ_{vis} is the visible part of the $ep \rightarrow ep\gamma$ cross-section with acceptance and trigger efficiency included.

The luminosity monitor detects scattered electrons and outgoing photons in coincidence. It contains therefore two arms: the electron detector (often called electron tagger-ET) and the photon detector (PD). The general view of the luminosity system is shown in Fig. 2.4. Scattered electrons are deflected by a set of quadrupoles and a bending magnet located in the region $-23.8 < z < -5.8$ m, pass an exit window at $z = -27.3$ m and hit ET at $z = -33.4$ m. The acceptance of the electron detector is defined by the fields in the machine magnets, and thus may vary significantly if the beam optics changed. The actual value of the beam tilt is measured on-line with a precision of 0.01 mrad by reconstructing the average position of the photon spot in the PD.

The photons leave the proton beam pipe through a window at $z = -92.3$ m, where the beam pipe bends upward, and hit PD at $z = 102.9$ m. A Pb filter ($2 X_0$) followed by a water Čerenkov ($1X_0$) veto counter (VC) (not shown in figure) is located in front of the photon detector. The filter protects the detector from the high synchrotron radiation flux. VC serves primarily as a veto counter (to tag and reject early photon showers), but also provides a rough energy measurement, which is combined with the energy measurement in the PD crystals. From the p -beam side PD is shielded by an iron wall of 2 m thickness. The aperture of the photon detector is $\lesssim 0.45$ mrad, limited by the inner diameter of a lead collimator. This corresponds to an acceptance of $\approx 98\%$ for bremsstrahlung photons, which varies only slightly with changes of the beam optics.

The parameters of the luminosity system are given in the Table 2.2.

	unit	ET	PD
Energy interval, $E_\gamma/E_e = 1 - E_{e'}/E_e$		0.2 – 0.8	0.004 – 1.0
Polar angle acceptance interval	mr	0 – 5	0 – 0.45
Average acceptance for $ep \rightarrow ep\gamma$	%	48	98
Average acceptance for photoproduction	%	36	–
σ_{vis}	mb	28	174
Aperture $x \times y$	mm ²	154×154	100×100
Granularity		7×7	5×5
Chemical composition		TiCl(78%) + TiBr(22%)	
Crystal length	cm	20	
Energy resolution, $\sigma(E)/E$		$10\%/\sqrt{E} \oplus 1\%$, (E in GeV)	
Position resolution, $\sigma_{x,y}$	mm	0.3 – 1.2	
Time resolution, σ_t	ns	< 3	

Table 2.2: Parameters of the luminosity system.

Since the luminosity detectors operate at high rates up to few MHz, which may vary within one beam filling by a factor of 3 to 10, they are permanently calibrated during data taking using the energy constraint $E_{ET} + E_{PD} = E_{e-beam}$. This method allows an absolute calibration with a precision of better than 1%. A final absolute measurement of the integrated luminosity used for physics analysis requires a precise absolute energy

calibration and detailed understanding of the acceptances of the luminosity detectors, and is performed off-line. The major contribution to the systematic errors of the absolute luminosity measurement comes from the $\sim 3\%$ uncertainty in the electron detector acceptance, which is determined off-line using the data sample which is independent on the electron detector and is insensitive to the possible variations of the beam optics [9]. The accuracy of the absolute luminosity measurement in 1993 was estimated to be $\lesssim 5\%$.

Chapter 3

Theoretical Overview

3.1 Kinematics of electron–proton scattering

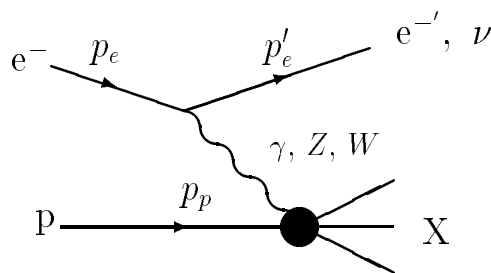


Figure 3.1: The diagram of electron–proton scattering.

Inclusive electron–proton scattering $ep \rightarrow e'X$ (Fig.3.1) can be described by three variables: s , Q^2 and x . s is the square of the centre of mass energy; Q^2 is the square of the four-momentum transfer; and x , the Bjorken scaling variable, in the parton picture is the momentum fraction carried by the struck quark inside the proton. Other variables which are used for the description of the electron-proton scattering processes are y – the ratio of the electron energy transferred to the hadronic system to the total electron energy in the rest frame of the proton, and W – the invariant mass of the hadronic final state. All these variables are uniquely defined in terms of $p_e, p_{e'}$ and p_p (see Fig. 3.1), the four momentum vectors of the incoming and outgoing electron and the incoming proton, respectively:

$$s = (p_e + p_p)^2 \quad (3.1)$$

$$Q^2 = -q^2 = -(p_e - p_{e'})^2 \quad (3.2)$$

$$x = \frac{Q^2}{2p_p \cdot q} \quad (3.3)$$

$$y = \frac{p_p \cdot q}{p_p \cdot p_e} = \frac{Q^2}{s \cdot x} \quad (3.4)$$

$$W^2 = (p_p + q)^2 \quad (3.5)$$

where $q = p_e - p_{e'}$.

If the masses of electron and proton are neglected, then expressions Eq.(3.1-3.5) can be given in terms of E_e – the energy of the incoming electron, $E_{e'}$ and θ' – the energy and angle of scattered electron (with respect to the direction of the incoming proton), and E_p – the energy of the incoming proton.

$$s \approx 4E_e E_p \quad (3.6)$$

$$Q^2 \approx 4E_e E_{e'} \sin^2 \frac{\theta'}{2} \quad (3.7)$$

$$y \approx 1 - \frac{E_{e'}}{E_e} \cos^2 \frac{\theta'}{2} \quad (3.8)$$

$$W^2 \approx Q^2 \frac{1-x}{x} \quad (3.9)$$

The important feature of HERA experiments is the possibility to measure both the scattered electron and the hadronic final state, thus the collision kinematics can be determined from electron variables, hadron variables or a mixture of both. This allows a more precise measurement compared to fixed target experiments. In order to reconstruct kinematics using the final state hadrons the method proposed by F.Jacquet and A.Blondel [10] is used:

$$y_{jb} = \frac{1}{2E} \sum_{hadrons} (E_h - p_{z,h}) \quad (3.10)$$

$$Q_{jb}^2 = \frac{1}{1 - y_h} \sum_{hadrons} (p_{t,h})^2 \quad (3.11)$$

Here E_h is the energy of a hadron and $p_{z,h}$ ($p_{t,h}$) its momentum component along (transverse) to the proton direction.

HERA covers the kinematical range of the electron-proton scattering from $Q^2 \approx 10^{-8} \text{ GeV}^2$ to $\approx 10^5 \text{ GeV}^2$. In the processes with large Q^2 ($Q^2 \gtrsim 4 \text{ GeV}^2$) the scattered electron is seen in the H1-calorimeters (LAr or BEMC). In the following, these events are called “*deep inelastic scattering*” or “*DIS*”. In contrast to DIS events, in processes with $Q^2 \lesssim 4 \text{ GeV}^2$ (we will call them “*photoproduction*”) the scattered electron has a very small angle with respect to the beam-line, and thus most of the time is lost in the beam-pipe. However, in some cases the scattered electrons can be detected in the electron detector of the luminosity system, which is located $\sim 33 \text{ m}$ down the electron beam-line (see section 2.2.4). For this class of events, henceforth called “*tagged photoproduction*”, the virtuality of the quasi-real photon is $3 \times 10^{-8} < Q^2 < 10^{-2} \text{ GeV}^2$. Only the tagged events are subject of the present analysis.

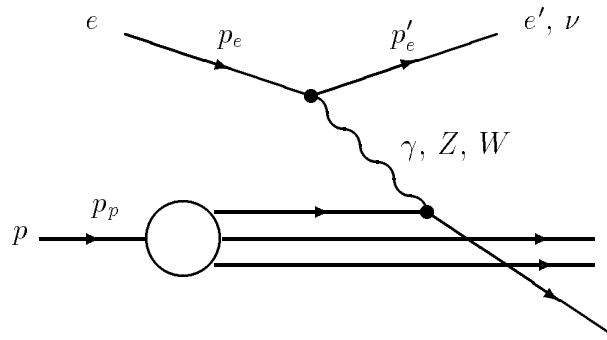


Figure 3.2: Deep inelastic electron–proton scattering.

3.2 Deep inelastic scattering

In the simple quark-parton model (*QPM*) of deep inelastic scattering (Fig.3.2), a quark, which carries a fraction x of the proton momentum, is scattered out of the proton by the interaction with a virtual boson (γ, Z^0 or W^\pm) emitted from the scattering lepton. In QPM there are no strong interactions between the quarks, and the proton structure function depends only on Bjorken- x (so called *scaling*). Processes which proceed through the exchange of a neutral boson are called *neutral current (NC)* reactions, whereas the exchange of a charged boson is called a *charged current (CC)* reaction. In this picture the partonic final state contains two objects, namely the scattered quark and the proton remnant. The proton remnant consists of two quarks and doesn't take part in the interaction. Quantum chromodynamics *QCD*– the gauge theory of strong interactions– modifies this naive picture including in the model gluons as gauge bosons of the strong interaction. It allows for gluon radiation from the quark before and after the boson–quark vertex. Virtual bosons can also interact with gluons inside the proton (boson–gluon fusion).

QCD describes the hadron substructure seen in deep inelastic scattering by distribution functions $q_i(x, Q^2)$, which give the probability for finding a parton $i = u, d, s, g, \dots$ with momentum fraction x in the hadron when probed at a scale Q^2 . In this approach the structure function is a sum of the contributions of all quarks and antiquarks:

$$F_2(x, Q^2) = \sum_i x e_i^2 q_i(x, Q^2) \quad (3.12)$$

For momentum transfer small compared to the mass of the Z^0 – and W^- –bosons the cross–section of electron–proton scattering can be expressed in terms of the proton structure function $F_2(x, Q^2)$:

$$\frac{d^2\sigma}{dx dQ^2} = \frac{2\pi\alpha^2}{Q^4 x} \left[2(1-y) + \frac{y^2}{1+R} \cdot F_2(x, Q^2) \right] \quad (3.13)$$

where $R = \sigma_L/\sigma_T$ is the ratio of cross-sections of the longitudinally to the transversely polarized virtual boson.

At present stage QCD does not supply information on the parton distribution functions inside the nucleons, but it predicts the Q^2 evolution of the structure functions. Until now mostly the Dokshitzer–Gribov–Lipatov–Altarelli–Parisi (DGLAP) QCD evolution equations [11] have been used to study and successfully interpret the Q^2 evolution of the available deep inelastic data from fixed target experiments, which are essentially limited to the region $x > 10^{-2}$. The high centre of mass energy of about $\sqrt{s} \approx 300 \text{ GeV}$ at HERA allows extending the kinematical range for Q^2 up to 10^5 GeV^2 and for Bjorken- x down to 10^{-4} . Due to the photon propagator in the scattering amplitude (see Eq.(3.13)) the majority of DIS events are at low Q^2 and low x . It is expected that at low x region the linear DGLAP evolution equation has to be replaced by non-linear Balitskii–Kuraev–Fadin–Lipatov (BFKL) equations [12] as the parton density rises strongly in the transition region between the perturbative and non-perturbative regimes. One important experimental input to these studies is the measurement of structure function F_2 in the low x ($< 10^{-2}$) region at HERA energies, for which extrapolations from the low energy measurements are available, using DGLAP evolution equations. H1 and ZEUS provided first measurements of proton structure F_2^p from neutral current DIS in the novel kinematic region [13]. These results confirm the steep rise towards low x values.

The *scaling violation* predicted by perturbative QCD leads to a logarithmic Q^2 -dependence of structure functions due to the gluon emission by quarks. The rise of F_2 with Q^2 can be related to the gluon density $G(x, Q^2)$:

$$G(x, Q^2) \propto \frac{\partial F_2(x, Q^2)}{\partial \ln Q^2} \quad (3.14)$$

Based on this assumption, first measurements of gluonic structure function in proton $G(x, Q^2)$ have been performed [14]. It was found that the gluon distribution rises strongly with decreasing x .

An other important test of QCD is provided by studying the hadronic final states in DIS. Several inclusive and topological measurements of hadronic final states have been used to extract the gluon density of the proton and to get information on the onset of BFKL evolution [15]. Expectations for the properties of hadronic final states are available in the form of Monte Carlo models, which are based on the DGLAP QCD evolution and which were tuned to provide a satisfactory description of low energy data. In the new domain at HERA they differ widely in their predictions, and significant differences between QCD models and the data have already been observed [16].

3.3 Physics with almost real photons

Photoproduction processes at HERA contain a wide spectrum of interesting physics, ranging from soft hadronic physics over hard QCD interactions and electroweak studies to explorations of extensions of the Standard Model.

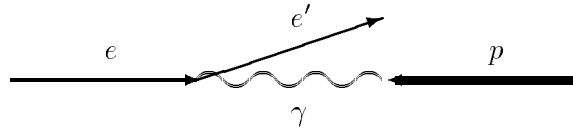


Figure 3.3: γp scattering.

The energy of the quasi-real photon which is emitted by an electron scattered through a small angle (Fig.3.3) is

$$E_\gamma = E_e - E_{e'}, \quad (3.15)$$

where E_e and $E_{e'}$ are the energies of the incoming and outgoing electrons. The acceptance of the electron detector restricts the photon energy to the range $0.2 < y < 0.8$, where $y \approx E_\gamma/E_e$. The total energy of the photon–proton system accessible at HERA is

$$130 \text{ GeV} \lesssim \sqrt{s_{\gamma p}} \approx \sqrt{4y E_e E_p} \lesssim 260 \text{ GeV},$$

about factor 10 higher than in the previous fixed-target experiments.

For small Q^2 an ep interaction can be represented as two subsequent processes: emission of a photon by the electron and interaction of the photon with the proton. The relation between the electron–proton and photon–proton cross–sections is given by the equivalent photon expression [17]:

$$\frac{d^2\sigma^{ep}}{dydQ^2} = \frac{\alpha}{2\pi y Q^2} \left[(1 + (1-y)^2 - 2(1-y)\frac{Q_{min}^2}{Q^2})\sigma_T(y, Q^2) + 2(1-y)\sigma_L(y, Q^2) \right] \quad (3.16)$$

where $Q_{min}^2 = m_e^2 y^2 / (1-y)$, m_e is the mass of the electron and σ_T and σ_L are the photon–proton cross–sections for transversely and longitudinally polarized photons.

In the limit of very small Q^2 ($Q^2 \ll 1 \text{ GeV}$) $\sigma_L \rightarrow 0$ and $\sigma_T \rightarrow \sigma^{\gamma p}$ ($\sigma^{\gamma p}$ is the full photon–proton cross–section). Performing the integration over Q^2 , with Q_{max}^2 given by the experimental conditions, provides the equivalent photon approximation in the form¹:

$$\frac{d\sigma^{ep}}{dy} = Flux(y) \cdot \sigma^{\gamma p} = \frac{\alpha}{2\pi} \left[\frac{1 + (1-y)^2}{y} \ln \frac{Q_{max}^2}{Q_{min}^2} - \frac{2(1-y)}{y} \left(1 - \frac{Q_{min}^2}{Q_{max}^2}\right) \right] \cdot \sigma^{\gamma p} \quad (3.17)$$

where the first term, called *photon flux*, defines the probability to find a photon with the fractional energy y and maximum virtuality Q_{max}^2 in the electron.

The total photoproduction cross–section has been measured by the H1 and ZEUS experiments at a centre of mass energy of about 200 GeV . The measured value is

$$\sigma_{\gamma p} = 165 \pm 2(stat) \pm 11(syst) \mu b \quad \text{at } \langle W_{\gamma p} \rangle = 200 \text{ GeV} \quad \text{for H1 [19]}$$

and

$$\sigma_{\gamma p} = 143 \pm 4(stat) \pm 17(syst) \mu b \quad \text{at } \langle W_{\gamma p} \rangle = 180 \text{ GeV} \quad \text{for ZEUS [20]},$$

where $\langle W_{\gamma p} \rangle$ denotes the average CMS energy of γp collision.

¹If the mass of electron is ignored, then in Eq.(3.17) only the \ln term is kept (Weizsäcker-Williams approximation–“WWA” [18]). Using the WWA, instead of Eq.(3.17), introduces a $\sim 7\%$ underestimate of the photoproduction cross–section [17].

3.3.1 Photon–proton interactions

At HERA the majority of the photoproduction interactions are expected to consist of “*soft*” peripheral collisions, similar to the hadron–hadron interactions. These collisions are characterized by small transverse momenta of produced particles ($p_T \ll 1 - 2 \text{ GeV}$). The dynamics of soft physics is generally regarded to be of a non–perturbative nature and not to be calculable in QCD, but is essentially described by longitudinal phase space.

From previous fixed target experiments we know that the photon does not necessarily interact directly as a gauge boson. It rather exhibits a hadronic type of scattering which is usually expressed in terms of the vector meson dominance (VDM) model [21]. The photon and the vector mesons ($V = \rho(770), \omega(782), \phi(1020), \dots$) have quantum numbers that allow the photon to couple to a vector meson which subsequently interacts with the proton. Hence the photon–proton collisions are expected to follow largely the same phenomenology and produce a final hadronic state very similar to that of hadron–hadron (e.g. πp) collisions. The main aim of the VDM model has been the description of the soft (low p_T) physics. In VDM, the γp cross–section can be expressed as a sum of the corresponding vector meson–proton cross–sections:

$$\sigma_{VDM}^{\gamma p}(s) = \sum_V \left(\frac{4\pi\alpha_{em}}{f_V^2} \right) \sigma^{Vp}(s) \quad (3.18)$$

where the couplings f_V^2 are determined experimentally [21, 22].

$$\frac{f_\rho^2}{4\pi} \approx 2.20 \quad \frac{f_\omega^2}{4\pi} \approx 23.6 \quad \frac{f_\phi^2}{4\pi} \approx 18.4$$

As any hadronic cross–section, $\sigma_{VDM}^{\gamma p}$ receives contributions from elastic and inelastic diffractive, and high- p_T non–diffractive reactions:

- VDM elastic processes $\gamma + p \rightarrow V + p$.
The Compton elastic scattering $\gamma + p \rightarrow \gamma + p$ is of order $O(\alpha^2)$ compared with the $O(\alpha)$ VDM processes and can be neglected.
- Diffractive dissociation processes
 - single dissociation of the proton $\gamma + p \rightarrow V + X$
 - single dissociation of the photon $\gamma + p \rightarrow X + p$
 - double dissociation $\gamma + p \rightarrow X_1 + X_2$

For single dissociation one of the incident particles dissociates after the interaction, while the other particle keeps its original identity (in case of the proton dissociation in photoproduction a vector meson is produced in the photon direction). For double dissociation both incident particles dissociate. Since diffractive reactions involve no exchange of quantum numbers between the incident particles, the final state is characterized by the appearance of large rapidity gaps with no hadrons (more details in section 3.5).

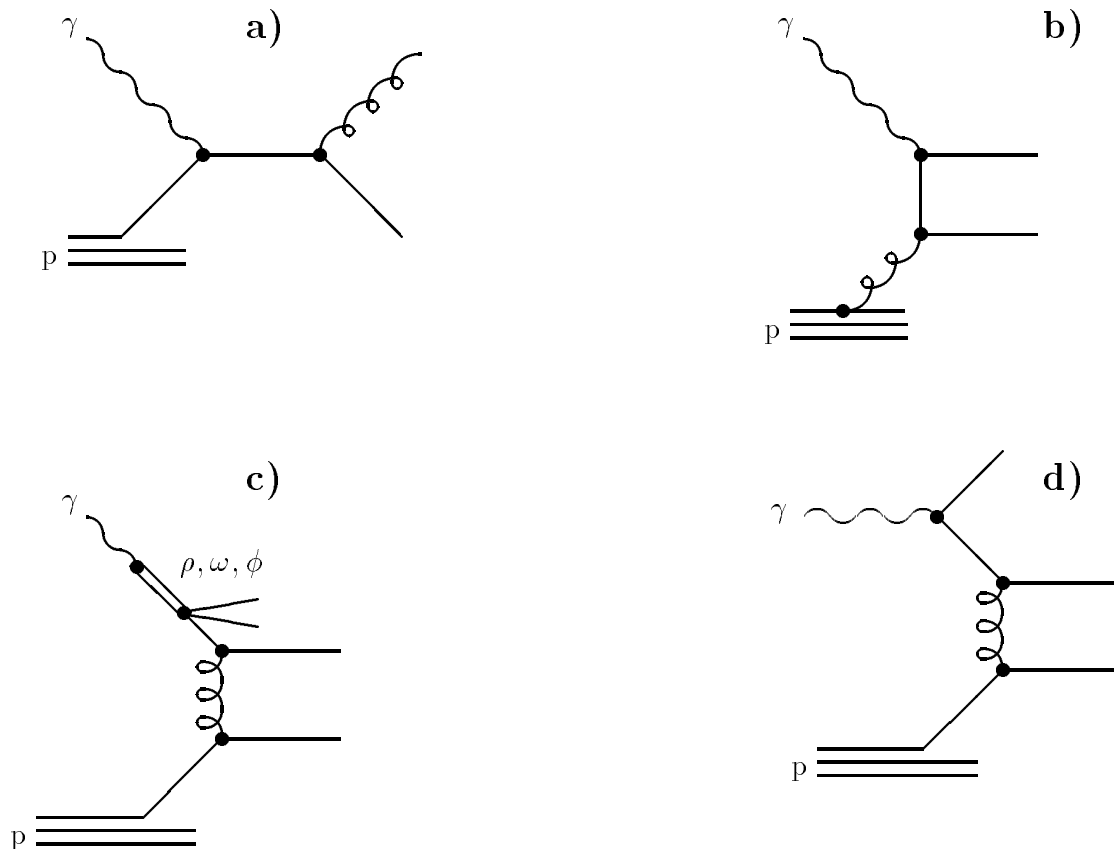


Figure 3.4: The diagrams for the hard photoproduction processes: (a,b)– direct photon processes, c)–VDM hard scattering, d)–anomalous process.

- The non-diffractive part of VDM covers all other possible processes, i.e. $\gamma + p \rightarrow X$, where the system X is supposed not to contain any large rapidity gaps, i.e. to be distinctive from diffractive events.

VDM is a purely phenomenological model, which, however, describes the fixed target photoproduction data fairly well. Significant differences only appear at the largest p_T , accessed at fixed target experiments. These deviations are due to “hard” interactions of the photon or its constituents with a proton.

Two types of processes contribute to large p_T photoproduction:

- The direct photon processes, where a bare photon interacts with a parton from the proton. The most important direct processes are the QCD–Compton process (Fig.3.4a), in which a photon couples to a quark in the proton and produces a quark and a gluon in the final state, and the boson-gluon fusion process (Fig.3.4b), which can produce light quark-antiquark pairs, fragmenting into two jets, as well as heavy quark $c\bar{c}$ or $b\bar{b}$ pairs.

- The resolved photon processes, where the photon acts as a source of partons which interact with the partons in the proton. Within resolved processes one can distinguish between [22]
 - the VDM hard scattering processes (Fig.3.4c) and
 - the anomalous or pointlike processes (Fig.3.4d), where the photon perturbatively branches into a quark–antiquark pair, which does not form a bound hadronic state, and one of these partons interacts with a parton from the proton.

The anomalous component is not present in hadronic collisions and is a special feature of the photon. The difference between the VDM and the anomalous parts is the difference in virtuality of $\gamma \leftrightarrow q\bar{q}$ fluctuations, as characterized by the common p_T^2 of the quark and antiquark with respect to the photon direction. When the virtuality is small the fluctuation is long-lived, then a soft gluon cloud can develop around the $q\bar{q}$ pair, and a vector meson wave function description may be a good approximation. But when the virtuality is larger, the fluctuation is too short-lived to develop into a hadronic state. In this case, the perturbative description is fully appropriate, while the VDM part must be based on a non-perturbative phenomenological ansatz.

In direct processes the full energy of the photon enters the hard subprocess, whereas in the resolved case a part of the photon energy is taken by the spectator partons, which do not contribute to a hard interaction. In case of resolved processes one can define the photon as having a structure, described by a structure function, similar to the structure function of a hadron (see section 3.2).

The underlying theoretical framework for the hard interactions is the QCD improved parton model. In leading order (LO) QCD the final state consists just of two partons with large transverse energies fragmenting into two jets of hadrons in addition to the proton remnant and the scattered electron which come out with small transverse energies. In the resolved process the spectator parton of the photon produces also a remnant jet with a small transverse energy. It is important to note that the full final state contains another component consisting of primarily low p_T particles. In general this “underlying event” itself has two components. One component involves the initial and final state radiations from partons that participate in the hard scattering and is correlated with the hard scattering. The other component involves the interactions of the “spectator” partons and is essentially uncorrelated with hard scattering.

Hard interactions are in general non-diffractive. Recently, hard scattering processes in diffractive events have been observed by experiments (see section 3.5).

The high energy interactions of real photons with matter have been studied in fixed target experiments with photon beams, and in $\gamma\gamma$ interactions at e^+e^- colliders. However, the different components of the γp interactions have not yet been unambiguously isolated by these experiments. It was expected that the large centre of mass energy at HERA would allow a clean separation of the resolved and direct components and, similar to high energy hadronic interactions, clear jet production and jet structure would become visible. With

the first data taken at HERA this general picture of hard photon-proton scattering has been confirmed by studying single particle distributions and jet topologies. It was shown that, similar to hadron-hadron scattering, photoproduction exhibits both the production of transverse jets and a substantial rate of events which contain particles with transverse momenta larger than a few GeV [23]-[29]. Models including leading order (LO) QCD diagrams for resolved and direct processes describe the gross features of these data. The inclusive charged particle cross-section shows that the resolved processes dominate at lower p_T , but constitute only about 70% of the cross-section at large p_T values (about 7–8 GeV), the remaining part are direct processes.

A central subject of photoproduction studies at HERA is the photon structure. At HERA energies the results of several authors [30] agree in predictions that the photoproduction of jets is dominated by resolved reactions at low and medium transverse energies E_t^{jet} of the jets (say below 30 GeV). Thus, in the framework of this QCD picture, photoproduction of jets can be used to obtain information on the photon's parton content assuming the parton densities in the proton are known. It also offers a new tool for the determination of the gluon density in the photon [26], about which very little is known at present. The information about the parton distribution in the photon can be obtained also from the production of heavy quarks, prompt photons and pions.

3.3.2 Inclusive jet cross-section

Hard processes which occur in high energy hadron-hadron interactions are characterized by large momentum transfer and by the production of large invariant masses. Such processes are perturbatively calculable and in general correctly described by the QCD improved quark-parton model.

In leading order QCD the hard interactions are viewed as $2 \rightarrow 2$ parton-parton scattering $q + q' \rightarrow q + q'$, $q + g \rightarrow q + g$ and $g + g \rightarrow g + g$ for resolved photons and $\gamma + q \rightarrow q + g$ and $\gamma + g \rightarrow q + \bar{q}$ for direct photons (Feynman diagrams for some of leading order parton-parton scattering processes are depicted in Fig.3.5). The differential cross-sections $d\hat{\sigma}/d\hat{t}$ for these processes are calculated by QCD as function of the Mandelstam variables \hat{s} , \hat{t} and \hat{u} :

$$\hat{s} = (p_1 + p_2)^2 = (p_3 + p_4)^2 \quad (3.19)$$

$$\hat{t} = (p_1 - p_3)^2 = (p_2 - p_4)^2 \quad (3.20)$$

$$\hat{u} = (p_1 - p_4)^2 = (p_2 - p_3)^2 \quad (3.21)$$

where p_1 , p_2 are the 4-momenta of incoming, and p_3 , p_4 of outgoing partons. The cross-sections for the main lowest order processes are shown in Table 3.1 [31]. Here q and g denote quark and gluon, respectively. Subscripts i, j denote distinct flavours. For direct processes the dominant subgraphs involve the exchange of a quark in the t - and u -channels, and so the parton-level cross-section $d\hat{\sigma}/d\hat{t}$ behaves like $\sim 1/p_T^2$ (at fixed \hat{s}),

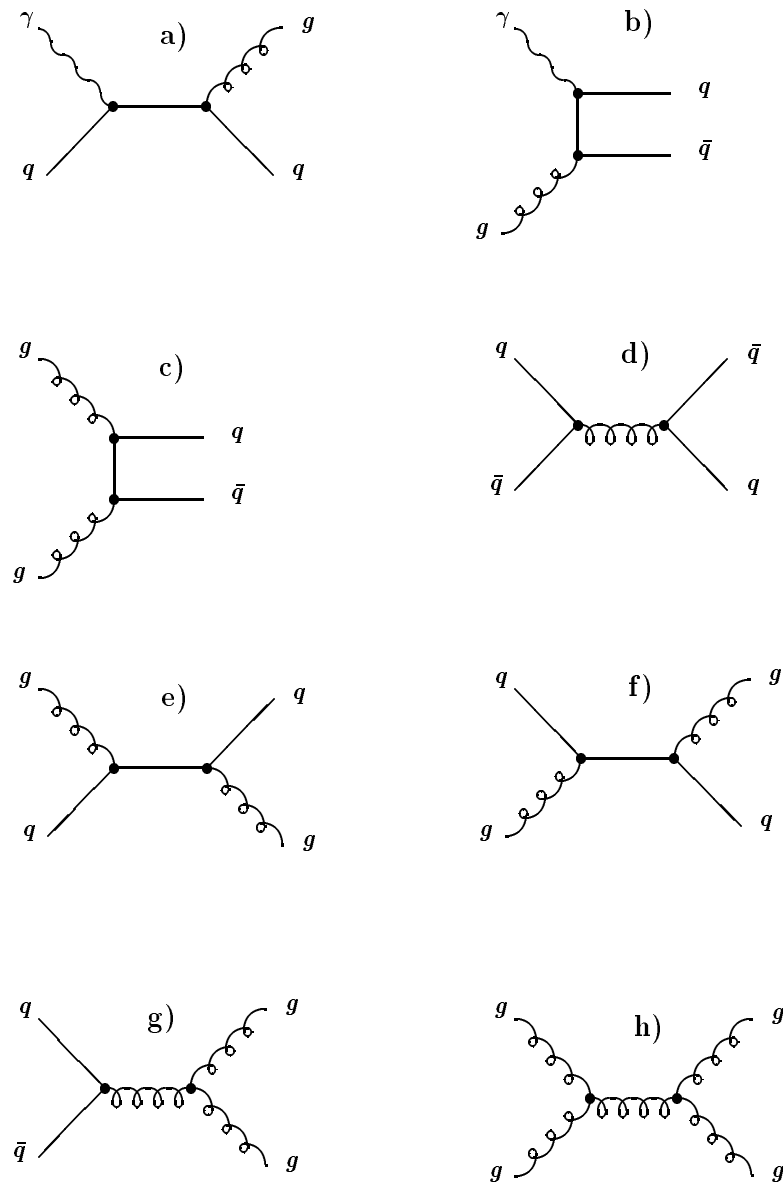


Figure 3.5: Feynman graphs for hard photoproduction subprocesses due to direct photon interactions (**a,b**), and due to resolved photon interactions (**c-h**).

- a)** QCD-Compton; **b)** photon-gluon fusion;
- c)** gluon-gluon fusion; **d)** quark-antiquark annihilation in $q\bar{q}$;
- e)** quark-gluon scattering (gluon from photon);
- f)** quark-gluon scattering (gluon from proton);
- g)** quark-antiquark annihilation in gg ; **h)** gluon-gluon scattering.

subprocess	$d\hat{\sigma}/d\hat{t}$
$q_i q_j \rightarrow q_i q_j, q_i \bar{q}_j \rightarrow q_i \bar{q}_j$	$\frac{4\pi\alpha_s^2}{9\hat{s}^2} \frac{\hat{s}^2 + \hat{u}^2}{\hat{t}^2}$
$q_i q_i \rightarrow q_i q_i$	$\frac{\pi\alpha_s^2}{\hat{s}^2} \left[\frac{4}{9} \left(\frac{\hat{s}^2 + \hat{u}^2}{\hat{t}^2} + \frac{\hat{s}^2 + \hat{t}^2}{\hat{u}^2} \right) - \frac{8}{27} \frac{\hat{s}^2}{\hat{u}\hat{t}} \right]$
$q_i \bar{q}_i \rightarrow q_j \bar{q}_j$	$\frac{4\pi\alpha_s^2}{9\hat{s}^2} \frac{\hat{t}^2 + \hat{u}^2}{\hat{s}^2}$
$q_i \bar{q}_i \rightarrow q_i \bar{q}_i$	$\frac{\pi\alpha_s^2}{\hat{s}^2} \left[\frac{4}{9} \left(\frac{\hat{s}^2 + \hat{u}^2}{\hat{t}^2} + \frac{\hat{t}^2 + \hat{u}^2}{\hat{s}^2} \right) - \frac{8}{27} \frac{\hat{u}^2}{\hat{s}\hat{t}} \right]$
$q\bar{q} \rightarrow gg$	$\frac{\pi\alpha_s^2}{\hat{s}^2} \left[\frac{32}{27} \frac{\hat{u}^2 + \hat{t}^2}{\hat{u}\hat{t}} - \frac{8}{3} \frac{\hat{u}^2 + \hat{t}^2}{\hat{s}^2} \right]$
$gg \rightarrow q\bar{q}$	$\frac{\pi\alpha_s^2}{\hat{s}^2} \left[\frac{1}{6} \frac{\hat{u}^2 + \hat{t}^2}{\hat{u}\hat{t}} - \frac{3}{8} \frac{\hat{u}^2 + \hat{s}^2}{\hat{t}^2} \right]$
$qg \rightarrow qg$	$\frac{\pi\alpha_s^2}{\hat{s}^2} \left[-\frac{4}{9} \frac{\hat{u}^2 + \hat{s}^2}{\hat{u}\hat{s}} + \frac{\hat{u}^2 + \hat{s}^2}{\hat{t}^2} \right]$
$gg \rightarrow gg$	$\frac{\pi\alpha_s^2}{\hat{s}^2} \left[\frac{9}{2} \left(3 - \frac{\hat{u}\hat{t}}{\hat{s}^2} - \frac{\hat{u}\hat{s}}{\hat{t}^2} - \frac{\hat{s}\hat{t}}{\hat{u}^2} \right) \right]$
$\gamma g \rightarrow q_i \bar{q}_i$	$\frac{\pi\alpha\alpha_s e_i^2}{\hat{s}^2} \left(\frac{\hat{u}}{\hat{t}} + \frac{\hat{t}}{\hat{u}} \right)$
$\gamma q_i \rightarrow q_i g$	$-\frac{8\pi\alpha\alpha_s e_i^2}{3\hat{s}^2} \left(\frac{\hat{t}}{\hat{s}} + \frac{\hat{s}}{\hat{t}} \right)$

Table 3.1: Hard scattering subprocesses in QCD and their differential cross-sections in the lowest order of perturbation theory.

subprocess	$\sigma_{subprocess}^{ep} [nb]$ ($\hat{p}_T^{min} = 2 GeV$)	$\sigma_{subprocess}^{ep} [nb]$ ($\hat{p}_T^{min} = 5 GeV$)
$qq \rightarrow qq$	75.7	4.54
$q\bar{q} \rightarrow q\bar{q}$	0.87	0.09
$q\bar{q} \rightarrow gg$	1.1	0.09
$gg \rightarrow qq$	638.0	22.7
$gg \rightarrow q\bar{q}$	19.7	0.47
$gg \rightarrow gg$	711.0	13.2
$\gamma q \rightarrow qq$	11.9	1.31
$\gamma g \rightarrow q\bar{q}$	88.6	6.10

Table 3.2: The contributions to the ep cross-sections given by PYTHIA Monte-Carlo generator (with GRV-LO parametrizations for the photon and proton distribution functions) for the transverse momentum cut-off $\hat{p}_T^{min} = 2 GeV$ and $5 GeV$.

whereas for resolved processes the major contribution to cross-section is through a gluon exchange in the t - and u -channels, and $d\hat{\sigma}/d\hat{t} \sim 1/p_T^4$.

Since partons themselves can not be observed in experiment, the partonic cross-section can be tested via production of hadronic jets in hadron-hadron collisions. In leading order QCD predictions for the jet cross-section are usually obtained by convolution of the parton densities in the photon and in the proton with all possible hard partonic scattering cross-sections. To calculate the jet rate it is necessary to define a low cut-off \hat{p}_T^{min} which defines how far down in \hat{p}_T perturbative parton-parton scattering is assumed to occur. Based on studies of $p\bar{p}$ collisions, a value of \hat{p}_T^{min} in the range $1.5 - 2.0 GeV$ is obtained [32].

The differential cross-section of inclusive jet production, as a function of jet momentum p and energy E , is given by

$$E \frac{d^3\sigma}{d^3p}(\gamma + p \rightarrow jet + X) = \frac{1}{\pi} \sum_{i,j} \int dx_1 \int dx_2 f_{i/\gamma}(x_1, \mu^2) f_{j/p}(x_2, \mu^2) \frac{d\hat{\sigma}_{ij}^k}{d\hat{t}} \delta\left(1 + \frac{\hat{t} + \hat{u}}{\hat{s}}\right) \quad (3.22)$$

where subscripts i and j label possible incoming partons taken from two incoming particles, and k denotes the different allowed final-state flavour content, $\hat{s} = x_\gamma x_p s_{\gamma p}$ is the centre of mass energy of the parton-parton system, x_γ (x_p) is the fraction of the photon (proton) momentum carried by the interacting parton, $f_{i/\gamma}$ ($f_{i/p}$) is the distribution

function of partons i in the photon (proton). As scale μ in the structure functions conventionally the transverse momentum \hat{p}_T produced in the parton-parton scattering is used².

Assuming massless particles this cross-section can be written as a function of the jet transverse momentum p_T and pseudorapidity $\eta = -\ln \tan \frac{\theta}{2}$, where θ is the polar angle with respect to the proton direction

$$E \frac{d^3\sigma}{d^3p}(\gamma + p \rightarrow jet + X) = \frac{1}{\pi} \frac{d^3\sigma}{d\eta d^2p_T}(\gamma + p \rightarrow jet + X) \quad (3.23)$$

Since Eq.(3.23) represents a purely perturbative results, it contains no explicit nonperturbative effects, either from fragmentation smearing or from the underlying event. These effects are modeled in the Monte-Carlo generators (section 3.6).

The transverse momentum of each massless parton in the final state is given by $p_T^2 = \frac{1}{4}\hat{s}(1 - \cos^2\theta^*)$, where θ^* is the parton scattering angle in the CMS of the two partons. For low p_T , the low x region of the parton densities is probed, in which case the gluon density in the proton and in the photon dominates. In order to illustrate the relative importance of the subprocesses, their absolute contributions to the ep cross-sections given by the PYTHIA Monte-Carlo generator (with GRV-LO parametrizations for the photon and proton parton distribution functions) for a transverse momentum cut-off $\hat{p}_T = 2 \text{ GeV}$ and 5 GeV are given in Table 3.2. At low p_T the main contribution to the cross-section is given by the gluon initiated processes. With increasing p_T , higher values of x are probed and the quark initiated processes become more significant. At large p_T values the direct photon processes are expected to dominate over the resolved.

Differential inclusive jet cross-sections have been measured in photoproduction events at HERA before [24, 29]. The transverse energy cross-section $d\sigma/dE_T^{jet}$ is steeply falling and can be described well by a power law $(E_T^{jet})^{-n}$, where $n \approx 6.1 \pm 0.5$ (see chapter 5). The measured cross-section is described by the QCD calculations and can therefore be interpreted as the result of underlying parton scattering processes. The observed jets are mainly located in the photon hemisphere and cover several units in pseudorapidity. Jet pseudorapidity cross-sections $d\sigma/d\eta^{jet}$ are therefore sensitive to the parton distributions in the photon. Comparison of the measured cross-sections with QCD calculations can be used for extraction of these parton distributions.

3.4 The photon structure function

The photon structure can be understood by probing it in a similar way as that of the nucleon. Before HERA, the structure of the photon was experimentally investigated mainly in inclusive $e\gamma$ deep inelastic scattering at e^+e^- colliders. Here one of the incoming leptons is scattered at a small angle and the emitted photon is almost real. The structure of this photon is probed by the highly virtual photon with the virtuality μ^2 , which is emitted by the second lepton which scatters at large angle. Four e^+e^- experiments have

²Normally the scale is denoted Q^2 , but in this thesis Q^2 is used to denote the virtuality of the photon.

presented results of their measurements at PETRA: PLUTO, for average μ^2 values of 2.4, 4.3, 5.3, 9.2, and 45 GeV^2 [33]; TASSO, at $\langle \mu^2 \rangle = 23$ GeV^2 [34]; JADE, for $\langle \mu^2 \rangle = 24$ and 100 GeV^2 [35]; and CELLO for $\langle \mu^2 \rangle = 7, 13.1, \text{ and } 28.8$ GeV^2 [36]. At PEP, the TCP/ 2γ group measured F_2^γ at $\langle \mu^2 \rangle = 0.24, 0.38, 0.71, 1.31, 2.83, 5.09,$ and 20 GeV^2 [37]. At LEP, OPAL experiment presented measurement of F_2^γ at $\langle \mu^2 \rangle = 5.8$ and 14.7 GeV^2 [38], and DELPHI experiment at $\langle \mu^2 \rangle = 12$ GeV^2 [39].

Leading and next-to-leading order fits to these data allowed to extract the quark densities in the photon. As a result of $e\gamma$ deep inelastic scattering experiments, studied at e^+e^- colliders, the quark content of the photon is already relatively well known in the fractional momentum range of the parton $0.007 \leq x_\gamma \leq 1$ [40, 41].

An essential difference between the photon and hadron is that the photon can couple directly to quark-antiquark pairs. This additional (often called anomalous) contribution modifies the DGLAP equations by adding an inhomogeneous part (see for example ref.[41]). This anomalous part of the photon structure function can be calculated directly from the quark-parton model. This is attained by performing a full calculation of the cross-section $\gamma^* + \gamma \rightarrow q + \bar{q}$ which is electromagnetic with known couplings. In the framework of the quark-parton model the interaction goes through a box-diagram (Fig.3.6). The calculations give for F_2^γ [42, 41]:

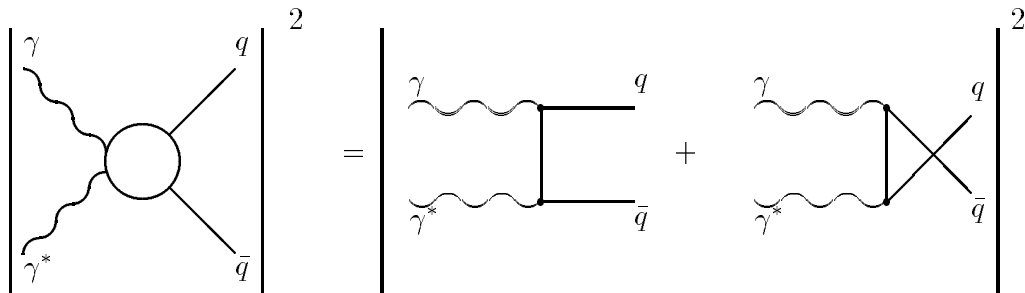


Figure 3.6: Diagrammatic presentation of the cross-section for the process $\gamma\gamma \rightarrow q\bar{q}$ in the QPM.

$$F_2^\gamma(x, \mu^2) = \frac{N_c \alpha}{\pi} \sum_{i=1}^f x e_{q_i}^4 \left[(x^2 + (1-x)^2) \ln \frac{\mu^2(1-x)}{m_{q_i}^2 x} + 8x(1-x) - 1 \right], \quad (3.24)$$

where N_c is the number of quark colors. By analogy to the nucleon case F_2^γ can be written in the form

$$F_2^\gamma(x, \mu^2) = \sum_{i=1}^f x e_{q_i}^2 q_i^\gamma(x, \mu^2) \quad (3.25)$$

where

$$q_i^\gamma(x, \mu^2) = \frac{N_c \alpha}{2\pi} e_{q_i}^2 \left[(x^2 + (1-x)^2) \ln \frac{\mu^2(1-x)}{m_{q_i}^2 x} + 8x(1-x) - 1 \right] \quad (3.26)$$

In the QCD improved parton model gluons can be emitted and absorbed by the strongly interacting quarks. This leads to Bjorken scaling violation, i.e. quark densities q_i acquiring a logarithmic μ^2 dependence, which is described by the DGLAP evolution equations [11]. The analysis of the scaling violation allow to obtain the gluon distribution function in the proton (see Eq.(3.14) and section 3.2). In contrast to the proton, the photon structure function shows strong scaling violation even without the presence of gluons (as is seen from Eq.(3.24)). $F_2^\gamma(x, \mu^2)$ has a logarithmic positive scaling violation ($\sim \ln \mu^2$) for all x values. The introduction of gluon bremsstrahlung does not change significantly the character of the μ^2 dependence of F_2^γ obtained in the quark-parton model.

The information available from e^+e^- experiments give only weak constraints on the gluon of the photon. Only recent TRISTAN measurements (TOPAZ and AMY collaborations) of F_2^γ [43] for squared transverse momenta of the outgoing partons $\mu^2 \sim 5 - 390 \text{ GeV}^2$ show that the gluon contribution to the photon structure function is essential to describe these measurements successfully.

Another important difference between the nucleon and photon case is that, while the proton structure function drops at high x , the photon structure function is large in the high x region at moderate and large μ^2 .

The most frequently used parametrizations make no distinction between the VDM and anomalous contributions to the structure function. A parametrization, fixed at a given μ_0^2 given by experiments, is evolved to a different μ^2 region through the inhomogeneous DGLAP equations.

The first parametrization which uses this approach to evolve an input parametrization of parton distributions at $\mu_0^2 = 1 \text{ GeV}^2$, so that data at higher μ^2 (PLUTO data at 5.9 GeV^2) are reproduced, is the parametrization of Drees and Grassie (DG) [44]. They start with 3 flavours at the input and evolve to higher μ^2 using 4 and 5 flavours. For Λ_{QCD} a value of 0.4 GeV is assumed. The input quark distributions are assumed to have a form:

$$xq(x) = A e_q^2 x \frac{x^2 + (1-x)^2}{1 - B \ln(1-x)} + C x^D (1-x)^E \quad (3.27)$$

where the first term reflects point-like and the second term hadron-like contributions. The gluon distribution is assumed to be:

$$xg(x) = C_g x^{D_g} (1-x)^{E_g} \quad (3.28)$$

The data available at the time when the parametrization was first used didn't allow to fit the gluon distribution.

Newer parametrizations which are based on a similar approach are the Abramowicz, Charchula and Levy parametrizations (LAC 1-3) [45]. The input scales are $\mu_0^2 = 4 \text{ GeV}^2$ for sets 1,2 and $\mu_0^2 = 1 \text{ GeV}^2$ for set 3. The evolution is carried out for four flavours with a Λ_{QCD} of 0.2 GeV . The parametrizations LAC 1-3 differ mainly in the assumptions used for the gluon distributions. The LAC-1 and LAC-2 parametrizations are practically

equal for $x \gtrsim 0.02$ (see Fig.3.7). LAC-3 has a smaller gluon contribution at small x but a significantly larger one at high x values.

In contrast to DG and LAC parametrizations which allow an arbitrary form of input distributions at scale μ_0^2 and therefore have a fairly large number of free parameters, Glück-Reya-Vogt (GRV) use theoretical considerations to fix the shape of the input distributions reducing the number of free parameters [47]. This parametrization exists for next-to-leading order (NLO) as well. The authors assume that the pure VDM ansatz is valid at the rather low input scale $\mu_0^2 = 0.25 \text{ GeV}^2$ ($\mu_0^2 = 0.3 \text{ GeV}^2$ for NLO).

$$q_i^\gamma(x, \mu_0^2) = k \frac{4\pi\alpha}{f_\rho^2} q_i^{\pi^0}(x, \mu_0^2), \quad (3.29)$$

where $i = \text{quark, gluon}$; $f_\rho^2/4\pi = 2.2$, and $k \approx 2$ for LO and ≈ 1.6 for NLO– obtained from a fit to existing F_2^γ data.

To illustrate the differences between the different parton distribution functions in the photon the distribution functions $xg(x, \mu^2)$ and $F_2(x, \mu^2)$ are shown in Fig.3.7 as function of x at a scale $\mu^2 = 50 \text{ GeV}^2$.

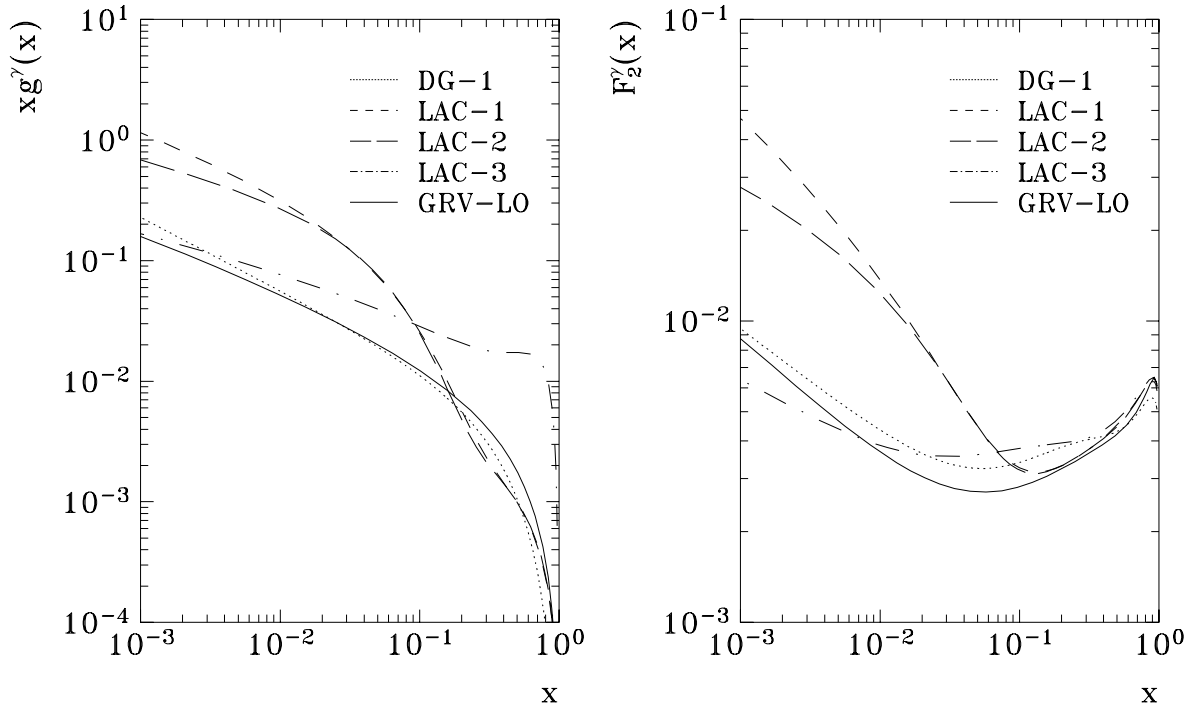


Figure 3.7: The different parametrizations of the photon distribution function, obtained at a scale $\mu^2 = 50 \text{ GeV}^2$.

3.5 Hard interactions in photon diffractive dissociation processes

A diagram for a single γ diffractive dissociation process $\gamma + p \rightarrow X + p$ is shown in Fig.3.8. Here the proton is elastically scattered retaining a large fraction of the initial momentum;

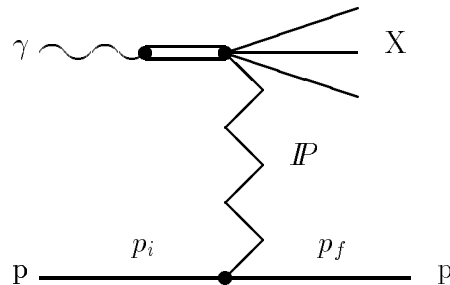


Figure 3.8: Photon diffractive dissociation.

it can be expressed via Feynman- x variable

$$x_F = \frac{p_l}{p_{l \max}} \approx \frac{p_f}{p_i} \quad (3.30)$$

Here p_l is a longitudinal momentum of a particle in the CMS with respect to the direction of the initial proton, and the $p_{l \max}$ is a maximal possible longitudinal momentum ($p_{l \max} = \sqrt{s}/2$). p_i and p_f are the longitudinal momenta of initial and final state protons. For diffractive processes which are characterized by small (up to few GeV^2) and negative values of 4-momentum transfer $t = (p_i - p_f)^2$, x_F can be related to the mass M_X into which the photon dissociates:

$$x_F \approx 1 - \frac{M_X^2}{s} > 0.9 \quad (3.31)$$

where s is the centre of mass energy of the γp system.

The basic features of hadronic diffractive processes are well described by the Regge theory [48] using the exchange in the t -channel of “Reggeon”, virtual ($M^2 < 0$) hadronic states whose angular momentum J changes linearly with t . The graph J vs t (or M^2) is called Regge trajectory, and when this is extrapolated to the positive M^2 region passes through J, M^2 values of known mesons.

Regge diagrams for processes where one of interacting particles is elastically scattered are shown in Fig.3.9 .

In this framework the differential cross-section, $d\sigma/dtdM_X^2$ is given in terms of Regge trajectories, which carry the energy-momentum transferred between the upper and lower vertices, triple Regge couplings $g_{kl}(t)$ and residue functions $\beta(t)$.

$$\frac{d^2\sigma^{AB}}{dt dM_X^2} = \frac{1}{s} \sum_{k,l} \frac{\beta_{Bk}(0)\beta_{Al}^2(t)g_{kl}(t)}{16\pi s} \left(\frac{s}{M_X^2}\right)^{2\alpha_l(t)} (M_X^2)^{\alpha_k(0)} \quad (3.32)$$

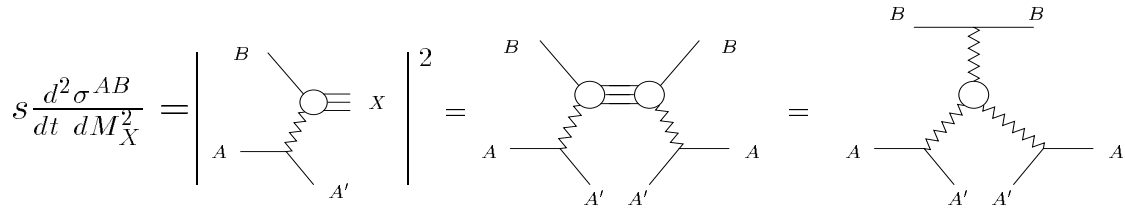


Figure 3.9: Regge diagrams for the single diffractive dissociation.

The most common Regge-trajectories are :

Pomeron, with $\alpha_{\mathbb{P}}(t) = \alpha_{\mathbb{P}}(0) + \alpha'_{\mathbb{P}}(t)$

Reggeon, with $\alpha_R(t) \cong 0.5 + t$

Pion, with $\alpha_{\pi}(t) \cong 0. + 0.9t$

In contrast to the standard Regge trajectories, no particles have been found on the time-like sector of the Pomeron trajectory. The Reggeon exchange will lead to a fast decrease of the cross-section with s , in contrast to a slow rise in the case of the Pomeron exchange. The differential cross-sections have been measured and consistent behavior found for various combinations of incident particles and at different energies. The experimental results support the hypothesis that diffractive processes are dominated by a Pomeron trajectory [49], i.e. an object with vacuum quantum numbers, with $\alpha_{\mathbb{P}}(0) \cong 1$, $\alpha'_{\mathbb{P}}(0) < 0.3 \text{ GeV}^{-2}$ and $g_{\mathbb{P}\mathbb{P}\mathbb{P}}(0) \neq 0$. Also the factorization hypothesis which is observed experimentally to hold a good approximation, supports this exchange mechanism and allows to consider a ‘‘Pomeron-proton’’ interaction. One should note, that the exact nature and the question whether this object has any particle like properties is far from being resolved.

Inserting $\alpha_{\mathbb{P}}(t) = 1 + \alpha'_{\mathbb{P}}(t)$ into Eq.(3.32), a simplified expression for differential cross-section for diffractive processes can be obtained:

$$\frac{d^2\sigma^{AB}(s, M_X^2, t)}{dt dM_X^2} = \frac{\beta_{B\mathbb{P}}(0)\beta_{A\mathbb{P}}^2(t)g_{\mathbb{P}\mathbb{P}\mathbb{P}}(t)}{16\pi} \frac{1}{M_x^2} e^{bt} \quad (3.33)$$

where slope parameter

$$b = b_0 + 2\alpha'(t)\ln\left(\frac{s}{M_X^2}\right) \approx 4.6 \text{ GeV}^{-2} + 0.25 \text{ GeV}^{-2}\ln(0.25 \text{ GeV}^{-2}s). \quad (3.34)$$

The couplings $\beta_{A\mathbb{P}}$, $\beta_{B\mathbb{P}}$ are related to the Pomeron term of the total cross-section parametrization $\beta_{A\mathbb{P}}\beta_{B\mathbb{P}} = X^{AB}s^\epsilon$ [22].³ The triple-Pomeron coupling is determined

³In the hadron-hadron interactions, the total hadronic cross-section for $AB \rightarrow \text{anything}$, σ_{tot}^{AB} , is calculated using the parametrization of Donnachie and Landshoff [50]. In this approach, the cross-section is given as the sum of one Pomeron term and one Reggeon term $\sigma_{tot}^{AB} = X^{AB}s^\epsilon + Y^{AB}s^{-\eta}$, where $\epsilon = 0.0808$ and $\eta = 0.4525$ are expected to be universal, whereas the coefficients X^{AB} and Y^{AB} are specific to each initial state.

from single diffractive data to be $g_{\mathbb{P}\mathbb{P}\mathbb{P}} \approx 0.359 \text{ mb}^{1/2}$ [22]. Thus, for Pomeron dominance and for the simple diagrams of Fig.3.9 the diffractive dissociation cross-section $d^2\sigma/dtdM_X^2$ depends exponentially on t , logarithmically on s and varies as $1/M_X^2$.

Regge theory which describes the measured differential cross-section cannot give reasonable description of the multiparticle final state in diffractive dissociation. Traditionally the final state is assumed to be described by a multiperipheral type of model in which particles are distributed throughout the final state phase space with limited transverse momentum [51]. This approach has been used successfully so far for comparisons with the available measurements of multiplicity and rapidity distributions of charged particles from the diffractive system [49].

On the other hand, in modern QCD language, it is tempting to consider the Pomeron as a partonic system [52] which can be probed in a hard scattering process. Models based on this idea assume that the Pomeron essentially behaves as a hadron and the concept of a Pomeron structure function is introduced [53, 54, 55, 56]. The first model of this kind was proposed by Ingelman and Schlein. In this scheme, first, a Pomeron is emitted with a small momentum transfer from the proton, and then one of its constituent partons interacts with a constituent parton of the other initial hadron with large momentum transfer.

The factorization theorem allows to write the cross-section for this process as

$$\frac{d\sigma(h + p \rightarrow p + X)}{dx_{\mathbb{P}/p} dt dx_1 dx_2} = f_{\mathbb{P}/p}(x_{\mathbb{P}/p}, t) \frac{d\sigma(h + \mathbb{P} \rightarrow X)}{dx_1 dx_2} \quad (3.35)$$

where h denotes the dissociating hadron (photon in our case) [57]. Here, $f_{\mathbb{P}/p}$ is called ‘‘Pomeron flux’’ and describes the emission of a Pomeron from the proton with a fraction $x_{\mathbb{P}/p} < 0.1$ of the proton momentum with a small momentum transfer t . The Pomeron flux is derived by Regge phenomenology and can be approximated by [57]

$$f_{\mathbb{P}/p}(x_{\mathbb{P}/p}, t) = \frac{d\sigma/dx_{\mathbb{P}/p}dt}{\sigma_{\mathbb{P}p \rightarrow X}} = \frac{6.38e^{8t} + 0.424e^{3t}}{2.3x_{\mathbb{P}/p}} \quad (3.36)$$

Another functional form of the flux factor is given by Donnachie and Landshoff [54], but is numerically about the same in the region of small t .⁴

⁴

$$f_{\mathbb{P}/p}^{DL}(x_{\mathbb{P}/p}, t) = \frac{9\beta_0^2}{4\pi^2} \left(\frac{1}{x_{\mathbb{P}/p}}\right)^{2\alpha(t)-1} [F_1(t)]^2 \quad (3.37)$$

Here the factor $\beta_0 F_1(t)$ describes the Pomeron-quark coupling:

$$\beta_0 = 3.24 \text{ GeV}^{-2}$$

$$F_1(t) = \frac{4m_p^2 - 2.8t}{4m_p^2 - t} \left(\frac{1}{1 - t/0.7}\right)^{2\alpha(t)} \quad (3.38)$$

$F_1(t)$ is an elastic form-factor of the proton, and m_p is the proton mass. $\alpha(t)$ is the Pomeron trajectory

$$\alpha(t) = 1 + \epsilon + \alpha' t; \quad \epsilon = 0.085; \quad \alpha' = 0.25 \quad (3.39)$$

The second factor in Eq.(3.35) $d\sigma(h + \mathbb{P} \rightarrow X)/dx_1 dx_2$ is a hard Pomeron–particle interaction cross–section and is given in terms of the Pomeron and the particle h densities of partons and the appropriate hard scattering subprocess cross–section by:

$$\frac{d\sigma(h + \mathbb{P} \rightarrow X)}{dx_1 dx_2 d\hat{t}} = f_{p_1/\mathbb{P}}(x_1, Q^2) f_{p_2/h}(x_2, Q^2) \frac{d\hat{\sigma}}{d\hat{t}}(p_1 p_2 \rightarrow p'_1 p'_2) \quad (3.40)$$

The Pomeron structure function is so far an unknown quantity. There are different assumption in the literature [53, 54, 58, 59]. The parton distribution functions strongly differ in the partons considered, in their shapes, in their normalizations, and in the Q^2 evolution of the parton densities. Many authors assume that the Pomeron structure function is purely gluonic [53, 57]. They make various alternative guesses for the shape of the structure function. Two extreme possibilities are:

–hard gluon structure function

$$xg(x) = 6x(1 - x) \quad (3.41)$$

–soft gluon structure function

$$xg(x) = (1 + a)(1 - x)^a, \quad (3.42)$$

where $a = 5$ in Eq.(3.42), if the gluons in the Pomeron are as soft as the gluon sea in a nucleon.

The first distribution assumes that two-gluons share the Pomeron momentum, when the second distribution assumes that the Pomeron is a many-gluon system. These distribution have both been normalized to saturate the momentum sum rule

$$\int_0^1 xg(x) dx = 1 \quad (3.43)$$

Other authors assume, that the Pomeron in analogy with the photon, couples to quarks and antiquarks and has a purely quark structure function. If only $u\bar{u}$ and $d\bar{d}$ pairs contribute, then the momentum sum rule is fulfilled by

$$xf(x) = \frac{6}{4}x(1 - x) \quad (3.44)$$

However, Donnachie and Landshoff argue [54] that since the Pomeron exchanged is not a physical particle, the momentum sum rules do not need to be fulfilled. They suggest a Pomeron structure function:

$$xf(x) = \frac{1}{3}C\pi x(1 - x), \quad \text{with } C = 0.23 \quad (3.45)$$

The absolute normalization for function Eq.(3.45) after summation over the quark flavours differs from the Eq.(3.41,3.42,3.44) by the factor 7.5.

In addition one can consider interactions where almost all the Pomeron momentum enters the hard scattering [55, 60, 61]. These effects would lead to a δ –function like term

in the Pomeron structure function. The first observation of this, so called “superhard Pomeron”, was made by UA8 experiment at the CERN Sp \bar{p} S collider [62].

In contrast to the phenomenological limited p_T phase space approach, the hard diffraction models predict that, similar to high energy hadron-hadron scattering, high mass diffractive dissociation exhibits the production of jets and a large p_T tail in the differential transverse momentum distribution. It was suggested that hard hadron–Pomeron scattering could be observed in diffractive hadronic collisions at high energies.

The UA8 collaboration at CERN recently has shown evidence for jet production in diffractive $p\bar{p}$ events [62], interpreted as resulting from the collisions with partons from the Pomeron. Furthermore, within this partonic picture, these data have shown sensitivity to the parton distribution in the Pomeron. The hard diffraction phenomena are expected also in photoproduction processes. Both direct and resolved photon interactions can contribute to these interactions. In particular, the p_T spectra of particles and the jet production are expected to provide important information on the underlying dynamics of the diffractive process.

3.6 Monte–Carlo models

In order to correct the data for detector effects and to compare with the theoretical predictions, γp interactions in the H1 detector have been simulated using the Monte-Carlo method. First, the γp interactions have been generated by different Monte-Carlo generators, which are briefly described in this section. Further, the result of the event generation were fed into the H1 detector simulation program containing a detailed description of the H1 detector geometry which is based on the GEANT package [63]. Then, Monte-Carlo events were processed through the same reconstruction and analysis chain as the data, and therefore could be later used for a direct comparison with the data.

3.6.1 PYTHIA

For the present analysis, the PYTHIA (versions 5.6 and 5.7) event generator [64] was used in the photon-proton interaction option summing the contributions from direct and resolved photon interactions, which were simulated separately. The simulation of quasi-real photon radiation from the electron was done with the IJRAY generator [65] according to the equivalent photon approximation (Eq.(3.17)). This program simulates the QED vertex $e \rightarrow e\gamma$ within a given kinematical region. For present analysis the kinematical cuts were set the same as given by the detector acceptance, i.e. $Q^2 < 0.01 \text{ GeV}^2$ and $0.25 < y < 0.7$ (see chapter 4).

For analysis of the hard non-diffractive scattering processes in photon-proton interactions, PYTHIA was used in its high p_T option for photoproduction. Here γp interactions are simulated as the hard scattering of the partons in the photon and in the proton, according to the leading order QCD matrix element calculations (Eq.(3.22) and Table 3.1).

In addition to hard scattering, the effects of initial and final state QCD radiation are included. These effects are higher order correction to LO parton-parton scattering and are described by leading logarithm type parton showers with two body parton splittings ($q \rightarrow q + g$, $g \rightarrow g + g$, $g \rightarrow q + \bar{q}$). In case of final state emission an outgoing virtual parton with large time-like mass generates a shower of partons with lower virtuality. The amount of emission is controlled by the momentum transfer scale \hat{p}_T of the hard subprocess. In the initial state radiation a parton constituent of an incident hadron with low space-like virtuality radiates partons. In the process it decreases its energy and increases its space-like virtual mass. This mass is bounded in absolute value by the scale \hat{p}_T of the hard subprocess. Initial state radiation occurs uncorrelated at the photon and at the proton side, and therefore can destroy momentum balance of hard jets and eventually lead to a 3-rd jet. Final state radiation does not lead to a momentum imbalance, but rather to a broadening of the jets.

An additional transverse momentum can be given to the hard interaction by the intrinsic k_t of the hard interacting parton, where k_t is defined with respect to the hadron direction. k_t distribution for the quark and antiquark from the photon ($\gamma \rightarrow q\bar{q}$) was parametrized in the simulation as $1/(k_t^2 + a^2)$, where $k_t < 5 \text{ GeV}$ and $a = 0.6 \text{ GeV}$ is a cut parameter.

The strong coupling constant $\alpha_s(\mu^2)$ was calculated in leading order QCD using $\Lambda_{QCD} = 200 \text{ MeV}$ with 4 flavours. The renormalization and factorization scales (μ) were both set to the transverse momentum \hat{p}_T produced in the parton-parton scattering.

Since a perturbative QCD calculation is not applicable for $\hat{p}_T \rightarrow 0$, where \hat{p}_T is the transverse momentum of the out-going partons in the hard scattering process, a minimum \hat{p}_T cut-off value \hat{p}_T^{min} is applied. For this analysis the cut-off $\hat{p}_T^{min} = 2.0 \text{ GeV}$ has been used.

The direct and resolved photon components were generated separately. For the parton distributions the leading order GRV-LO [46] parametrization for proton, and the GRV-LO [47] and LAC-1 [45] parametrizations for the photon structure were used, which give a satisfactory description of data [23]-[26].

For the hadronisation process the ‘‘Lund string’’ fragmentation scheme was applied (as implemented in JETSET [66] program). In this model the colored partons are connected via a ‘‘string’’ of self interacting gluons. The energy density within a string is $\sim 1 \text{ GeV}/fm$. The gluons can produce the quark-antiquark pairs. As the quark and antiquark move apart, the potential energy stored in the string increases, and then the string breaks down by the production of a new quark-antiquark pair. If the invariant mass of either of these string pieces is large enough, further breaks may occur. The string break-up process is assumed to proceed until only on-mass-shell hadrons remain, each hadron corresponding to a small piece of string with a quark at one end and an antiquark at the other.

Optionally, PYTHIA includes a model, which describes the possibility that several parton pairs undergo hard interactions in a hadron-hadron collisions, and thereby contribute to the overall event activity, in particularly at low p_T . This can happen because the parton densities probed at HERA are sufficiently large that even from a naive probabilistic point of view, the chance of more than one hard scatter in a γp interaction becomes

significant. The perturbative parton-parton scattering framework here is extended in the non-perturbative low- p_T region. A regularization of the divergence in the cross-section for $p_T \rightarrow 0$ is introduced, which provides the free parameters of the model. Models of this nature are usually called “eikonal” models [67] and are used to regularize the strong growth exhibited in minijet calculations of the γp cross-section.

This so called *multiple interaction* model has been explored in proton-antiproton collisions before [68]. It is assumed that the multiple interactions take place essentially independent of each other. They are ranging from soft to hard interactions but are by definition softer than the “main” hard process, i.e. $\hat{p}_{T MI} < \hat{p}_T$. The additional parton-parton interactions are calculated as perturbative gluon-gluon scattering processes. The necessity of adding these additional interactions came first from the analysis of the charged multiplicity distribution [69] and the distribution of the average transverse momentum of charged particles as function of the total multiplicity in event [70] at the Sp \bar{p} S collider. Also the “pedestal effect” [71], which implies that events with jet activity also have larger activity away from the jet core may be understood in a multiple interaction scenario [72]. From the analysis of the energy flow in the high E_T photoproduction [73] the minimum \hat{p}_T of the multiple interactions was set to 1.2 GeV .

PYTHIA 5.6 was used in this analysis also for generation of the soft diffractive component of the γp cross-section. The diffractive system is treated as a string with the quantum numbers of the original hadron. Since the exact nature of the Pomeron exchanged between the hadrons is unknown, two alternatives, mixed in equal proportions, are included. In the first, the Pomeron is assumed to couple to valence quarks, so that the string is stretched directly between the struck quark and the remnant antiquark of the diffractive state. In the second, the interaction is rather with gluon, so that the string is stretched from the quark to a gluon and then back to antiquark inside a dissociated system. For simplicity this string is aligned along the γp interaction axis. The quark and antiquark share the momentum along the photon direction. The string itself fragments into hadrons. This model, though based on a partonic picture, doesn’t include hard scattering between partons from the photon and from the proton or Pomeron. The differential cross-section for diffractive events follows the properties known from hadronic diffractive dissociation [74], namely an exponential t dependence and a $1/M_X^2$ behavior (see Eq.(3.33)). Here t is the four momentum transfer between the incident particles and M_X is the invariant mass of the dissociated system.

The spectrum of the dissociation mass M_X is taken to begin at 0.28 GeV ($\approx 2m_\pi$) above the mass of the respective incoming particle and extends to the kinematical limit. The simple $1/M_X^2$ behavior is modified by the mass dependence in the diffractive slope [22]. This model reproduces the kinematic properties of a longitudinal phase space model. Henceforth it is referred to as the *soft diffractive model*.

3.6.2 PHOJET

The PHOJET event generator [75] is designed to simulate all components which contribute to the photoproduction total cross-section on the basis of unitarization of soft and

hard processes. PHOJET is based on the two-component Dual Parton Model (DPM) [76] incorporating soft hadronic processes, described by the ‘supercritical’ Pomeron (Eq.(3.39)), and hard processes, described by perturbative constituent scattering. Previous studies [77] have shown that the DPM successfully describes most features of high energy hadronic processes, for example, the long range correlations, violation of KNO scaling, multiplicity–transverse momentum correlations etc. The free parameters of the model have been tuned using the results from proton–antiproton collisions and low energy photoproduction cross–section measurements.

The ep frame and full γp kinematics is realized in the framework of the IJRAY [65] generator for the photon flux. The hard processes are calculated using standard parton distribution functions together with LO QCD matrix elements (Eq.(3.22) and Table 3.1). The lower transverse momentum cut-off is $\hat{p}_T \geq 3 \text{ GeV}$. Due to the unitarization scheme, small variations of this cut-off parameter do not have a large influence on the results of this generator. Initial state radiation is not generated in this version of PHOJET because it is mainly included in the generation of soft part. Final state radiation is generated using JETSET [66].

The leading contribution to the soft interaction is represented by two strings stretched between valence quark of the colliding proton and antiquark of the resolved hadronic state of the photon and between the remaining quark of the photon and diquark of the proton. In addition multiple soft scattering is simulated by further strings stretched between the sea quarks of the photon and proton. The transverse momenta of partons belonging to soft chain are assumed to be distributed according to

$$\frac{dN_{soft}}{dp_T} \sim \exp(-\beta \cdot p_T) \quad (3.46)$$

The slope parameter β follows the requirement to have a smooth transition between the soft and the hard scattered partons,

$$\left. \frac{dN_{soft}}{dp_T} \right|_{p_T=p_T^{cut-off}} = \left. \frac{dN_{hard}}{dp_T} \right|_{p_T=p_T^{cut-off}} \quad (3.47)$$

The characteristic feature of this model are multiple soft and hard interactions. The multiplicities of soft and hard interactions are calculated within unitarization scheme [78]. The average number of interactions in non-diffractive events in the energy range of HERA is estimated to be about 1.7 interactions per event. The details concerning the calculation of cross–sections for different configurations of the final state are given in [78, 77]. GRV-LO parametrizations were used for the proton and photon structure functions. For the fragmentation process the JETSET program is used.

3.6.3 HERWIG

HERWIG (versions 5.7 and 5.8 were used) is a general purpose event generator for high energy hadronic processes, with particular emphasis on the detailed simulation of QCD

showers [79]. The emission of the quasi-real photons by electrons is generated according to the equivalent photon approximation (Eq.(3.17)). For the photon and proton distribution functions the GRV-LO [46, 47] parametrizations have been used.

The generation of the hard hadron-hadron interactions in HERWIG is to some extent similar to the PYTHIA generator. The hard parton-parton interactions are simulated according to LO QCD calculations (Eq.(3.22) and Table 3.1). HERWIG includes a parton shower model which allows for interference effects between the initial and final state showers. The renormalization and factorization scales were set according to the transverse momentum of the scattered partons with a cut-off at $\hat{p}_T \leq 2 \text{ GeV}$. α_s was calculated to first order using $\Lambda_{QCD} = 180 \text{ MeV}$ for 5 flavours.

The major difference between HERWIG and PYTHIA generators is the difference in the hadronisation models. HERWIG uses the cluster hadronisation algorithm. In this scheme, after the perturbative stage of parton generation, all final gluons are split non-perturbatively into essentially light (u or d) quark and antiquark pairs. Quark and antiquark (or diquark) pairs are combined into colorless cluster. A heavy clusters can be divided into two light clusters first. Finally all clusters decay into hadrons. The parameter CLMAX which sets in HERWIG the cluster mass threshold for which phase space decay is allowed was set equal to 3.0 GeV . Another important user-defined parameters are: PSPLT=0.5, which determines the mass distribution in the cluster splitting; the minimum intrinsic transverse momentum of the quarks in a proton 0.7 GeV ; QSPAC=2.0 cut-off in Q^2 for the structure functions below which non-valence constituents are forced to evolve into valence partons; BTCLM=1.0 which determines the splitting of the beam and target cluster.

For a certain fraction of generated events the interaction between the “beam clusters” containing the spectators from the incoming hadrons is allowed. This *soft underlying event* technique is a phenomenological approach based on minimum bias $p\bar{p}$ events from UA5 [80]. The main motivation to add this option was to correctly describe the distribution of soft hadrons in the hadronic CMS. The necessity of adding this option comes also from the analysis of the “pedestal height” in hadronic jet production. The observed pedestal height and its dependence on jet transverse energy [71] are accounted for by superposing on the hard emission an underlying event structure similar to that of a minimum-bias collision. Since the production of most of these low- p_T hadrons is related to the remnant proton fragmentation, the soft underlying event provides the possibility to add these particles to the event. It generates many “soft” clusters per event. The cluster momenta are generated with a simple longitudinal phase-space distribution and limited transverse momenta. Next the clusters are fragmented into the hadrons using the same cluster fragmentation algorithm as mentioned above. After tuning, these soft underlying events were applied for 35% of the resolved photon-proton interactions.

3.6.4 POMPYT

The POMPYT 1.0 [57] model was used for generating hard scattering interactions in the γp diffractive processes following ideas of Ingelman and Schlein (for details see section 3.5).

POMPYT is a Monte-Carlo model in which, within the framework provided by PYTHIA, the proton emits a Pomeron whose partonic constituents subsequently take part in a hard interaction process with the photon or its constituents. The Feynman- x variable is generated in the range $0.9 < x_F < 0.9999$ and the effective mass of the dissociated system is generated in the range $2.9 < M_X < 93.6 \text{ GeV}$. The Pomeron flux is given by the Eq.(3.36).

In this analysis the Pomeron was assumed to consist of gluons and their distribution function within the Pomeron was taken to be either “hard”, $zg(z) \sim z(1-z)$, or “soft”, $zg(z) \sim (1-z)^5$. The variable $z = x_{g/P}$ is the fraction of the Pomeron momentum carried by the struck gluon involved in the interaction.

The resulting photon-Pomeron interaction is simulated as the hard scattering of the photon (direct process) or partons in the photon (resolved process) with partons in the Pomeron according to LO QCD calculations for the hard scattering processes. The minimum transverse momentum cut-off \hat{p}_T^{min} was set to 2.0 GeV . The Drees-Grassie parametrization was used for the parton density distribution in the photon.

Chapter 4

The Data Sample

In the quasi-real photoproduction interactions at HERA the electron is scattered at small angles $\theta \lesssim 5^\circ$ and is not seen in the main detectors. For these events the squared four-momentum transfer $Q^2 = 4E_e E'_e \cos^2(\theta_e/2) \lesssim 4 \text{ GeV}^2$, where E_e and E'_e are the energies of the incoming and scattered electrons respectively and θ_e is the electron scattering angle with respect to the proton direction. The energy of the interacting photon can be reconstructed from the final state hadrons measured in the detector:

$$E_\gamma = \sum_{\text{hadrons}} (E_h - p_{z,h})/2, \quad (4.1)$$

where E_h and $p_{z,h}$ are the energy and longitudinal momentum of the hadron, respectively. In practice, the sum over $(E_h - p_{z,h})$ is substituted by summing over $(E - E \cdot \cos\theta)$ of the calorimeter cells (or clusters) and tracks, assuming that the interaction vertex is known.

$$\sum_{\text{hadrons}} (E_h - p_{z,h})/2 \approx \sum_{\text{cells,tracks}} (E_i - E_i \cdot \cos\theta)/2 \quad (4.2)$$

In some cases, when the electron scattering angle is of the order of a few *mrad*, it can be detected in the H1 small angle electron detector. For these events, henceforth called *tagged*, the acceptances for the virtuality of the incident photons Q^2 and for the fractional momentum of photon y are limited to the range $3 \times 10^{-8} \text{ GeV}^2 < Q^2 < 10^{-2} \text{ GeV}^2$ and $0.2 < y < 0.8$, respectively, as shown in Fig.4.1. The energy of the photon can be determined with good precision as a difference between the electron beam energy and the energy detected in the electron detector $E_\gamma \approx E_e - E'_e$.

Only *tagged* events have been used for the analysis presented here. In addition to the tagged electron some activity in the main H1 detector, in the form of at least one charged track with transverse momentum $p_T \lesssim 150 \text{ MeV}$ was required already at the hardware trigger level (see section 4.1.1). The requirement of e^- -detector signal suppressed the background from proton-gas and proton-wall background by about two orders of magnitude and ensured a sufficiently low rate for this trigger during data taking. In addition using a *tagged* sample allows for a much more precise measurement of E_γ (see below).

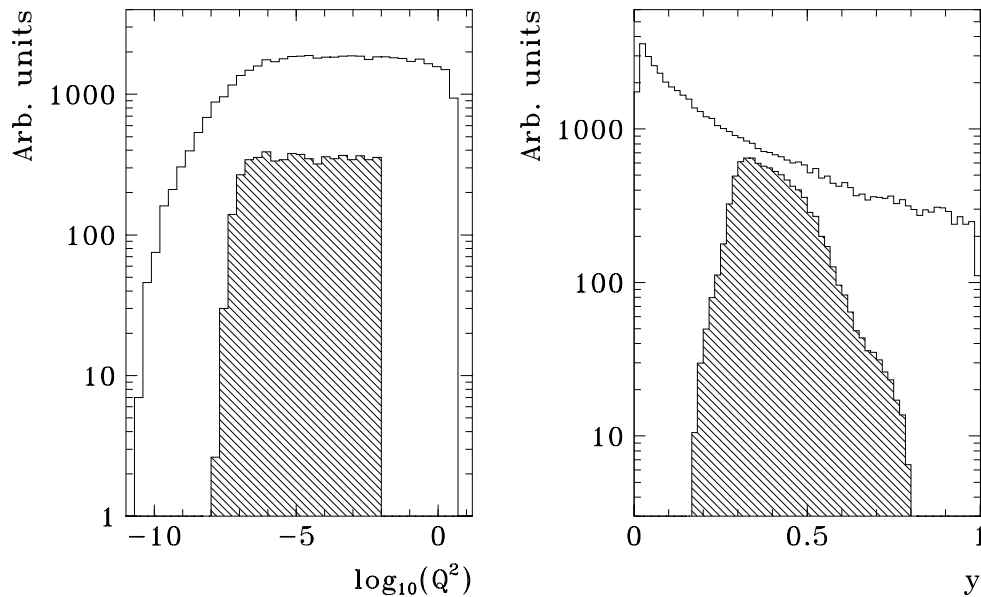


Figure 4.1: The distributions of the kinematic variables Q^2 and y for Monte-Carlo events, generated in the kinematical region $10^{-12} \text{ GeV}^2 < Q^2 < 4 \text{ GeV}^2$ and $0.01 < y < 1$, and for events with a scattered electron detected in the electron detector (hatched histograms).

In this chapter all selection steps of the tagged photoproduction event samples are described. These samples are used for the jet search in the inclusive jet cross-section analysis (chapter 5) and for the diffractive photoproduction analysis (chapter 6).

These studies are based on the data taken by H1 during the 1993 running period and correspond to a total integrated luminosity $\int L dt \approx 289 \text{ nb}^{-1}$.

4.1 Trigger

The purpose of the trigger system is to select interesting ep collision events and to reject background events. The main sources of background are: synchrotron radiation from the electron beam, proton gas interaction in the beam pipe vacuum of about 10^{-9} mbar and stray protons, which produce particle showers by hitting the beam tube and other apertures around the accelerator.

As a consequence of the background situation, the short bunch time interval of 96 ns and the request for low dead-time of the readout system, the four-level H1 trigger system was proposed. In 1993 only the first and fourth trigger levels were available. The first decision is made by the hardware first level trigger (L1) which use the logical signals

(trigger elements) from the different subdetectors. These trigger elements are fed to a central trigger logic where they are combined to various so called subtriggers. The events which passed first trigger level are partially reconstructed and filtered by the so called “filter farm” (or L4 trigger). The filter farm is a software trigger based on the fast MIPS R3000 processor boards [8]. It is integrated into the central data acquisition system and has the raw data of the full event available as a basis for its decision algorithms. In 1993 fourteen processor boards ran in parallel. Each board processes one event completely until a decision is reached. The filter farm it is also well suited for monitoring and calibration.

4.1.1 L1-trigger

For analysis two data samples have been selected. The first one, henceforth called *minimum bias sample*, has been collected with a loose, so called minimum bias trigger, designed for collecting events for general multiparticle studies of γp collisions. This trigger requires a coincidence of the signal from electron detector with a t_0 signal derived from central and forward proportional chambers (**ETAG** \times **ZVTX** – **t0**). A second data sample, henceforth called *high E_T sample*, was collected with a more selective trigger, which requires in addition to the minimum bias trigger fast signals of the central drift chamber trigger (**ETAG** \times **DC** – **r φ** – **a** \times **ZVTX** – **t0**).

Below, the trigger elements used in the mentioned triggers are briefly described.

- **ETAG**–trigger element requires the energy deposited in the electron detector of the luminosity system to be $E_{e'} > 4 \text{ GeV}$ and energy in the Water-Čerenkov photon detector to be $E_\gamma < 2 \text{ GeV}$. The last condition is aimed to reduce the high background rate from the bremsstrahlung events $ep \rightarrow ep\gamma$ having a typical rate of a few kHz for the events with $E_{e'} > 4 \text{ GeV}$. The efficiencies of the luminosity trigger elements (electron trigger, photon trigger, ETAG trigger) are shown in Fig.4.2 as function of reconstructed energies. The efficiencies of electron and photon detectors are close to 100% for corresponding energies above 8 GeV . The efficiency of the ETAG trigger element is somewhat smaller due to accidental coincidences between PD and VC from bremsstrahlung processes. This inefficiency enters into the systematic errors of luminosity calculation.
- The aim of the **ZVTX** trigger is to reconstruct the primary interaction vertex along the beam axis, the z -coordinate. The trigger signals are derived by six central and forward multiwire proportional chamber layers (four central layers CIP, COP and the first two layers of the FPC). A particle originating from the beam passes four layers of chambers either the double layers of CIP and COP or CIP and the first forward proportional chamber. Then four cathode pad signals which lie on a straight line on the $r - z$ plane are combined into an object called ray.¹

In the plane perpendicular to the beam, a 16 fold segmentation (φ –sectors) is used,

¹During 1993 running central proportional chambers CIP and COP contained some dead φ sectors. For them the coincidence of 3 out of 4 pads have been required in order to construct the “ray”.

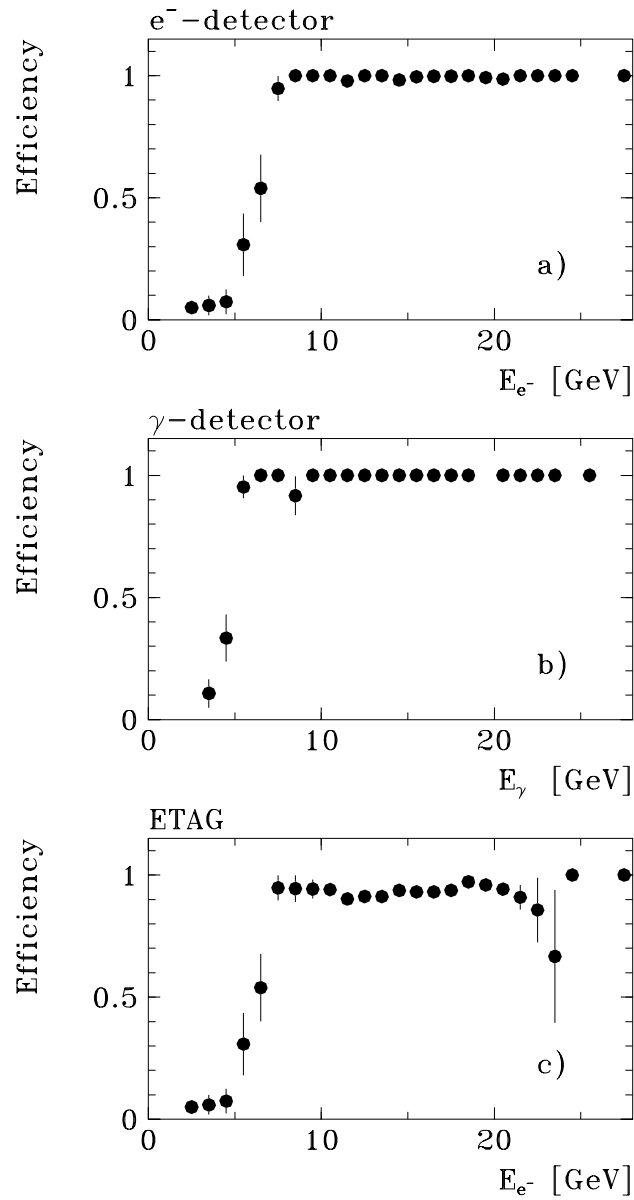


Figure 4.2: Efficiencies of ETAG trigger elements with respect to the trigger based only on the central tracker: **a)** Electron detector, **b)** Photon detector, **c)** ETAG.

such that the rays of each segment are treated separately. Therefore tracks with small transverse momenta ($p_T \lesssim 150 \text{ MeV}$), i.e. large curvature, can not produce a ray. If the intercept of a ray with the z axis is within $\pm 44 \text{ cm}$ of the nominal interaction point, it enters into a histogram with 16 bins along z with a bin width of 5.4 cm , which is filled according to the z -coordinate of the origin of each ray. The rays which are formed by the combinations of pads associated with the real particles all enter in the same bin and form a significant peak above the background

entries, which originate from rays from wrong combinations of pads and are therefore randomly distributed. The **ZVTX-t0** trigger element is activated, if there is at least one entry in the histogram. This information is used as an indication, that there is at least some activity in the central region of H1. Since multiwire proportional chambers provide good time resolution, ZVTX-t0 is also used to identify the bunch crossing, when the detected interaction happened (so called event-t0).

- The **DC – r φ** trigger provides a rough track recognition in the central jet chambers (inner and outer CJC) in the plane transverse to the ep interaction axis. Only the tracks which have a distance of closest approach (DCA) from the nominal beam axis less than 2 cm are considered as “trigger roads”. This allows to suppress beam-wall events as well as synchrotron radiation background. To keep the logic reasonably small and without degrading the performance significantly only 10 out of 56 signal wire layers of the CJC are used in the trigger. First, the signals from the CJC are digitized and serially clocked into shift-registers by the HERA clock. The drift-time information is kept with an accuracy of 96 ns or about 5 mm of position resolution. Then, about 10000 track masks which are defined according to their position in the drift-space and their curvature in the magnetic field, are applied to the outputs of the shift-registers to mark the active roads. This algorithm can recognize tracks with a transverse momentum $p_T \gtrsim 450 \text{ MeV}$ and a polar angular interval of $25^\circ < \theta < 155^\circ$. Tracks with low ($p_T \lesssim 800 \text{ MeV}$) or high ($p_T \gtrsim 800 \text{ MeV}$) transverse momentum can be distinguished as well as the sign of the low momentum tracks. In addition a topological analysis in the $x - y$ plane is performed, for instance track activities in region of opposite φ are recognized. Finally track counts are processed to generate trigger elements. For trigger **DC – r φ – a** used in the present analysis at least one track was required.
- In addition a veto signal delivered from the time-of-flight scintillators is required (**TOF – BG**). Beam-wall and beam-gas events originating from the proton upstream direction ($z \lesssim -2 \text{ m}$) can produce showers, which mostly run through both scintillator. Background (BG) and interaction (IA) timing windows (defined relative to the HERA clock signal) define for each scintillator of each wall whether the hits belong to particles originating from upstream or from the nominal interaction region. The signals from the single scintillators of each wall are “ORed” together to form a signal for each plane, and the two planes are then put into coincidence forming the final **TOF – BG** and **TOF – IA** trigger elements. If there are corresponding BG signals in both walls, the event is rejected.

A typical rate for **ETAG \times DC – r φ – a \times ZVTX – t0** trigger was a few Hz in the data collecting period used in the present analysis. This trigger permitted the use of a data sample corresponding to an integrated luminosity of 289 nb^{-1} . The rate of **ETAG \times ZVTX – t0** was $\sim 5 - 6$ times higher. In order to reduce the dead-time due to the high rate, for this trigger prescaling factors between 1 and 20 have been introduced. Therefore, the equivalent integrated luminosity for the minimum bias sample is smaller, namely $\sim 120 \text{ nb}^{-1}$.

4.1.2 L4-trigger or Filter farm

The sample selected after the L1 trigger contains a large number of background events due to an accidental coincidence of a beam-wall or beam-gas interaction with an electron scattered at small angle and detected in the electron detector. A significant part of the background is rejected already on-line by the level 4 trigger. The L4 modules use either fast algorithms designed specifically for the filter farm, or contain parts of the standard off-line reconstruction program.

The typical reduction factor which the filter farm achieved in 1993 was $\sim 5 - 6$. A small fraction— typically 1%— of all L4 rejected events was kept for monitoring purposes.

The dominant part of the proton beam interactions with the beam-pipe originate very far upstream from the interaction point. Such events are suppressed requiring

- at least one reconstructed track in the central jet chambers—(CJC) pointing into the central region ($|z_{track}| < 60 \text{ cm}$)
- less than 3 tracks coming from upstream ($z_{track} < -100 \text{ cm}$),
- the fraction of tracks in central region to be more than 50% of all tracks.

For rejection of beam-gas background events originating in the interaction region, a cut on two following reconstructed quantities is used. One of such variable is y , which is in the rest frame of the proton the ratio of electron energy transfered to the hadronic system to the total electron energy. For the photoproduction events y is with the good approximation the fractional energy carried by the photon $y = E_\gamma/E_e$. y can be reconstructed either from measured energy of scattered electron

$$y_e \approx 1 - E'_e/E_e \quad (4.3)$$

(if scattered electron is detected in electron detector), or from the final state particles (Jacquet-Blondel method)

$$y_h = \sum (E - p_z)/2E_e, \quad (4.4)$$

where p_z denotes the longitudinal momentum component. $\sum (E - p_z)$ is determined by summing $E \cdot (1 - \cos \theta)$ of all calorimeter cells and reconstructed tracks. The calorimeter cells behind the tracks have been masked to avoid double counting of energy.

For simulated events Fig.4.3a and Fig.4.3c depict the relative difference $(y_{gen} - y_e)/y_{gen}$ and $(y_{gen} - y_h)/y_{gen}$ between the true and reconstructed values of y , using the electron and Jacquet-Blondel methods. The reconstructed y_e agrees well with the generated value with a resolution of about 4%. The y_h is systematically smaller than the true value by about $\sim 45\%$ with a resolution of $\sim 25\%$. This discrepancy is attributed to the poor calorimetric measurements in backward region ($\theta > 140^\circ$) (the backward region is especially important for the $(E - p_z)$ calculation) and to the noise suppression in calorimeter which influence mainly soft, i.e. low p_T events. With increasing of the total E_T in event the difference between y_{gen} and y_h becomes smaller (see Fig.4.3a and Fig.4.3b). Fig.4.3d shows the

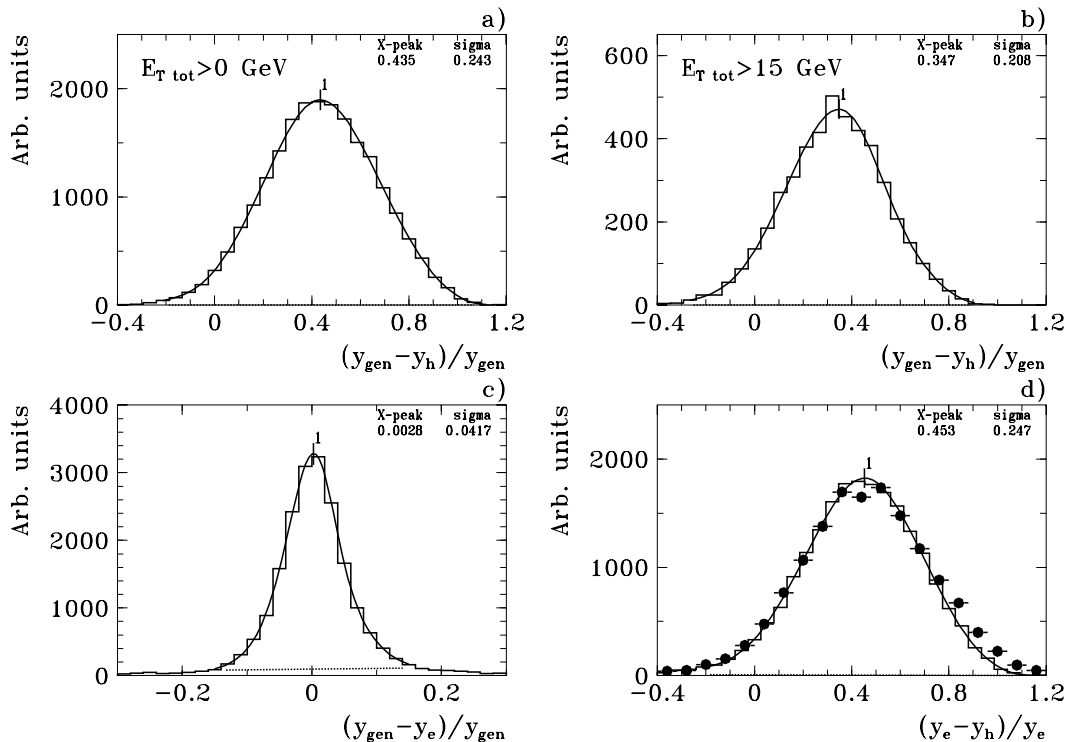


Figure 4.3: **a)** The relative difference between the generated y_{gen} and y_h , reconstructed by Jacquet-Blondel method (from PYTHIA Monte-Carlo);
b) same as **a)** but for $E_T > 15$ GeV;
c) The relative difference between the generated y_{gen} and y_e , reconstructed from the electron detector method;
d) The relative difference between y_h reconstructed by Jacquet-Blondel method and by electron detector method y_e .

Points represent data, histograms are PYTHIA MC predictions and curves are the fits of Monte-Carlo histograms.

relative difference $(y_e - y_h)/y_e$ for the data and the PYTHIA predictions. The results of data and Monte-Carlo compare well.

For background events, i.e. events originating from a accidental coincidence of proton-gas interaction with a electron scattered at small angle and detected in the electron detector, reconstructed y_e and y_h are not correlated. From simple kinematical reason, $\sum(E - p_Z)$ for these events is expected to be small, namely of order of nuclei mass instead of $2E_\gamma$ for photoproduction events (see Eq.(4.4)), and therefore $y_h \sim 0$.

Another variable, which is used for background separation is the ratio $\sum p_Z / \sum p$, which for background events is expected to be large, near to 1, due to the large Lorentz boost. Again, summation is performed over tracks and calorimeter cells.

The background sample, which contains events coming from the so called proton pilot bunches with no electron bunch partner was used in order to define cuts on y_h and $\sum p_z / \sum p$. The event distribution of these variables for the background sample compared to the photoproduction events from Monte-Carlo simulation is shown in Figure 4.4.

It was found, that using the logical combinations of cuts

$$(y_h < 0.05 \text{ .AND. } \sum p_z / \sum p > 0.6) \text{ .OR. } (y_h < 0.15 \text{ .AND. } \sum p_z / \sum p > 0.9)$$

about 85% of the beam-gas background can be removed, keeping more than 98% of the γp interaction events.

The efficiency of L4 cuts was studied using a sample of L4-rejected events (1% of all rejected events). The influence of L4 on the final selection is expected to be small, because most of the L4-rejection criteria are used in further selection steps as well. It was found that less than 1% of the *high* E_T sample and about 2% of minimum bias sample have been rejected by L4.

4.2 Reconstruction and event classification

Events accepted by level 4 trigger pass full H1 reconstruction and event classification programs. In this step the full information from all H1 subdetectors is available, as well as the final calibration constants.

The event classification program combines all reconstructed information and defines simple criteria, which are used for classifying an event into physics or background classes. Several classes are defined, for example low and high Q^2 deep inelastic scattering, heavy quark physics, physics beyond the standard model, high E_T and minimum bias photoproduction, etc. Events which are classified as candidates for physics analysis are kept on data storage tapes (DST). Those events, which do not belong to any physics class are rejected. It allows to reduce the event rate by about a factor 2.

As a first step, the obvious background events are recognized and removed. Events containing cosmic ray showers are rejected by means of patterns recognized in the central tracking and muon systems. The dE/dx information from CJC is used for recognition of low energy protons, originating from proton-gas interactions. Events are rejected if more than 3 of such protons are found. Muons from proton-beam halo penetrate the calorimeter almost parallel to the beam axis and leave their energy in many calorimeter cells with nearly the same radius and azimuthal angle. Therefore, events containing such halo-muons can be recognized and rejected. The beam interactions with the beam-pipe have usually interaction vertex far from beam axis. Events, where the distance between the reconstructed vertex and the beam axis in the (x, y) plane is more than 6 cm, are rejected. The beam-gas finder, described in the previous section, is used in event classification as well, but here, in difference to L4 it uses the results of complete reconstruction program.

Further, the events are classified as minimum bias photoproduction candidates, if the reconstructed energy in the electron detector $E_{e-\text{detector}} = E_{e'}$ is higher than 4 GeV,

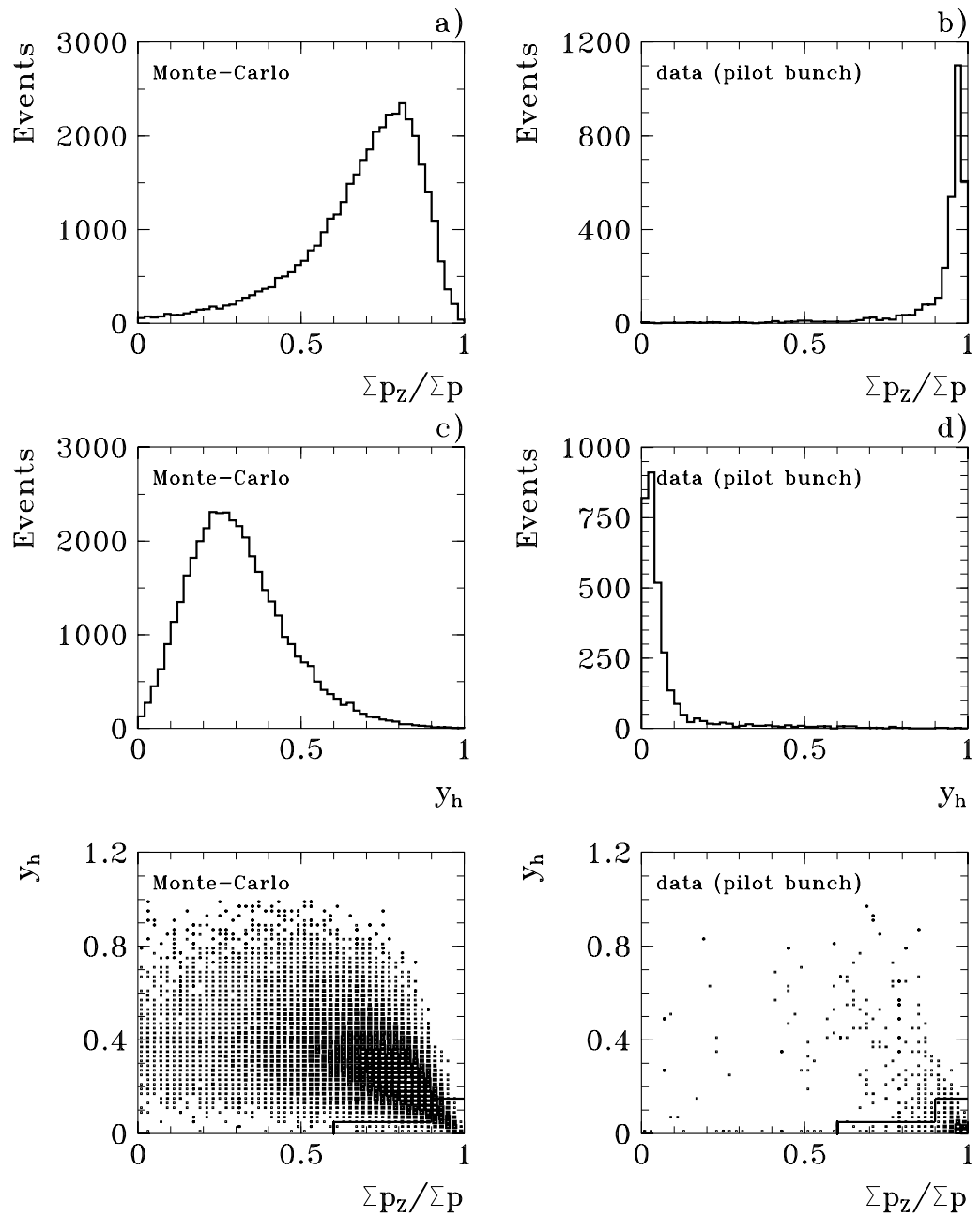


Figure 4.4: The distributions of $\Sigma p_z / \Sigma p$, y_h and the scatter plot $\Sigma p_z / \Sigma p$ vs y_h for minimum bias Monte-Carlo (a,c,e) and for the background events (b,d,f). The cuts applied for the proton-gas background rejection are indicated in the figures (e,f) by the solid line.

the energy in the photon detector of luminosity system $E_{\gamma-detector}$ is less than 2 GeV and at least one track originated from the interaction region in the transverse (x, y) plane is found.

In total $\sim 360,000$ events satisfied the minimum bias photoproduction criteria.²

4.3 Final selections

In the next selection step the fractional energy of the photon as measured by the electron detector is required to be in the interval $0.25 < y < 0.7$, where $y = 1 - E_{e'}/E_e$, or equivalently the scattered electron energy to be between 8 and 20 GeV . This condition removes events from the tails of the electron energy distribution where the geometrical acceptance of the electron detector is small, namely less than $7\text{--}8\%$ (see Fig.4.5b).

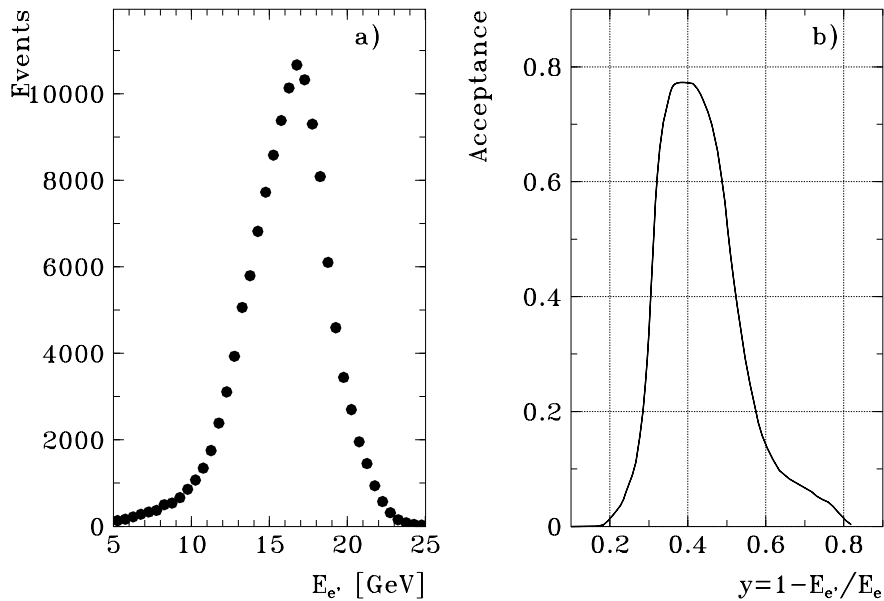


Figure 4.5: a) the measured spectrum of scattered electron for the minimum bias sample; b) the geometrical acceptance of electron detector.

This range of y corresponds to an energy interval of the γp system (W) from 150 GeV to 250 GeV , with an average of about 200 GeV .

In addition, events should contain at least one track with transverse momentum $p_T \geq 300 \text{ MeV}$ originated from the interaction region in the transverse (x, y) plane.

²In 1993 these events were assigned to DST class 19.

The distance of closest approach (DCA) from the z -axis for this track should be smaller than 2 cm , which rejects additional beam-wall and beam-gas background. In Fig.4.6 is shown the distribution of the z -vertex reconstructed from tracks. The curves on this plot are results of the Monte-Carlo simulation and of a Gaussian fit. The z -vertex distribution has a Gaussian shape with a mean value $\sim -5.3\text{ cm}$ and width $\sim 10\text{ cm}$. In addition one can see the small peak from the satellite proton bunch with $z \approx 54.4\text{ cm}$ and $\sigma \approx 12.3\text{ cm}$. For the final event sample the z -vertex was required to lie in a region of ± 3 standard deviations around the nominal vertex position, the length of which is governed by the total proton bunch length ($-35 < z_V < 25\text{ cm}$). This cut removes the events from satellite bunches. Since the satellite bunches are taken into account for luminosity calculation, the final luminosity has to be corrected by $\sim 3\%$. Also $\sim 0.3\%$ of events from “main” proton bunches are removed by this cut, it also has to be taken into account in luminosity correction.

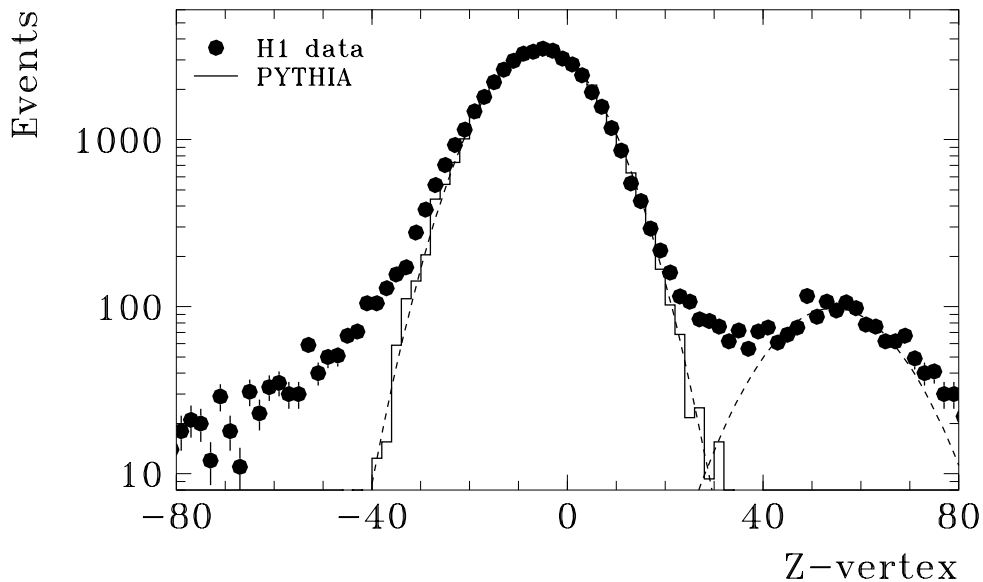


Figure 4.6: z -vertex spectrum for data and PYTHIA-minimum bias MC. The dashed lines are the result of a Gaussian fit (see text).

In addition, a *high* E_T sample is selected, where the events are required to contain a minimum transverse energy, E_T , of 5 GeV .

In total about 125,000 events satisfy the final selection criteria for the minimum bias sample and 174,000 events for the *high* E_T sample.

Since the precision of the scattered electron energy and coordinate reconstruction is not good enough in the areas close to the boundaries of the electron detector $x_{el} = \pm 7.7\text{ cm}$, for the sample used to determine the inclusive jet cross sections an additional fiducial cut

$|x_{el}| \leq 6.5$ cm was applied (see Fig.4.7). About 147,000 events from the high E_T sample survive this cut.

After all corrections the total integrated luminosity for the *high* E_T sample was

$$\int L dt \approx 279.3 \text{ nb}^{-1},$$

and for the minimum bias sample was

$$\int L dt \approx 117.0 \text{ nb}^{-1},$$

with $\sim 5\%$ of systematic uncertainty.

The event selection is summarized in the Table 4.1.

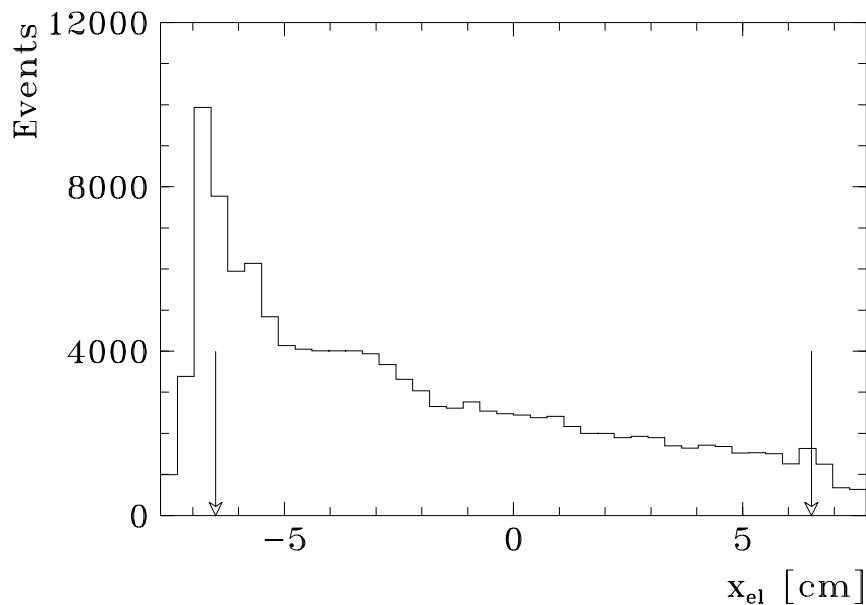


Figure 4.7: The distribution of the x coordinate of the electron in the electron detector. The arrows indicate the fiducial cut.

4.4 Background

The contamination of electron-beam or proton-beam induced background in the selected samples can be studied using events coming from electron or proton pilot bunches, respectively. The total number of expected background events will be:

$$N_{p\text{-background}} = \sum_i R_i^p \times N_i^{p\text{-pilot}}, \quad N_{e\text{-background}} = \sum_i R_i^e \times N_i^{e\text{-pilot}},$$

where R_i^e and R_i^p denote the ratios of the total beam current to the pilot bunch current for a given run i and $N_i^{e^- - pilot}$ and $N_i^{p - pilot}$ are the numbers of observed events in the pilot bunches.

Background events induced by electrons are almost completely suppressed by requiring at least one reconstructed track in the central tracker already at L4-level. For 1993 running conditions $\langle R_i^e \rangle \approx 8.3$. The number of $e^- - pilot$ bunch events is 69 for the minimum bias sample and 5 for the high E_T sample. Therefore, the electron induced background is only $0.49 \pm 0.06\%$ and $0.025 \pm 0.01\%$ for these samples, respectively.

The background from the interactions of the proton beam with the residual gas in the fiducial vertex region in random coincidence with a signal in the electron detector is expected to be more significant. This background cannot be studied in the same way as the electron induced background, i.e. using events from the proton pilot bunches in this sample, because our selections required a scattered electron and therefore events from proton pilot-bunches are excluded.

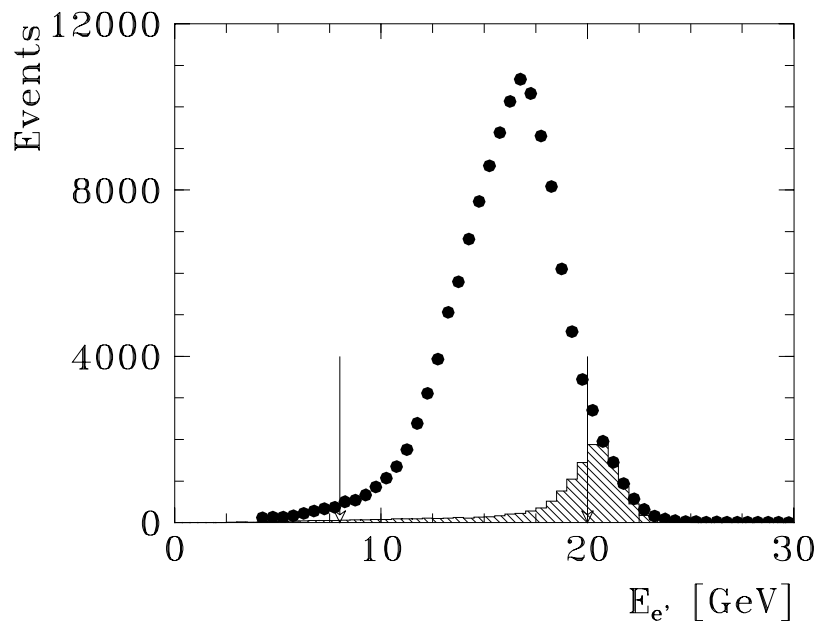


Figure 4.8: The measured energy spectrum of scattered electron for minimum bias events (points) and for background (hatched histogram). Arrows indicate the cut applied on $E_{e'}$.

A rough estimate of this background can be made by analyzing the energy spectrum of the scattered electron. The distribution for minimum bias events is shown in Fig.4.8 (but without any cut on $E_{e'}$). The hatched histogram is the energy spectrum measured by the electron detector alone, i.e. independent of the other H1-detector components.

The latter spectrum is shifted towards high $E_{e'}$ with respect to minimum bias γp events and has a strong peak around $E_{e'} \approx 21 - 22 \text{ GeV}$. In order to estimate the upper limit of the remaining background of the accidental coincidence of a proton beam gas interaction with the signal in the electron detector, one can make the assumption that all events with high $E_{e'}$ are background. Therefore, in this plot the background spectrum is normalized to the number of events with $E_{e'} > 21 \text{ GeV}$ in the selected sample. From this plot one can see that a cut $E_{e'} < 20 \text{ GeV}$ removes a significant part of the background. After the cut $8 \text{ GeV} < E_{e'} < 20 \text{ GeV}$ the remaining background is estimated to be less than 4%.

This number overestimates the background, because as we will see from the comparison of $E_{e'}$ spectrum for data and PYTHIA Monte-Carlo (Fig.5.2), a significant fraction of events with $y < 0.25$ ($E_{e'} > 20 \text{ GeV}$) originates from photon-proton interactions.

step	min.bias sample	high E_T sample
L1-trigger	$ETAG \times t0$	$ETAG \times DC - r\varphi - a \times t0$
L4-trigger	≥ 1 track with $ z_{track} < 60 \text{ cm}$, $N_{tracks z_{track} < 60 \text{ cm}} / N_{all \text{ tracks}} \geq 0.5$, ≤ 2 tracks with $z_{track} < 100 \text{ cm}$, no beam-gas candidate	
Event classification (L5)	no background candidate, ≥ 1 track, $E_{e^- - detector} > 4 \text{ GeV}$, $E_{\gamma - detector} < 2 \text{ GeV}$	
Final selection	$8 \text{ GeV} < E_{e^- - detector} < 20 \text{ GeV}$ $-35 \text{ cm} < z_V < 25 \text{ cm}$	$8 \text{ GeV} < E_{e^- - detector} < 20 \text{ GeV}$ $-35 \text{ cm} < z_V < 25 \text{ cm}$ $E_{T \text{ total}} > 5 \text{ GeV}$ $(x_{el} \leq 6.5 \text{ cm})^*$
Luminosity $\int Ldt$	117.0 nb^{-1}	279.3 nb^{-1}
Events	125,000	174,000 147,000*

Table 4.1: Summary of the data selection.

Chapter 5

Measurement of the Inclusive Jet Cross-Section in Photoproduction

5.1 Jet algorithm

For the jet search, a cone-type jet algorithm was applied to all photoproduction events which passed the above selection criteria. The cone algorithm follows the Snowmass convention [81]. It was originally developed for the analysis of $p\bar{p}$ collider data by the UA1 collaboration [82]. The definition of the jet is based on the energy deposition within a cone with radius $R = \sqrt{\Delta\eta^2 + \Delta\varphi^2} = 1$. This (η, φ) metric has the virtue of being independent of the the longitudinal Lorentz boost to the event.

The cone jet algorithm can be understood with the help of the Figure 5.1.

The total solid angle coverage of the detector is subdivided into equal cells in pseudorapidity ($\eta = -\ln \tan \frac{\theta}{2}$) and azimuthal angle (φ) with the grid 25×24 in the region $-2 \leq \eta \leq 3$ and $0 \leq \varphi \leq 2\pi$. The deposited transverse energy $E_T = E \cdot \sin\theta$ in the calorimeter (LAR and BEMC) is summed up in each grid cell.

The cell with the highest E_T is considered as possible jet initiator. A cone with radius equal 1 in the (η, φ) plane, is drawn around this cell. The cells inside this cone are used to calculate the axis and transverse energy of the cone. The transverse energy E_T in the cone is calculated as the scalar sum of transverse energy of cells within this cone. Cells with $E_T^{cell} < 50 \text{ MeV}$ are not used. The cone axis is taken to be the vector pointing from the event vertex to the transverse energy centroid of all cells within the cone.

$$E_{T \text{ cone}} = \sum_{\text{cells}} E_{T \text{ cell}} \quad (5.1)$$

$$\eta_{\text{cone}} = \frac{1}{E_{T \text{ cone}}} \sum_{\text{cells}} E_{T \text{ cell}} \times \eta_{\text{cell}} \quad (5.2)$$

$$\varphi_{\text{cone}} = \frac{1}{E_{T \text{ cone}}} \sum_{\text{cells}} E_{T \text{ cell}} \times \varphi_{\text{cell}} \quad (5.3)$$

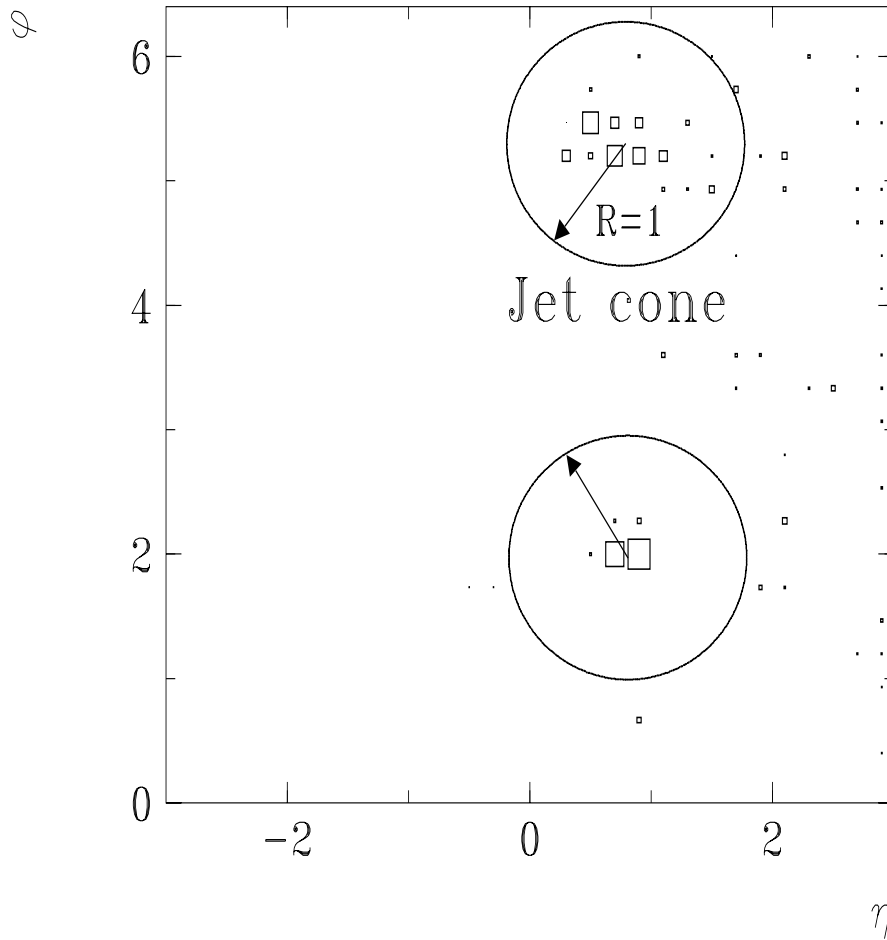


Figure 5.1: Energy distribution in a two-jet event in the η, φ plane (same event is shown in Fig.5.3).

Within the given (η, φ) region the algorithm selects the cone with the highest transverse energy in the event. If the energy of the cone is above the given threshold, it is accepted as a jet and the cells inside it are removed for the subsequent search for the next highest E_T cone in the event in order to avoid double counting of cells in different jets. This procedure is iterated until no further jet cone with E_T above threshold $E_{T_{min}}$ can be found.

For comparison with the Monte-Carlo models, the same algorithm can be applied to Monte-Carlo generated events, using instead of calorimeter cells final state particles (see below).

Within this scheme not all particles (cells) are necessarily assigned to jets.

5.2 Event sample

For the determination of the inclusive jet cross-section the jet algorithm was applied to the *high E_T sample*. Events are selected with at least one jet having a transverse energy E_T^{jet} above 7 GeV and pseudorapidity of the jet axis in the range $-1.0 < \eta^{jet} < 2.0$, (which corresponds to about $-3.3 < \eta^* < 0.1$ in the CMS of the γp system, i.e. the observed jets are mainly located in the photon hemisphere). This η^{jet} range avoids the region, where the γ -remnant jets can be misidentified as jets from the hard parton-parton interactions, and is restricted to the region where the $DC - r\varphi$ trigger efficiency is high.

The spectrum of the energy measured in the electron detector is shown in Fig.5.2 together with the result of Monte-Carlo simulation. In the range defined by our cuts ($8 < E_{e'} < 20$ GeV) the Monte-Carlo simulation gives a reasonable description of the data.

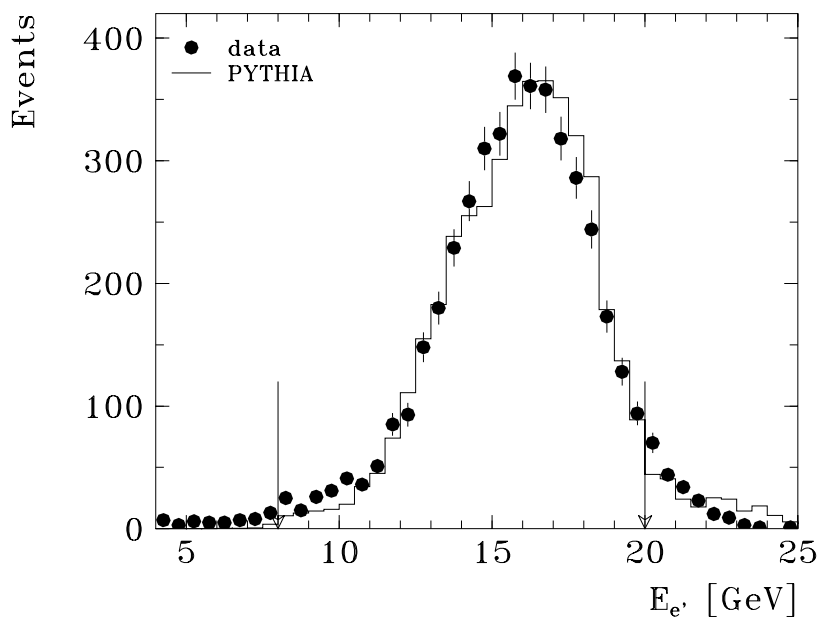


Figure 5.2: Spectrum of the energy in the electron detector for jet events in the data (points) and PYTHIA Monte-Carlo. Arrows indicate the cut used in the event selection $8 < E_{e'} < 20$ GeV.

Since in the presented analysis the radius of the jet cone $R = \sqrt{\Delta\eta^2 + \Delta\varphi^2}$ is equal to 1.0, only the LAr and BEMC cells in the pseudorapidity range $-2.0 \leq \eta^{cell} \leq 3.0$ were considered for jet search.

In total 4190 events containing 4906 jets satisfied the jet finding criteria. 3499 events (83.5%) in this sample contain 1 jet, 666 (15.9%)–2 jets, and 24 (0.6%)–3 jets. An example of an event with two jets with $E_T^{jet} \approx 20 \text{ GeV}$ is shown in Fig.5.3. The lower right picture shows the energy deposit of the electron in the electron detector.

The spectrum of jets as a function of their transverse energy and pseudorapidity is shown in Fig.5.4.

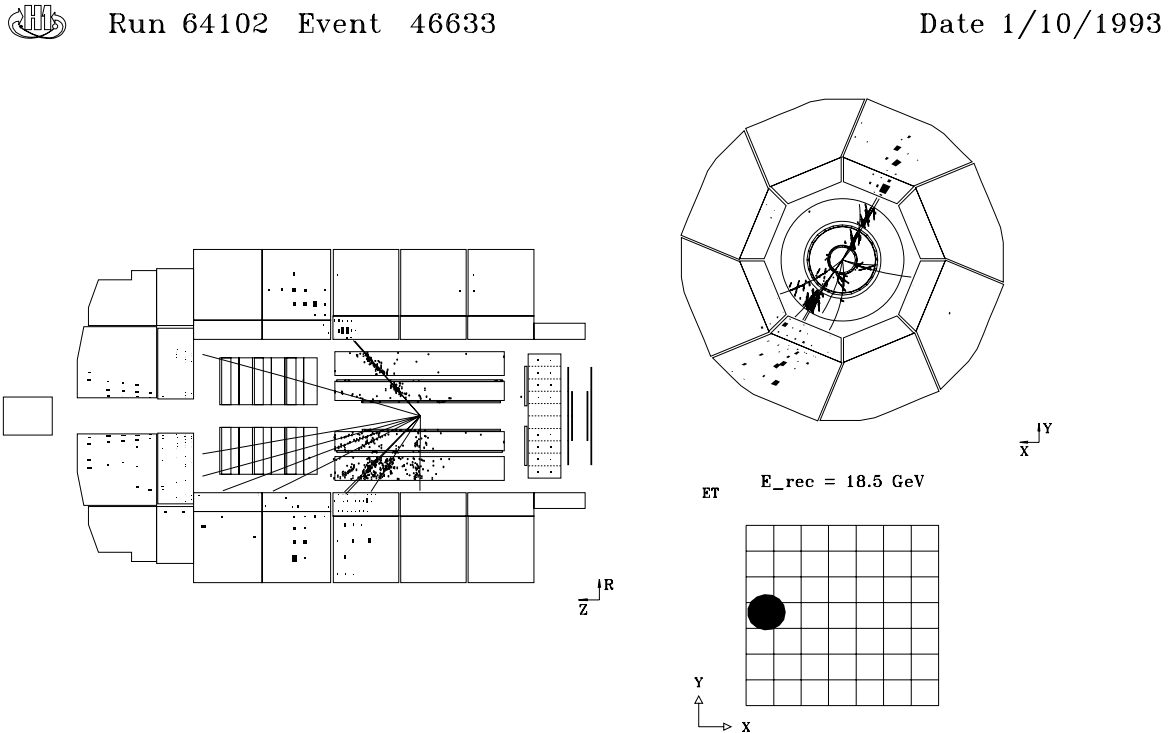


Figure 5.3: Two-jet photoproduction event in the H1-detector. Left: zR view, upper right: $R\phi$ view, lower right: ϵ^- -detector.

The background in this jet sample was studied using the same technique as for the full photoproduction sample in section 4.4. No event from an electron pilot bunch was found in the selected sample. Proton induced background was found to be less than 1% and is not considered in the following. The QED radiative corrections to the jet cross-section are expected to be small ($\lesssim 2\%$) [19] for the present experimental conditions and have not been considered in this analysis.

Before studying the jet properties, it was checked that the global variables of the events with jet structure are in agreement with the expectations of the QCD based Monte-Carlo simulations (Fig.5.5). The distributions of the total transverse energy, the transverse momenta of the most energetic track, the charge multiplicity in the central region, and the

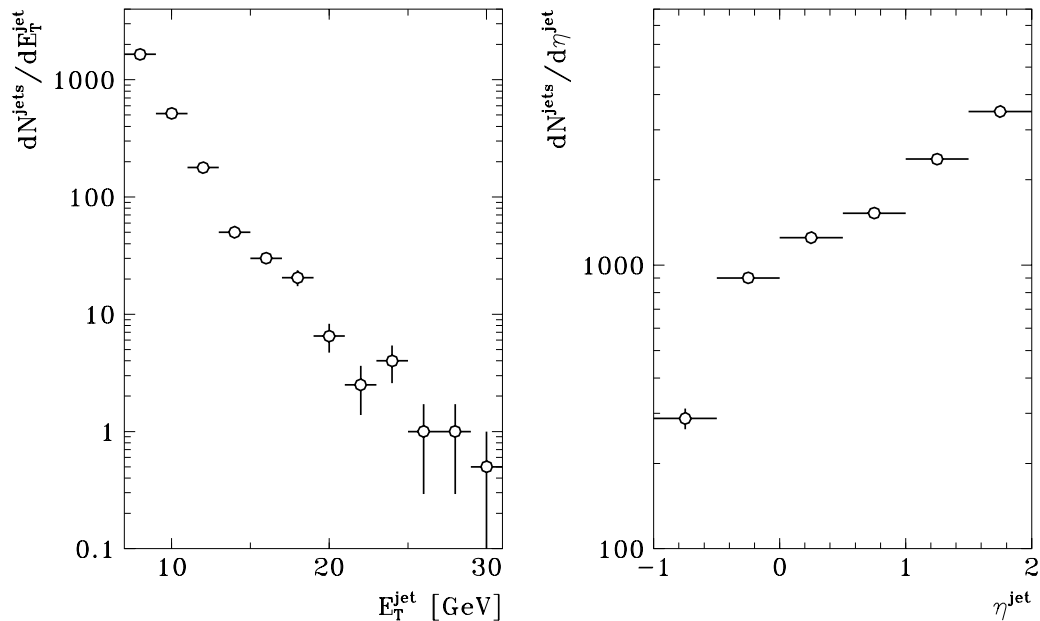


Figure 5.4: The uncorrected spectra of jets as function of E_T^{jet} (left) and η^{jet} (right).

$\Delta\varphi$ between the two jets for the 2-jet sample are compared in the data and the PYTHIA and PHOJET Monte-Carlo. In these plots the data distributions are not corrected for detector effects, but these effects are included in the detector simulation. The Monte-Carlo simulations give a good description of the global event shapes of the data. PHOJET shows a larger tail in the E_T and N_{charge} distributions. It should be noted that the Monte-Carlo simulation tends to overestimate the efficiencies for the charged track reconstruction. The jets in the 2-jet sample are back-to-back in φ as expected from parton-parton scattering kinematics.

5.3 Jet shapes

In order to measure the inclusive jet cross-section, the data distributions have to be corrected for detector effects, which can be calculated from the Monte-Carlo simulations. Two studies have been performed to verify that the Monte-Carlo which is used for correction calculation adequately reproduces the main properties of jet events at the detector level.

The properties of the events containing jets were examined in terms of the transverse energy flow in the region around the jet direction and the charged particle content of the jets in the region where tracks are well reconstructed ($|\eta^{\text{jet}}| < 1.0$). The jet profiles, i.e.

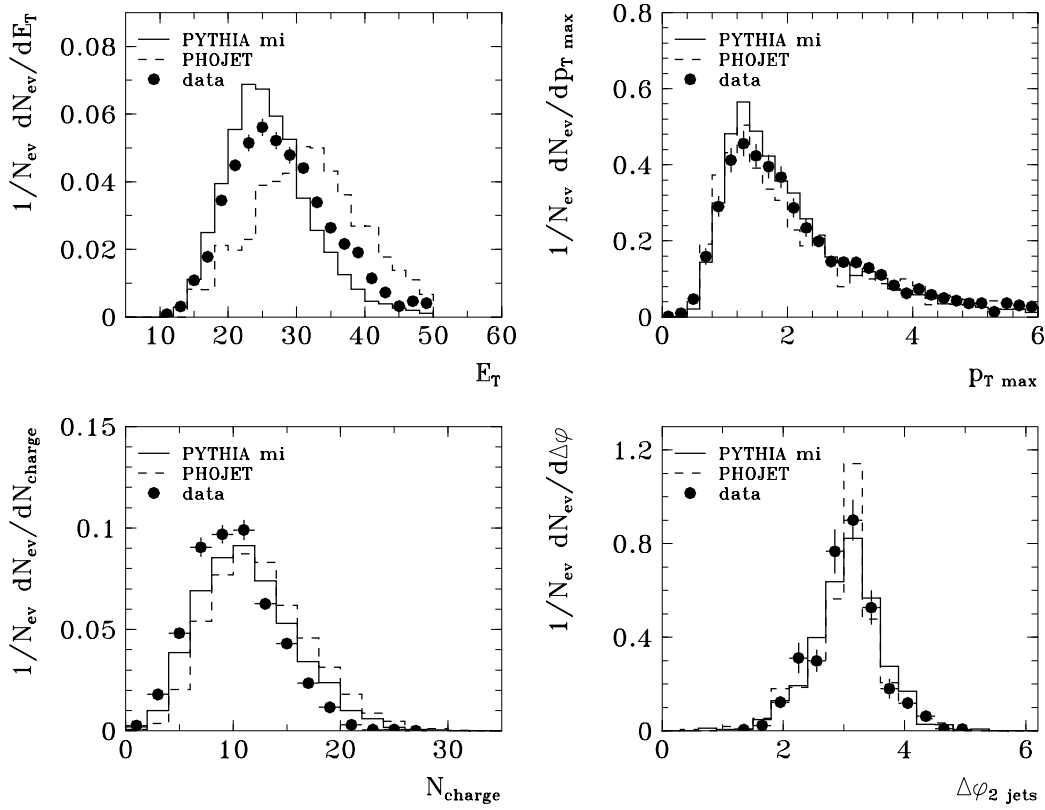


Figure 5.5: Distributions of the transverse energy E_T , the transverse momenta of the most energetic track $p_{T \max}$, multiplicity of the charged particles in the central tracker N_{charge} in the jet sample, and $\Delta\varphi$ between two jets in the 2-jet sample. Data are compared to the PYTHIA (with multiple interactions) and PHOJET Monte-Carlo predictions. All distributions are normalized to the number of events.

the average transverse energy flow around the jet axis, calculated from the calorimeter cells, are shown in Fig.5.6 and Fig.5.7 in two ranges of η^{jet} for jets with transverse energy $7 \leq E_T^{jet} \leq 9 \text{ GeV}$ as a function of $\Delta\varphi$ integrated over $|\Delta\eta| < 1.0$ (Fig.5.6, Fig.5.7a,b) and as a function of $\Delta\eta$ integrated over $|\Delta\varphi| < 1.0$ (Fig.5.6, Fig.5.7c,d). Here $\Delta\eta$ and $\Delta\varphi$ are the coordinates of the calorimeter cells relative to the jet axis.

Fig.5.8 and Fig.5.9 show the same distributions for jets $11 < E_T^{jet} < 13 \text{ GeV}$ and $15 < E_T^{jet} < 17 \text{ GeV}$ but only for forward jets $0.5 < \eta^{jet} < 2.0$.

On all plots one can see a strong peak around $\Delta\eta$ and $\Delta\varphi$ equal 0, which corresponds to the jet core. The increase of the energy flow at $\Delta\varphi \approx \pm\pi$ corresponds to the second jet, which also comes from hard parton-parton interaction. Only a fraction of the second jet energy is contained within the window $|\Delta\eta| < 1.0$. Therefore the energy flow around $\Delta\varphi = \pi$ does not balance the peak at $\Delta\varphi = 0$. Also, one can observe, that there is non-zero energy flow outside the jet cores both in azimuthal angle and pseudorapidity.

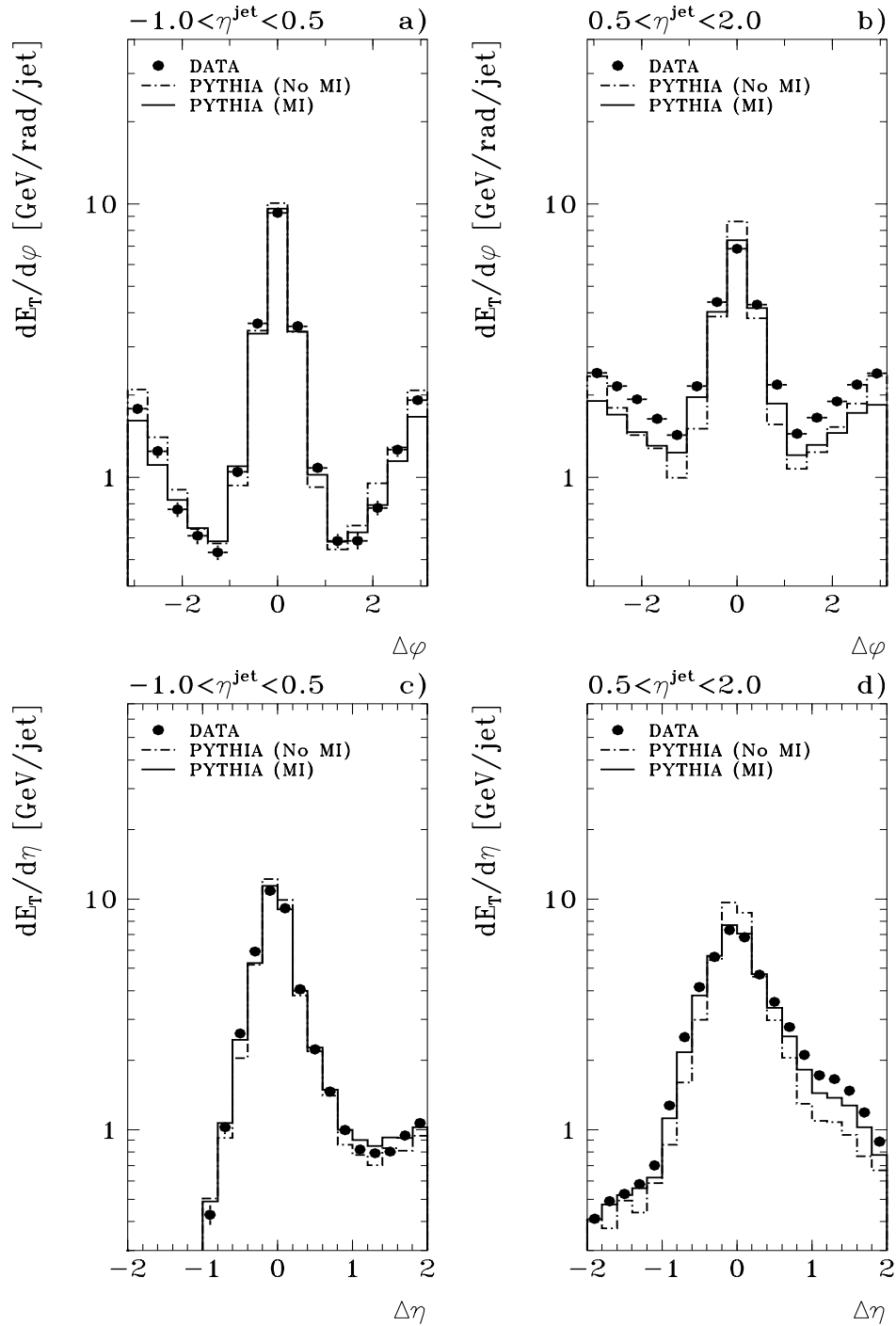


Figure 5.6: Transverse energy flow around the jet axis for jets with $7 < E_T^{jet} < 9$ GeV and $-1 < \eta^{jet} < 0.5$ (a,c), $0.5 < \eta^{jet} < 2.0$ (b,d) for data compared to PYTHIA Monte-Carlo predictions with (solid line) and without (dash-dotted line) multiple interactions.

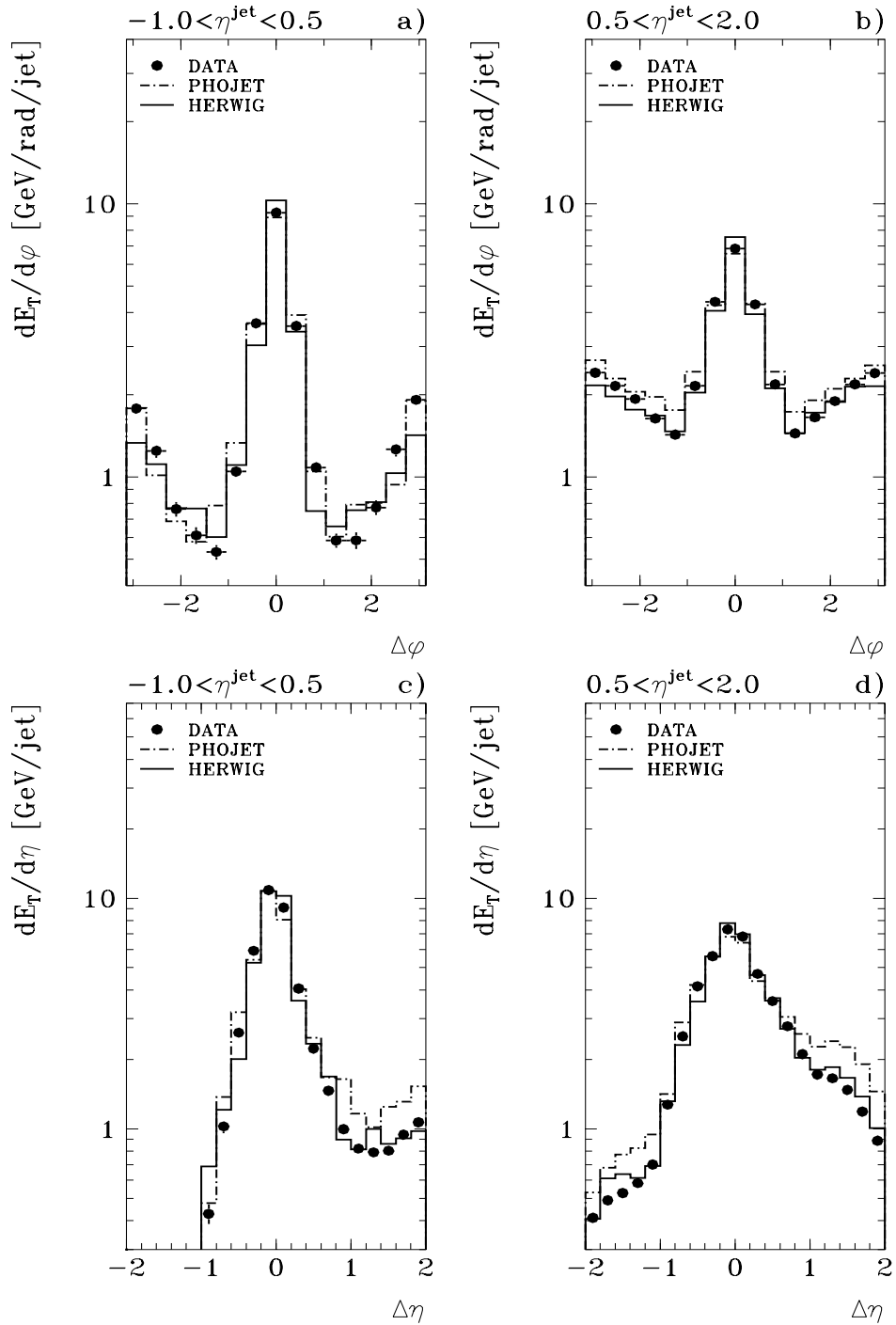


Figure 5.7: Transverse energy flow around the jet axis for jets with $7 < E_T^{jet} < 9 \text{ GeV}$ and $-1 < \eta^{jet} < 0.5$ (a,c), $0.5 < \eta^{jet} < 2.0$ (b,d) for data compared to HERWIG (solid line) and PHOJET (dash-dotted line) Monte-Carlo predictions.

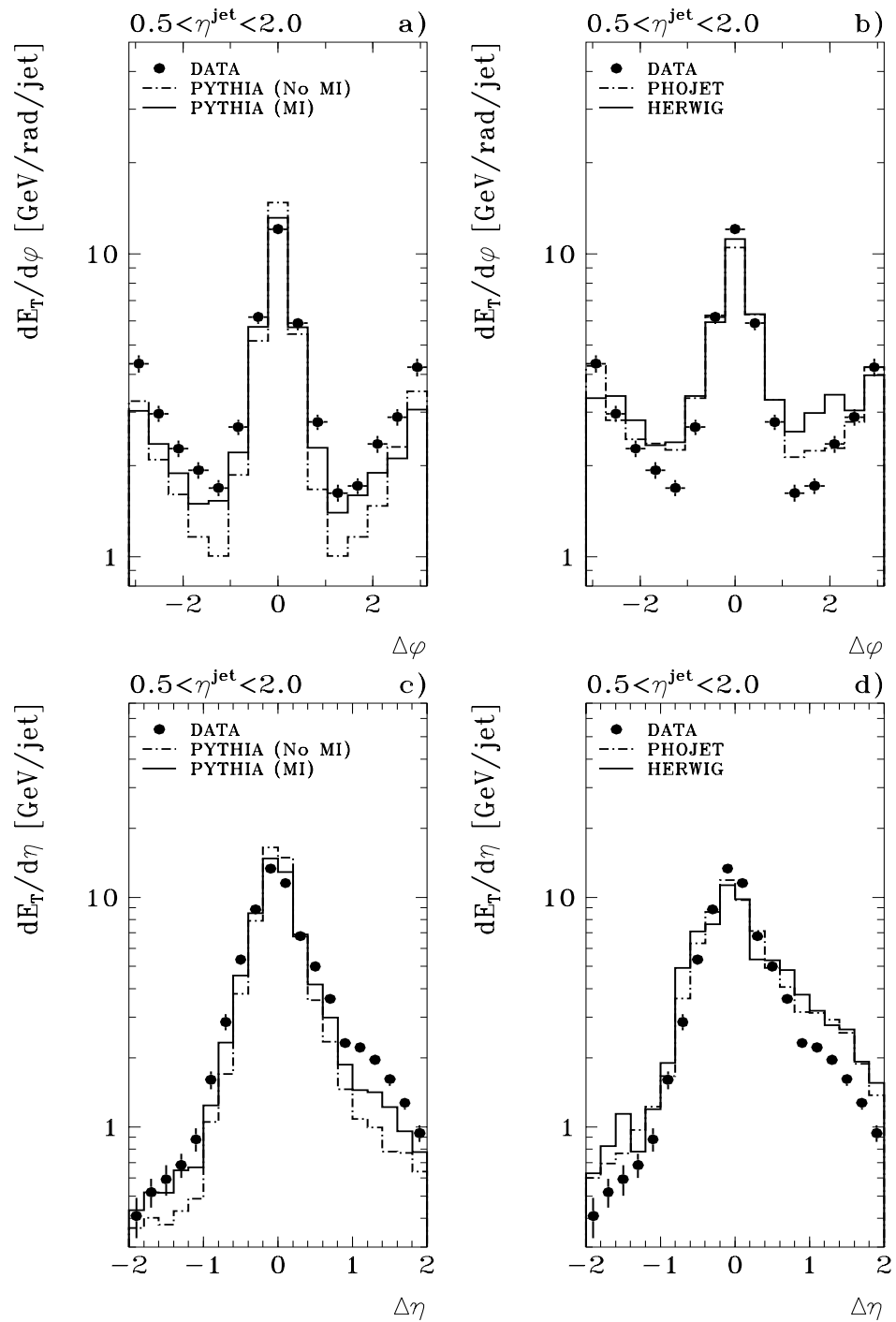


Figure 5.8: Transverse energy flow around the jet axis for jets with $11 < E_T^{\text{jet}} < 13 \text{ GeV}$ and $0.5 < \eta^{\text{jet}} < 2.0$. Left plots (a,c) compare data with PYTHIA Monte-Carlo predictions with (solid line) and without (dashed line) multiple interactions, and right plots (b,d) compare data with HERWIG (solid line) and PHOJET (dash-dotted line) Monte-Carlo predictions.

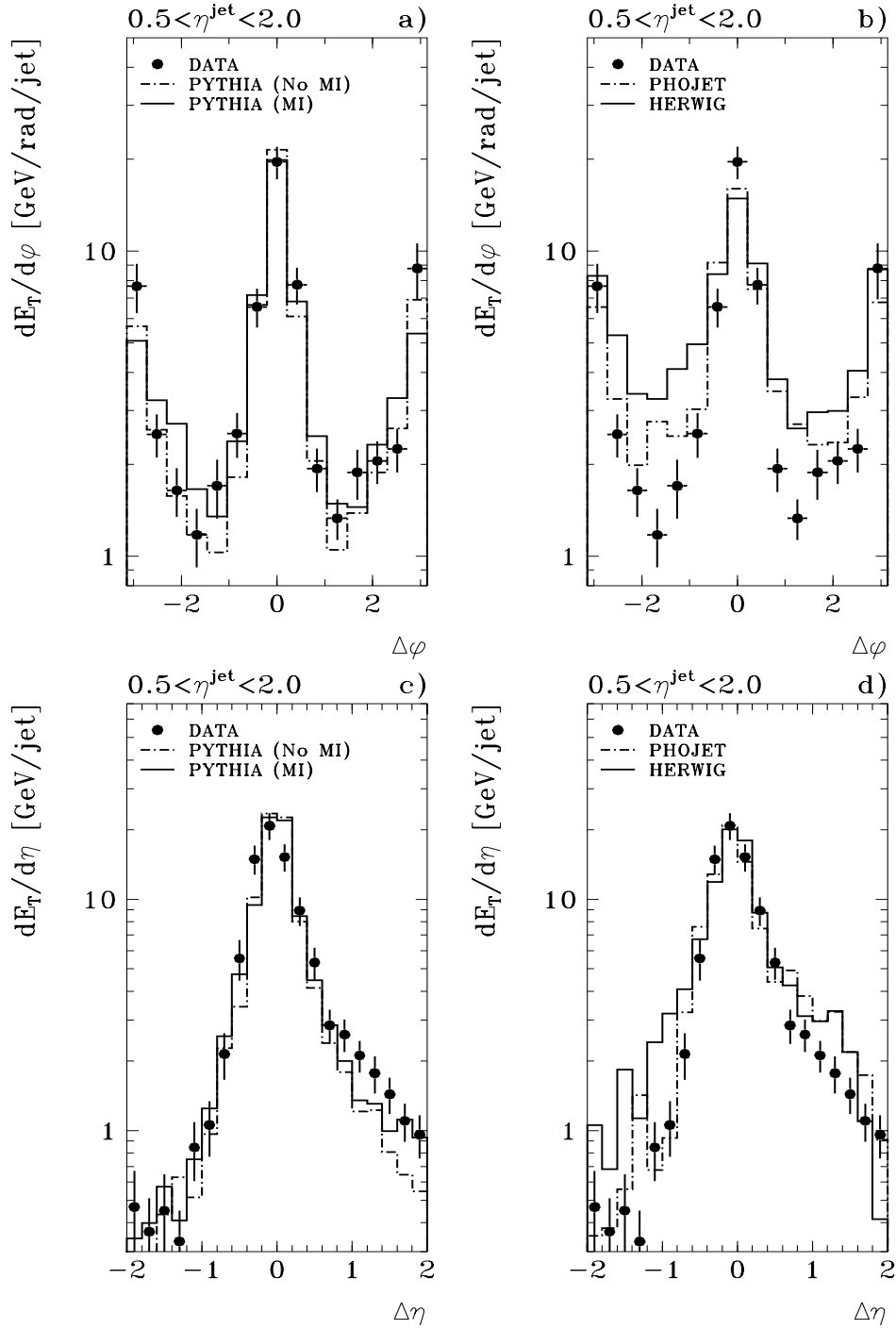


Figure 5.9: Transverse energy flow around the jet axis for jets with $15 < E_T^{jet} < 17 \text{ GeV}$ and $0.5 < \eta^{jet} < 2.0$. Left plots (a,c) compare data with PYTHIA Monte-Carlo predictions with (solid line) and without (dashed line) multiple interactions, and right plots (b,d) compare data with HERWIG (solid line) and PHOJET (dash-dotted line) Monte-Carlo predictions.

The average value of this “pedestal” is increasing with η^{jet} , as is seen well from the $\Delta\varphi$ distributions in Fig.5.6. The $\Delta\eta$ profiles are asymmetric, showing a higher energy level in the proton direction ($\Delta\eta \geq 0$) than in the photon direction ($\Delta\eta \leq 0$).

There are several effects, which can contribute to the pedestal energy

- hard parton–parton interaction,
- initial and final state (QCD) radiation, where gluons, emitted by partons before or after the hard interaction, can give additional energy flow between the jets,
- further partonic remnant–remnant interactions (multiple interactions)
- parton hadronisation.

These processes are described differently in various Monte-Carlo generators (see section 3.6). For this analysis we compare the jet profiles of the selected data sample with the PYTHIA, PHOJET and HERWIG Monte-Carlo predictions (see Fig.5.6-5.9).

All Monte-Carlo models, used here, describe the jet profiles well in the backward region $-1.0 < \eta^{jet} < 0.5$. However, they differ much in the forward detector region $0.5 < \eta^{jet} < 2.0$. The PYTHIA model without multiple interactions does not give a good description of jet profiles, in particular it predicts energy flow outside the jet core, both in azimuthal angle and pseudorapidity. The PYTHIA model with multiple interactions improves the description of jet profiles, but some discrepancy with the data remains. PHOJET predicts larger average values of E_T outside the jet cone. HERWIG gives a good description of data for $7 < E_T^{jet} < 9 \text{ GeV}$.¹ With increasing jet energy the pedestal predicted by HERWIG becomes larger than in the data, while the difference between PYTHIA (with multiple interactions) and data decreases and almost vanishes for $E_T^{jet} > 15 \text{ GeV}$.

Another variable, which characterizes jet events is the multiplicity of the charged tracks within the jet cone. For the following analysis the tracks were required to be in the range $|\eta^{track}| < 1.5$ and to have $p_T^{track} > 200 \text{ MeV}$, where p_T^{track} is the transverse momentum of the track with respect to the beam axis. Tracks were associated with the reconstructed jet if the variable $\Delta R = \sqrt{(\eta^{track} - \eta^{jet})^2 + (\varphi^{track} - \varphi^{jet})^2}$ was less than the cone radius used for the jet selection, i.e. $\Delta R \leq 1$.

The average distribution of charged tracks within the jet cone for jets $-1.0 < \eta^{jet} < 1.0$ and $7 < E_T^{jet} < 9 \text{ GeV}$ is shown in Fig.5.10. Again data are compared with PYTHIA, PHOJET and HERWIG predictions. All distributions are normalized to the total number of events.

The average charged multiplicity within the jet cone in the data is about 3.6. PYTHIA with multiple interactions, HERWIG and PHOJET give good descriptions of the data. At low E_T^{jet} the PYTHIA model without multiple interactions overestimates the average multiplicity by about 15%. For higher E_T^{jet} (say $E_T^{jet} > 11 \text{ GeV}$) the difference between the PYTHIA predictions with and without multiple interactions almost vanishes.

¹Here should be noted, that the parameter which defines the fraction of the soft underlying event in HERWIG (see section 3.6) was tuned in order to describe the distributions shown in Fig.5.7 and Fig.5.10.

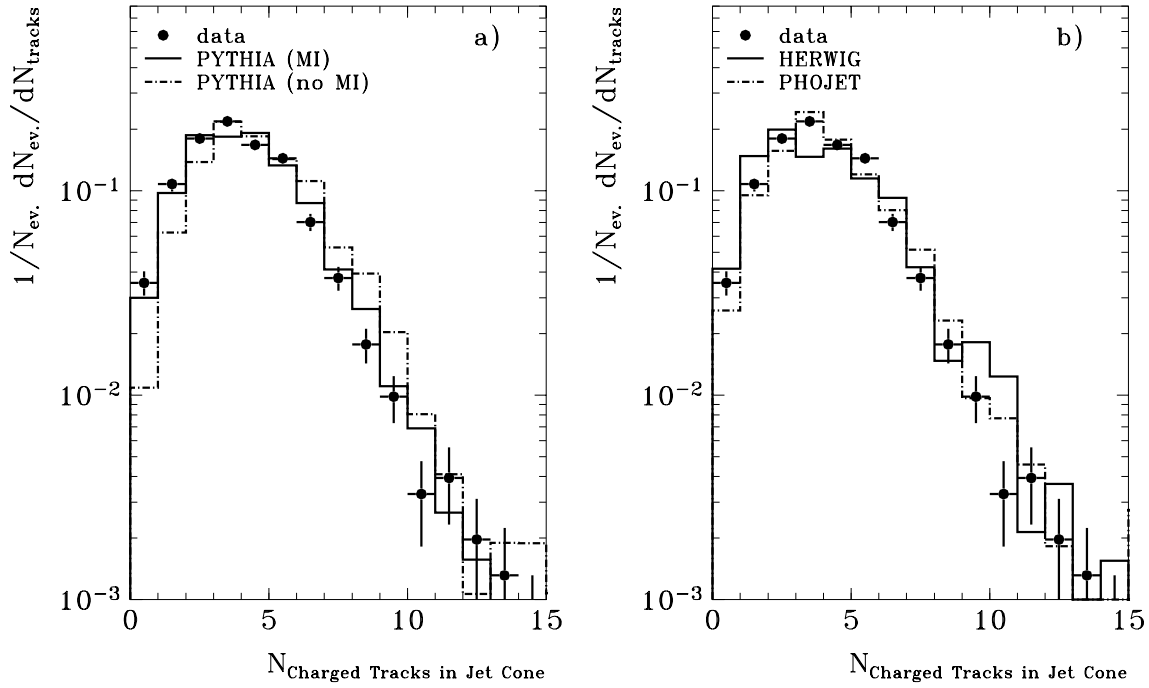


Figure 5.10: Multiplicity of charged tracks within the jet cone for jets with pseudorapidity $-1.0 < \eta^{jet} < 1.0$ and transverse energy $7 < E_T^{jet} < 9 \text{ GeV}$. Data are compared with Monte-Carlo predictions of PYTHIA (with and without multiple interactions) (a) and PHOJET and HERWIG (b).

5.4 The measurement of the inclusive jet cross-section

As was said above, in order to calculate the inclusive jet cross-section, the data distributions have to be corrected for detector effects, and the trigger efficiency and the acceptance has to be taken into account. The cross-section as a function of jet transverse energy and pseudorapidity was calculated according to the formulae:

$$\frac{d\sigma}{dE_T^{jet}} = \frac{dN}{dE_T^{jet}} \cdot \frac{1}{\int L dt \cdot \varepsilon_{trigger} \cdot Acc_{etag}} \cdot \epsilon(E_T^{jet}) \quad (5.4)$$

and

$$\frac{d\sigma}{d\eta^{jet}} = \frac{dN}{d\eta^{jet}} \cdot \frac{1}{\int L dt \cdot \varepsilon_{trigger} \cdot Acc_{etag}} \cdot \epsilon(\eta^{jet}), \quad (5.5)$$

where dN/dE_T^{jet} and $dN/d\eta^{jet}$ are the uncorrected distributions; Acc_{etag} is the geometrical acceptance of the electron detector; $\epsilon(E_T^{jet})$ and $\epsilon(\eta^{jet})$ are the correction functions (see

below); and $\int Ldt$ is the total integrated luminosity ($\approx 279.3 \text{ nb}^{-1}$). $\varepsilon_{trigger}$ is the trigger efficiency which can be represented as a product of the efficiencies of trigger elements included in this trigger:

$$\varepsilon_{trigger} = \varepsilon_{DC-R\varphi-a} \cdot \varepsilon_{t0} \cdot \varepsilon_{etag} \quad (5.6)$$

5.4.1 Trigger efficiency

The mean overall efficiency of the trigger conditions and the selection criteria, including the geometrical acceptance of the electron detector, is, as determined from the Monte-Carlo, $40 \pm 1\%$. The main source for inefficiency is the geometrical acceptance of the electron detector (Acc_{etag}). Acc_{etag} as function of $y \approx 1 - E'_e/E_e$ is shown in Fig.4.5. In average $\langle Acc_{etag} \rangle \approx 42 \pm 1\%$ and does not depend on E_T^{jet} and η^{jet} within statistical errors. The efficiency of $ETAG$ trigger element (ε_{etag}) is close to 100% (see Fig.4.2) and is taken into account in the luminosity calculation.

The efficiency of $ZVTX - t0$ trigger element is expected to be large for events with high track multiplicity. Indeed, from the Monte-Carlo simulation we obtained $\varepsilon_{t0} \approx 100\%$.

The efficiency of the $DC - r\varphi - a$ trigger ($\varepsilon_{DC-r\varphi-a}$) can be determined using a data sample, which was triggered by the minimum-bias trigger ($ETAG \times ZVTX - t0$).

This efficiency is shown in Fig.5.11 as function of E_T^{jet} and η^{jet} . It varies between 90 and 100% and is in agreement with the result of the Monte-Carlo simulation. This efficiency was taken into account for the inclusive jet cross-section, and $\sim 3\%$ uncertainty in the efficiency calculation was included in the systematic errors.

5.4.2 Corrections

In order to obtain an inclusive jet cross-section, the observed jet rates have to be corrected for detector effects. PYTHIA, HERWIG and PHOJET Monte-Carlo simulations have been used to determine the response of the detector to jets of hadrons. The correction functions $\epsilon(E_T^{jet})$ and $\epsilon(\eta^{jet})$ for each E_T^{jet} and η^{jet} bin are defined as the ratio between each bin content for the generated and for the reconstructed jets in the Monte Carlo events. The generator jets were determined from the original final state particles with lifetimes larger than 10^{-13} s using the same jet algorithm as for reconstructed events. The particles for the generator jet search have to be within the calorimeter region, where a fully contained measurement is possible ($5^\circ < \theta < 175^\circ$). The reconstructed jets were obtained after full detector simulation and reconstruction and event selection in the same way as for real data. Correction functions $\epsilon(E_T^{jet})$ and $\epsilon(\eta^{jet})$ computed from different Monte-Carlo simulations for $E_T^{jet} > 7 \text{ GeV}$ and $-1 < \eta^{jet} < 2$ are shown in Fig.5.12.

Since the PYTHIA Monte-Carlo with multiple interactions gives the best description of jet-profiles and charged track multiplicity within the jet cone (which is necessary for the bin-by-bin correction technique to be applicable), correction functions derived from this model were used in order to correct the data. The difference between correction

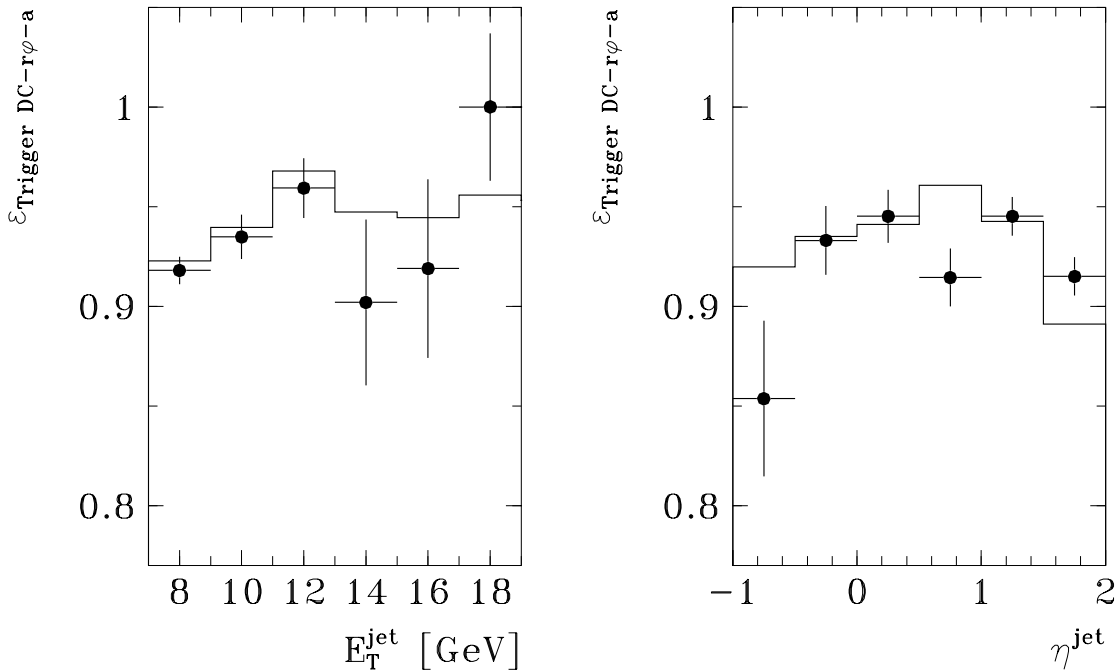


Figure 5.11: Efficiency of the trigger $DC - r\phi - a$ with respect to trigger $ZVTX - t0$ as a function of E_T^{jet} and η^{jet} for events with $E_T^{\text{jet}} > 7 \text{ GeV}$ and $-1 < \eta^{\text{jet}} < 2$. Points are data and the histogram is the result of the PYTHIA Monte-Carlo.

functions given by other Monte-Carlo models does not exceed 10%. The obtained correction function $\epsilon(E_T^{\text{jet}})$ varies from about 1.1 to 0.7 over the range $7 < E_T^{\text{jet}} < 30 \text{ GeV}$ and $\epsilon(\eta^{\text{jet}})$ from about 1.7 to 0.7 over the range $-1 < \eta^{\text{jet}} < 2$. No additional corrections were applied, either for the jet energy lost outside the jet core, or for the non-jet energy contribution inside the cone.

The jet resolution was determined by comparison of generator and reconstructed jets from the PYTHIA Monte-Carlo (see Fig.5.13). For each generator jet with $E_T^{\text{jet}_{gen}} > 7 \text{ GeV}$ and $-1 < \eta_{gen}^{\text{jet}} < 2$ the associated reconstructed jet with $E_T^{\text{jet}_{rec}} > 6 \text{ GeV}$ and $-1 < \eta_{rec}^{\text{jet}} < 2.5$ has been searched. The reconstructed jet was associated to a generator jet, if it lay in the same φ hemisphere, i.e. if $|\varphi_{rec}^{\text{jet}} - \varphi_{had}^{\text{jet}}| < 90^\circ$. The generator jets without corresponding reconstructed jets have not been considered for this comparison.

The resolution in η and φ was found to be about 0.1 for $E_T^{\text{jet}} \approx 7 \text{ GeV}$ in the whole η region and decreases to ~ 0.07 for higher energies $E_T^{\text{jet}} \gtrsim 17 \text{ GeV}$. The jet transverse energy resolution is $\approx 16\%$. On the other hand, the reconstructed jet energy is systematically smaller than the generated value by $\sim 10\%$ for $E_T^{\text{jet}} \approx 7 \text{ GeV}$ and $\sim 7\%$ for $E_T^{\text{jet}} \approx 17 \text{ GeV}$. The jet resolution given by PHOJET is worse (see Fig.5.14).

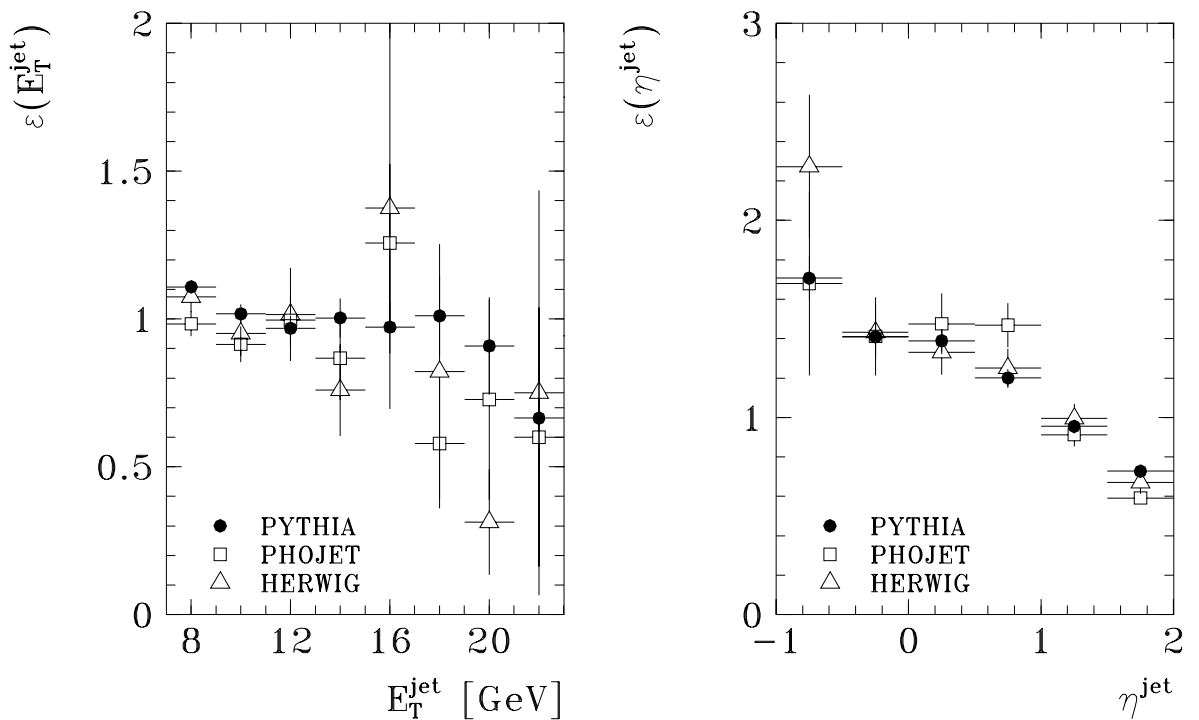


Figure 5.12: Correction functions $\epsilon(E_T^{\text{jet}})$ and $\epsilon(\eta^{\text{jet}})$ for PYTHIA with multiple interactions, PHOJET and HERWIG Monte-Carlo simulations.

The inclusive jet cross-section $d\sigma/dE_T^{\text{jet}}$ was calculated for two pseudorapidity regions: $-1 < \eta^{\text{jet}} < 2$ and $-1 < \eta^{\text{jet}} < 1$ requiring the minimum E_T of a jet to be more than 7 GeV. The cross-section $d\sigma/d\eta^{\text{jet}}$ was calculated for three different E_T thresholds of jets (7.0, 11.0 and 15.0 GeV). The corrected inclusive jet cross-sections as function of E_T^{jet} and η^{jet} are given in Tables 5.2-5.6.

5.4.3 Systematic errors

In the following the contributions to the systematic uncertainties are described.

The dominant source of systematic errors are the uncertainties in the absolute hadronic energy scale and resolution of the calorimeter. They have been verified from the balance of transverse momentum between hadronic jets and the scattered electron in DIS events.

The hadronic energy scale is known to a precision of 5%, allowing for an additional bin-by-bin contribution of $\pm 3\%$ caused by possible systematic differences between calorimeter sections. Taking into account the steep slope of the E_T^{jet} distribution as $\sim E_T^{-6.1}$ the quoted energy scale uncertainties correspond to about $\pm 25\%$ and $\pm 15\%$ uncertainties of

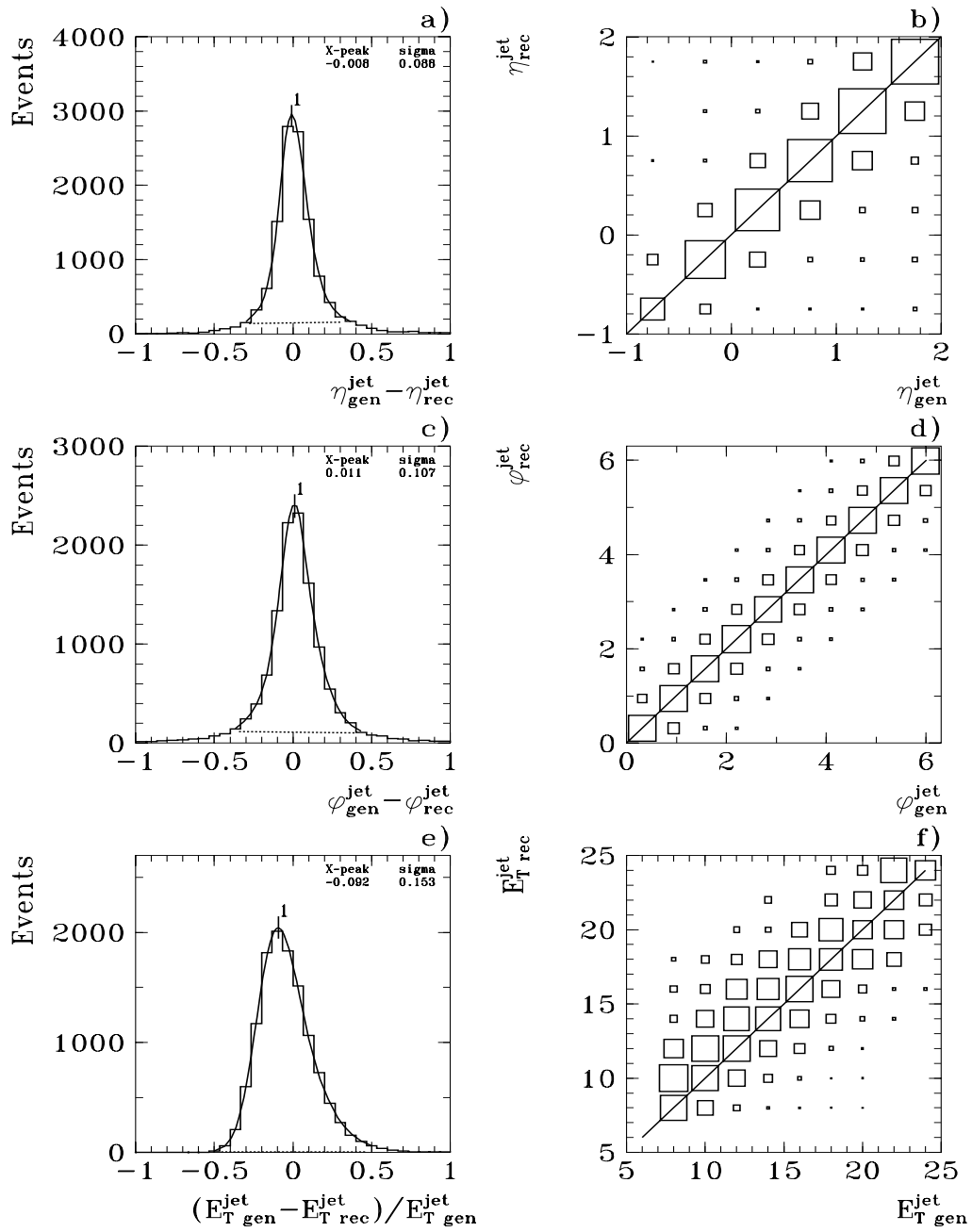


Figure 5.13: The difference between the η , φ and E_T of the reconstructed and generated jets obtained from PYTHIA Monte-Carlo for jets with $E_T^{\text{jet}}_{\text{gen}} > 7 \text{ GeV}$ and $-1 < \eta_{\text{gen}}^{\text{jet}} < 2$.

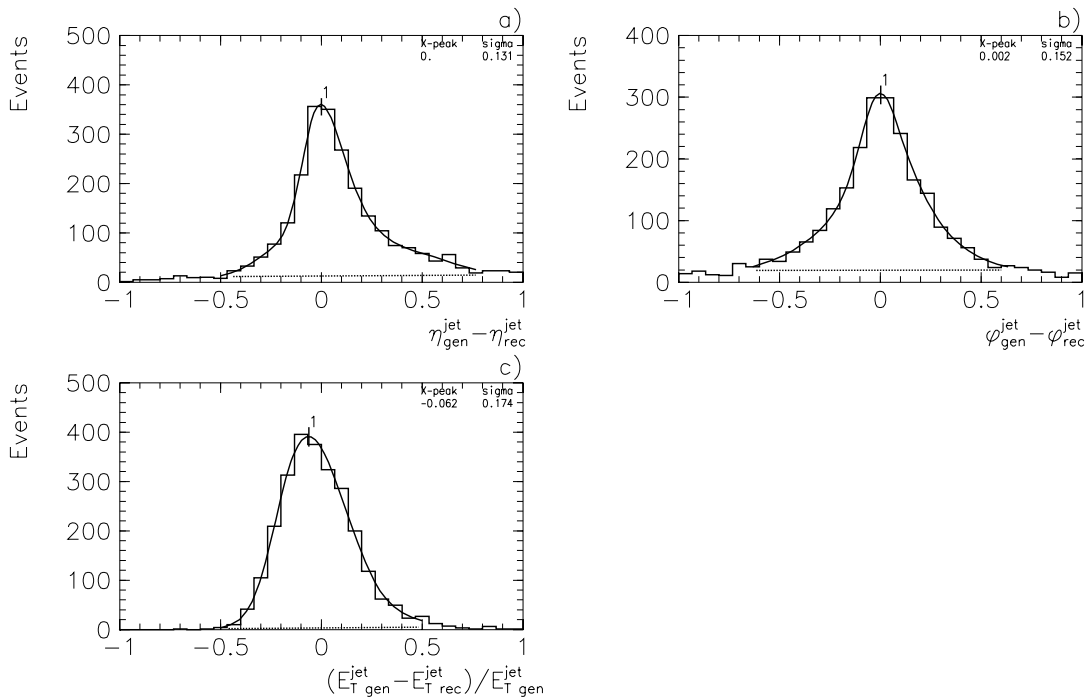


Figure 5.14: The difference between the η, φ and E_T of the reconstructed and generated jets obtained from PHOJET Monte-Carlo for jets with $E_T^{jet_{gen}} > 7 \text{ GeV}$ and $-1 < \eta_{gen}^{jet} < 2$.

the cross-section, respectively. These numbers have been derived by comparing the cross-sections after scaling the jet energies by $\pm 5\%$ and $\pm 3\%$, respectively.²

In order to compute the systematic errors due to uncertainty in the hadronic energy resolution ($50\%/\sqrt{E_T}$), which is known to a precision of 10%, E_T^{jet} was smeared by a Gaussian distribution with $\sigma = 30\% \cdot \sqrt{E_T}$ (because $[50\%/\sqrt{E_T}]^2 + [30\%/\sqrt{E_T}]^2 \approx [60\%/\sqrt{E_T}]^2$). The resulting contribution to the systematic errors in the cross-section is $\sim 10\%$.

The determination of the correction functions $\epsilon(E_T^{jet})$ and $\epsilon(\eta^{jet})$ gives rise to bin-by-bin uncertainties of $\pm 10\%$. The latter was determined by varying the shape of the Monte-Carlo spectrum within the range of errors of the measured spectrum. The differences between correction functions obtained from different Monte-Carlo simulations lie within this 10% level.

The uncertainty in the efficiency of the track-trigger is about 3%.

The uncertainty of the luminosity measurement, which includes also the uncertainty in the efficiency of the electron detector is $\pm 5\%$.

² If the cross-section $d\sigma/dE_T$ behaves like $f(E_T) \sim E_T^{-n}$ then for small variations of energy scale (δE_T) the upper limit of the variation of cross-section (δf) can be calculated by $\frac{\delta f}{f} \sim n \cdot \frac{\delta E_T}{E_T}$. For $n = 6.1$ and $\delta E_T/E_T = 5\%$ (3%) the expected systematic uncertainty of the cross-section will be 30% (18%).

The summary of the systematic errors is given in the Table 5.1.

The different contributions to the systematic errors added in quadrature result to the total bin-by-bin uncertainties of about $\sim 21\%$. An overall normalization uncertainty due to LAr energy scale and luminosity measurements amounts to $\pm 26\%$ and is shown in separate columns in Tables 5.2–5.6.

Table 5.1: Systematic errors to inclusive jet cross-section.

Source	Error
Luminosity (overall)	5%
LAr energy scale $\pm 5\%$ (overall)	25%
LAr energy scale $\pm 3\%$ (bin-by-bin)	15%
Trigger $DC - R\varphi - a$	3%
Uncertainty in jet energy resolution	10%
Uncertainty in correction functions	10%

5.4.4 Results and discussions

The measured differential ep inclusive jet cross-section $d\sigma/dE_T^{jet}$ is shown in Fig.5.15 for two ranges of η^{jet} : $-1 < \eta^{jet} < 2$ and $-1 < \eta^{jet} < 1$. The outer error bars in the data points receive contributions from the statistical errors and bin-by-bin systematic uncertainties, added in quadrature. The inner error bars represent only statistical errors. The overall systematic errors of the cross-section normalization is shown separately. In the figure the data distributions are compared to the absolute predictions of different Monte-Carlo generators: PYTHIA (with and without multiple interactions), HERWIG (without soft underlying event) and PHOJET. For all the models the GRV-LO photon structure function was used (except dotted line, which corresponds to LAC-1).

The cross-section $d\sigma/dE_T^{jet}$ shows a fast decrease with E_T^{jet} in both η ranges as $E_T^{-6.1 \pm 0.5}$, where the errors reflect the statistical and systematic uncertainties of the fit. The measured power -6.1 ± 0.5 is compatible with previous results on jet production in γp interactions [24, 29]. The result compares well with jet cross-sections measured by the UA1 experiment in $p\bar{p}$ collisions at the same CMS energy $\sqrt{s_{p\bar{p}}} = 200 \text{ GeV}$ [71] (Fig.5.16). This can be interpreted as a demonstration that γp and $p\bar{p}$ hard interactions are— in this kinematical range— predominantly based on the same type of parton scattering processes. Such a falling distributions is well described by the Monte-Carlo generators, however, the best description is given by models which include in addition the remnant interactions (for example, PHOJET and PYTHIA). The models which do not include remnant interactions underestimate the cross-sections at small E_T^{jet} values. We also note that HERWIG overestimates the cross-section at high E_T^{jet} .

The jet pseudorapidity cross-section $d\sigma/d\eta^{jet}$ is presented in Fig.5.17 for three different E_T^{jet} thresholds. Cross-section shows an increase with η^{jet} , although the rise at

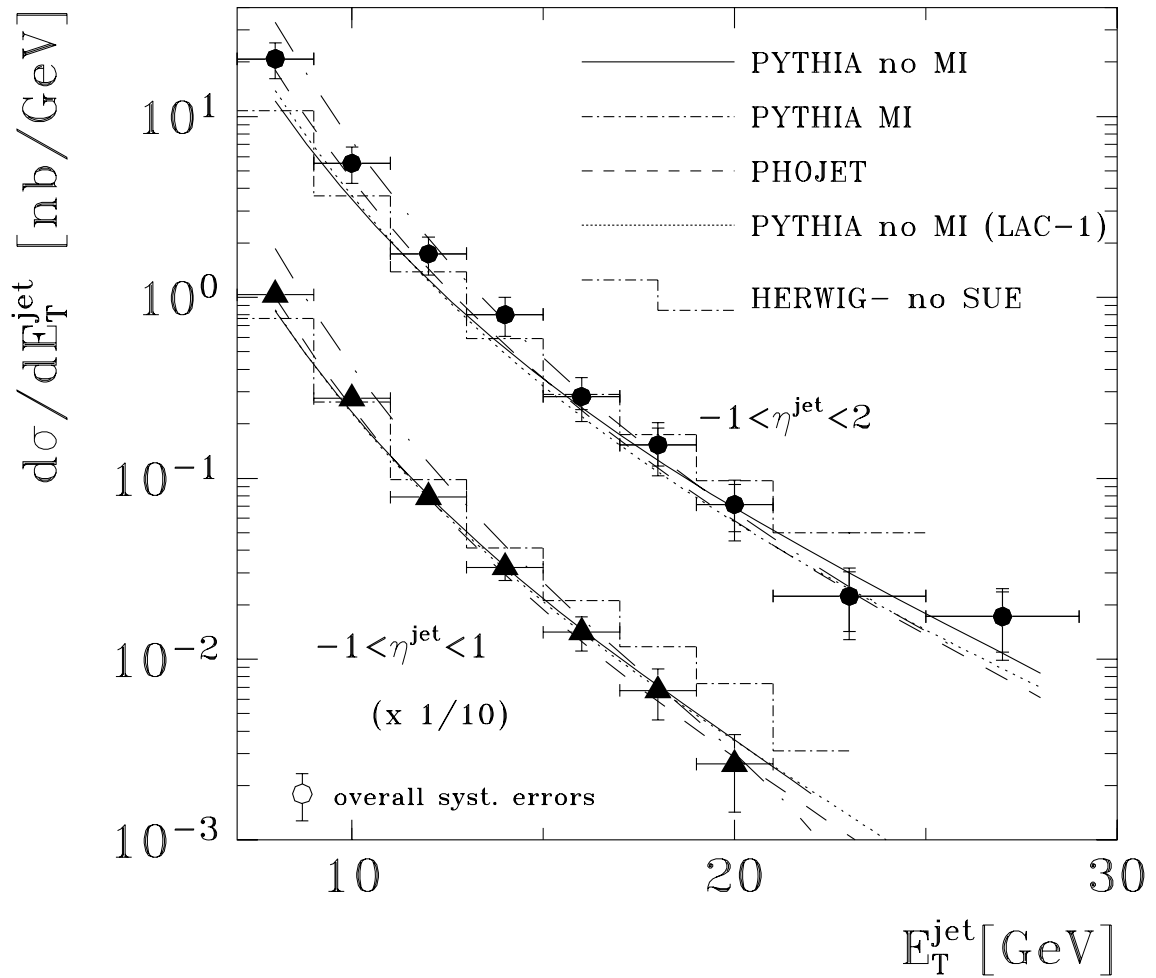


Figure 5.15: Inclusive differential jet cross-sections for jets with transverse energy above $E_T^{\text{jet}} > 7 \text{ GeV}$ summed in a cone of $R = 1$. The circles are H1 data integrated in the pseudorapidity range $-1.0 < \eta^{\text{jet}} < 2.0$, the triangles refer to the region $-1.0 < \eta^{\text{jet}} < 1.0$ (lowered by factor 10). The curves show the predictions of the Monte-Carlo generators.

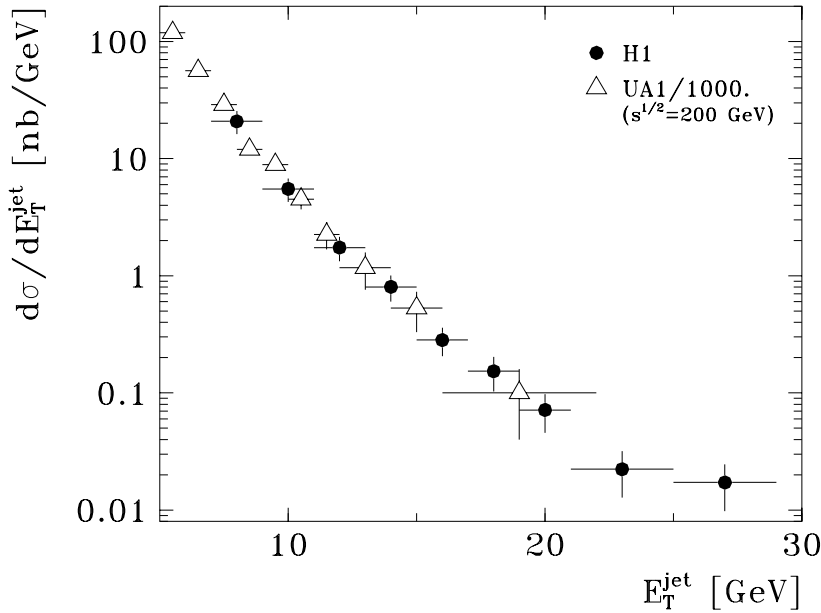


Figure 5.16: Inclusive differential jet cross-sections integrated in the pseudorapidity range $-1.0 < \eta^{jet} < 2.0$ (circles), and the results of UA1 experiment at $\sqrt{s_{p\bar{p}}} = 200 \text{ GeV}$ (triangles) [71], lowered by a factor 1000.

very forward η^{jet} observed for $E_T^{jet} > 7.0 \text{ GeV}$ is not present at higher E_T thresholds $E_T^{jet} > 11.0, 15.0 \text{ GeV}$. The measured cross-section is compared to the different Monte-Carlo models using the GRV-LO photon structure function. Fig.5.17a shows a comparison of the data with the Monte-Carlo models which consider only the leading order parton-parton scattering and parton showers, but no remnant interactions (PYTHIA and HERWIG), while Fig.5.17b compares data with the Monte-Carlo models which include additional remnant interaction models (PYTHIA, HERWIG and PHOJET). The calculations which include additional interactions (or soft underlying events)– PHOJET, PYTHIA and HERWIG– provide a fair description of the shape of the measured cross-section. The models without remnant interactions show clear deficiencies in describing the cross-section at large pseudorapidities and small transverse energies of the jets. We remember, that these models failed to describe the jet profiles as well, namely, there was a significant excess of transverse energy density in the data with respect to the no-remnant interaction Monte-Carlo expectations for jets in the forward region (see section 5.3). The large pseudorapidities ($\eta^{jet} > 1$), where the discrepancy between the data and Monte-Carlo is largest, correspond to the region of small momentum fraction of the parton from the photon $x_\gamma < 0.2$ (this is demonstrated in the Fig.5.18 where the average x_γ is shown as function of η_{jet} for the PYTHIA Monte-Carlo). For these events the spectator partons carry much energy and, therefore, can undergo additional interactions. We have already

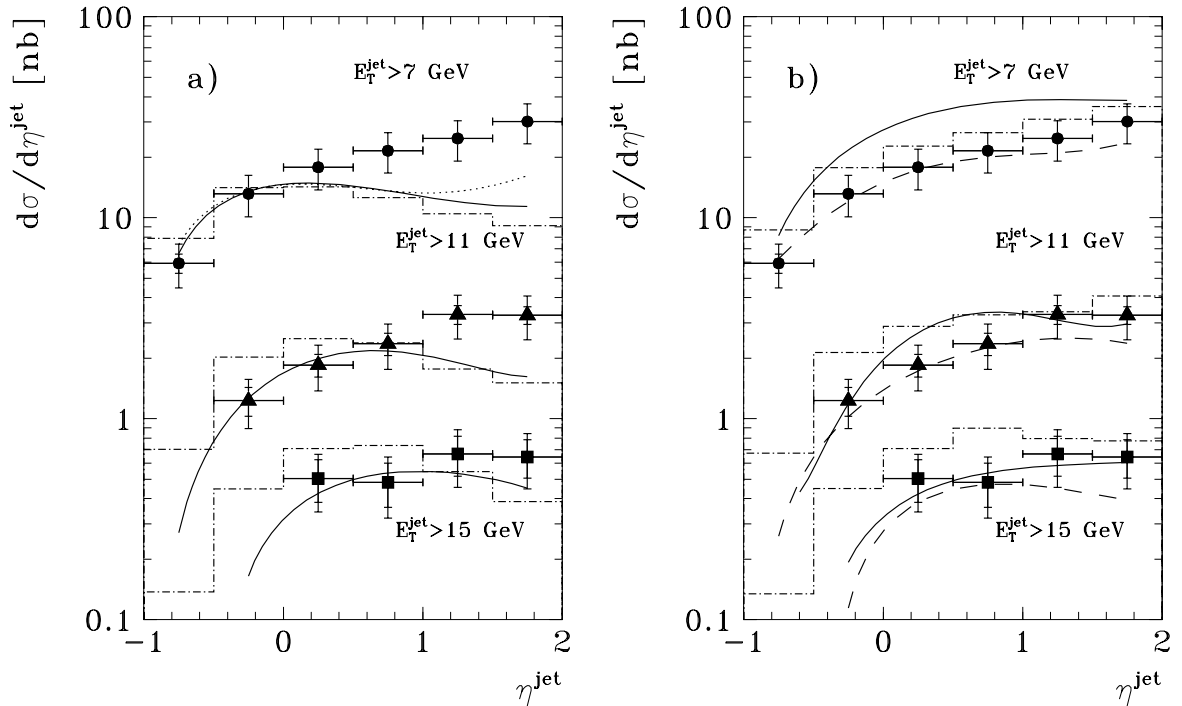


Figure 5.17: Inclusive differential jet cross-sections $d\sigma/d\eta^{jet}$ for different thresholds in the jet transverse energy compared to Monte-Carlo predictions.

a) Data compared to the Monte-Carlo models **without** remnant-remnant interactions. Solid line- PYTHIA and the dash-dotted histogram- HERWIG. Both use GRV-LO photon structure function. Dotted line is PYTHIA using LAC-1 photon structure function.

b) Data compared to the Monte-Carlo models **with** remnant-remnant interactions. Solid line- PYTHIA, the dash-dotted histogram- HERWIG, dashed line- PHOJET. All Monte-Carlo models use GRV-LO photon structure function.

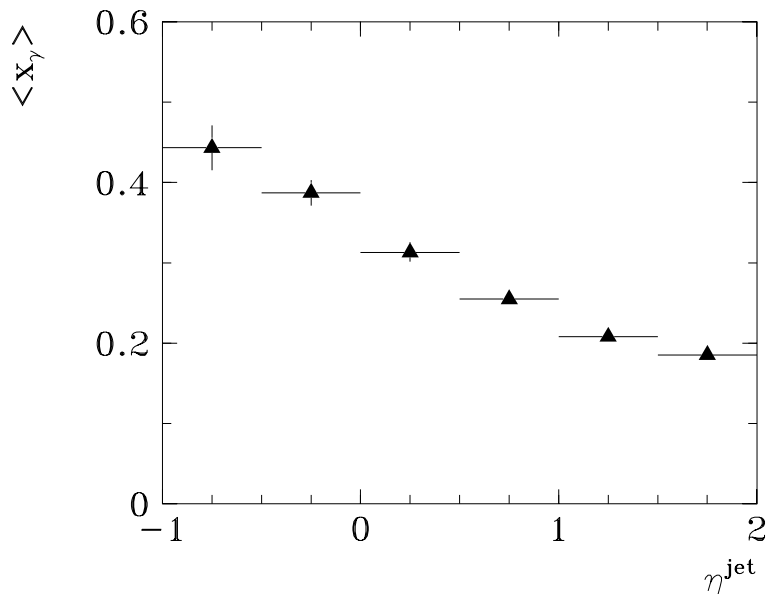


Figure 5.18: Average fraction of parton momentum $\langle x_\gamma \rangle$ vs the pseudorapidity of the jets with $E_T^{\text{jet}} > 7 \text{ GeV}$ from PYTHIA Monte-Carlo.

observed, that the description of jet profiles in photoproduction events was improved when interactions of the spectator partons have been added to the calculations (section 5.3). In $\bar{p}p$ scattering the measured underlying event energy was also not well reproduced by QCD calculations using only the matrix elements and parton distributions [83]. However, the data have been described by adding interactions of the beam remnants to the calculations [72].

The sensitivity of the jet inclusive cross-section to the gluon content of the photon and to the direct photon component was studied with the PYTHIA Monte-Carlo. The cross-section is split into the direct part, the part originating from the quark distribution and from the gluon distribution of the photon using the GRV-LO structure function. The results are shown in Fig.5.19. It demonstrates that the resolved photon processes dominate in the whole kinematical range studied, but the direct contribution increases with increasing E_T^{jet} . From this figure we also conclude that gluons in the photon make an essential contribution to the measured cross-section at low E_T^{jet} and high η^{jet} (Fig.5.19b).

Since the measurements are sensitive to the gluon content of the photon, they can provide a direct comparison between the different parametrizations, which differ mainly in the description of the gluon part. In order to study this, the cross-sections were calculated with the same Monte-Carlo generators but using LAC-1 structure function, which has a larger gluon content at small x_γ compared to GRV-LO parametrization (see Fig.3.7). From previous studies both structure functions (GRV-LO and LAC-1) were found to give

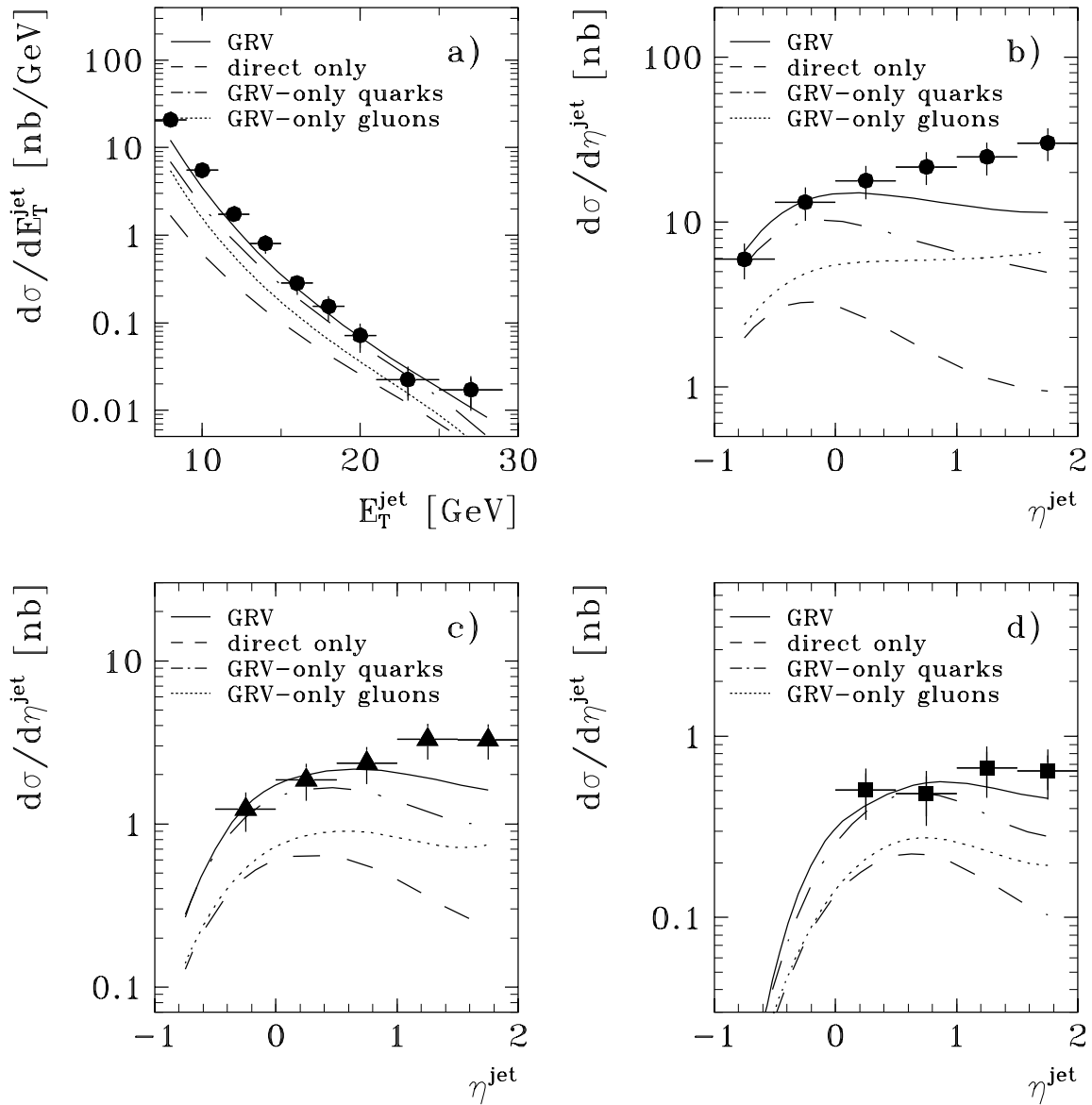


Figure 5.19: a) Inclusive differential jet cross-sections $d\sigma/dE_T^{jet}$ for jets $-1 \leq \eta^{jet} \leq 2$.
b) Inclusive differential jet cross-sections $d\sigma/d\eta^{jet}$ for jets with $E_T^{jet} > 7$ GeV.
c) Inclusive differential jet cross-sections $d\sigma/d\eta^{jet}$ for jets with $E_T^{jet} > 11$ GeV.
d) Inclusive differential jet cross-sections $d\sigma/d\eta^{jet}$ for jets with $E_T^{jet} > 15$ GeV.

The curves show the calculation of the PYTHIA generator with the separate contributions of gluons and quarks in the photon (using the GRV-LO photon structure function), and the direct photon contribution.

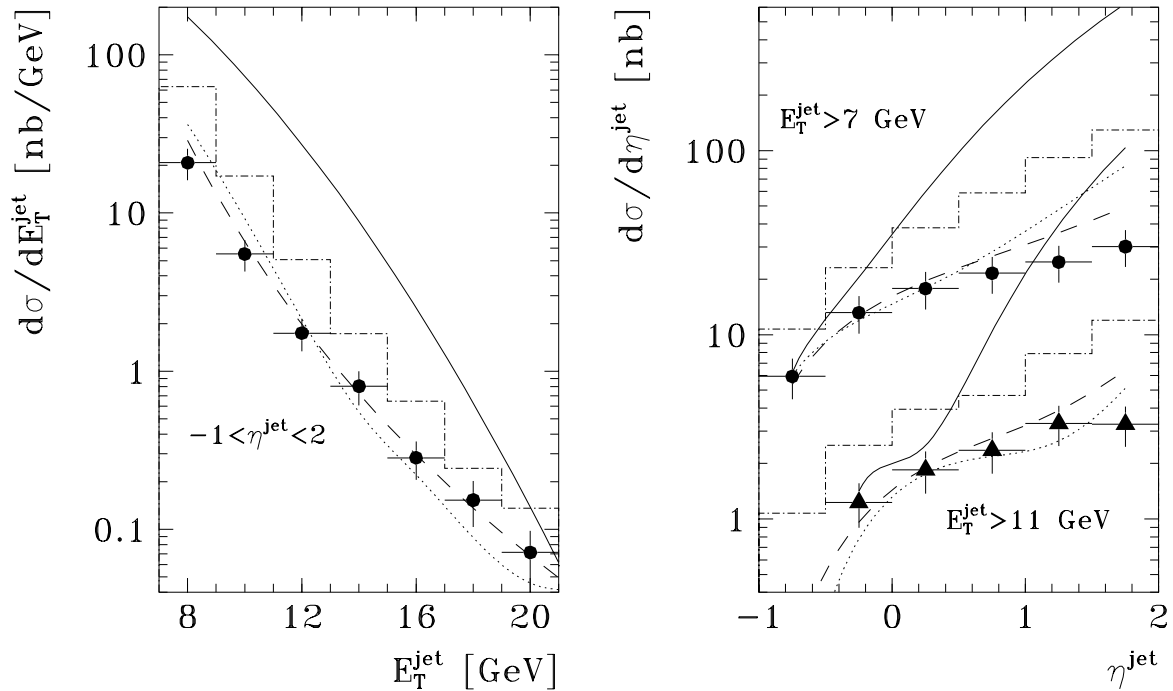


Figure 5.20: Measured inclusive differential jet cross-section $d\sigma/dE_T^{jet}$ and $d\sigma/d\eta^{jet}$ compared with Monte-Carlo models **with** remnant-remnant interactions and using the LAC-1 photon structure function. Solid line-PYTHIA, dashed line-PHOJET, histogram-HERWIG. Dotted line corresponds to PYTHIA after changing the transverse momentum cut-off of multiple interactions $\hat{p}_{T MI}$ from 1.2 GeV to 2 GeV .

satisfactory description of data³. First, the predictions of GRV-LO and LAC-1 structure functions are compared using no-remnant interaction models. In Fig.5.15 and Fig.5.17a the dotted lines indicate the results of PYTHIA generator for LAC-1. The E_T^{jet} cross-section for LAC-1 and GRV-LO (solid line) structure functions are quite similar (Fig.5.15).

In contrast to the E_T^{jet} cross-section the predictions for LAC-1 and GRV-LO structure functions differ in the jet pseudorapidity cross-section at low E_T^{jet} (Fig.5.17). It is the reflection of larger gluon density at small fractional momenta x_γ in LAC-1. The prediction based on the LAC-1 increases for $\eta^{jet} > 1$, whereas the predictions based on the GRV-LO shows a slow decrease in this region. Although the Monte-Carlo calculation using the LAC-1 gives a reasonable description of the rise of η^{jet} cross-section in the forward region at low E_T^{jet} , it cannot be concluded that this rise is due to the abundance of low x_γ gluons

³The LAC-3 parametrization with an extremely large gluon content at high x was ruled out by the previous measurements [24]. The results of calculations using LAC-2 parametrization are very similar with those using LAC-1.

in the photon, because, as was shown before, the underlying event energy, which is not included in this calculation, has large influence on the measured jet cross-section in this region.

In the calculations which include the remnant interactions the difference between the GRV-LO and LAC-1 structure functions becomes more significant (compare Fig.5.17b and Fig.5.20). At large η^{jet} prediction of the PYTHIA Monte-Carlo using the LAC-1 photon structure function is about order of magnitude higher than the data or the same Monte-Carlo but using GRV-LO photon structure function. However, the effect of introducing multiple interactions depends strongly on the parton density of the photon, and therefore, the model parameters which describe the multiple interactions cannot be tuned independently of the photon structure functions. For instance, after changing the parameter which defines the transverse momentum cut-off of multiple interactions $\hat{p}_{T MI}$ in the PYTHIA Monte-Carlo (see section 3.6.1) from 1.2 GeV to 2.0 GeV, the jet cross-section decreases by about a factor 5 (compare solid and dotted lines in the Fig.5.20). Furthermore, the results of different Monte-Carlo models differ in absolute numbers in the low E_T^{jet} region despite the use of the same QCD matrix elements and structure functions. The calculations include different modeling of the remnant interactions and the transition from the hard to the soft scattering region. There is a large amount of freedom in the models, and a firm conclusion can be drawn only after better understanding of these effects.

The measured cross-sections have also been compared to the next-to-leading order (NLO) QCD calculations, which have become available recently, and where the theoretical framework is well understood [84]-[87]. NLO calculations have significant advantages with respect to the LO. First, in the LO calculations the jets are identical with two partons, emerging from the hard interaction, and the cross-sections do not depend on the cone size (the dependence appears in the Monte-Carlo calculations after including the parton showers and hadronisation effects). In the NLO there is explicit dependence on the jet definition: one must decide when two partons count as two jets and when they count as one. It was demonstrated that the NLO cross-section increases with the increasing of the cone size, and is about 20% larger than the LO cross-section for a cone size of $R = 1$ [84]. Second, the uncertainty of the theoretical cross-section due to the choice of the renormalization and factorization scale is reduced, so the sensitivity of the results to the choice of the photon distribution is significant compared to the choice of scales. Another feature of NLO calculations is that the separation between the direct and resolved parts becomes ambiguous because there are diagrams which contribute to both processes, and only the sum of both contributions is physically meaningful.

Fig.5.21 shows the comparison of the measured cross-sections with NLO calculations of P. Aurenche et al. [88] (dashed lines) and with results of JETSAM program, which is based on the calculations of G. Kramer et al. [89] (solid and dash-dotted lines). The solid lines correspond to the GRV-HO photon structure function, and the dash-dotted lines to the parametrization of P. Aurenche et al., similar to that used in ref.[88]. Both calculations approximately agree in predictions when they use the same structure function. This result demonstrates the sensitivity of NLO calculations to the variation of the parton distribution functions in the photon. The calculations are in good agreement with the data at the high E_T^{jet} values, but clearly fail to describe the pseudorapidity distribution

for low E_T^{jet} . However, we must keep in mind, that the experimental cross-sections are for jets made of hadrons, whereas the theoretical cross-sections are for the jets consisting of partons. Theoretical calculations do not include effects of parton fragmentation and multiple interactions, which may play an important role at low E_T^{jet} values and lead to an increase of cross-sections.

The effect of hadronisation on the cross-section was studied using the PYTHIA Monte-Carlo by comparing the cross-sections calculated from the final state hadrons and leading order partons. This effect is about 30% at $E_T^{jet} > 7 \text{ GeV}$ and decreases to about 10% at $E_T^{jet} > 15 \text{ GeV}$.

The influence of the underlying event energy (multiple interactions) on the jet cross-section can be estimated using the measured energy density outside the jets in the central γp collision region ($-1 < \eta^* < 1$ in γp CMS or approximately $1 < \eta < 3$ in the laboratory system) [73]. With the assumption that the calculations of the PYTHIA and HERWIG generators represent a good approximation to the energy density outside the jets arising from the hard parton scattering process, the average energy added by multiple interactions into the jet cone energy is calculated as the energy difference between the data and the calculation without multiple interaction (see for details ref. [73]). In the jet pseudorapidity range $1 < \eta^{jet} < 2$ this energy was found to be about $0.8 \pm 0.45 \text{ GeV}$. In order to correct the measured cross-section for the underlying event energy this energy has to be subtracted from the energy of the jet. This correction lower the cross-section for jets $E_T^{jet} > 7 \text{ GeV}$ by about 40%, $E_T^{jet} > 11 \text{ GeV}$ by 30%, and $E_T^{jet} > 15 \text{ GeV}$ by 15%. The measured cross-sections after a correction for the underlying event energy are given in the Table 5.7 and shown in the Fig.5.21 by the open symbols.

Thus, if the contributions from hadronisation effects and soft underlying event are taken into account, the agreement between the theoretical (NLO) and experimental results with respect to shape and absolute normalization is quite reasonable.

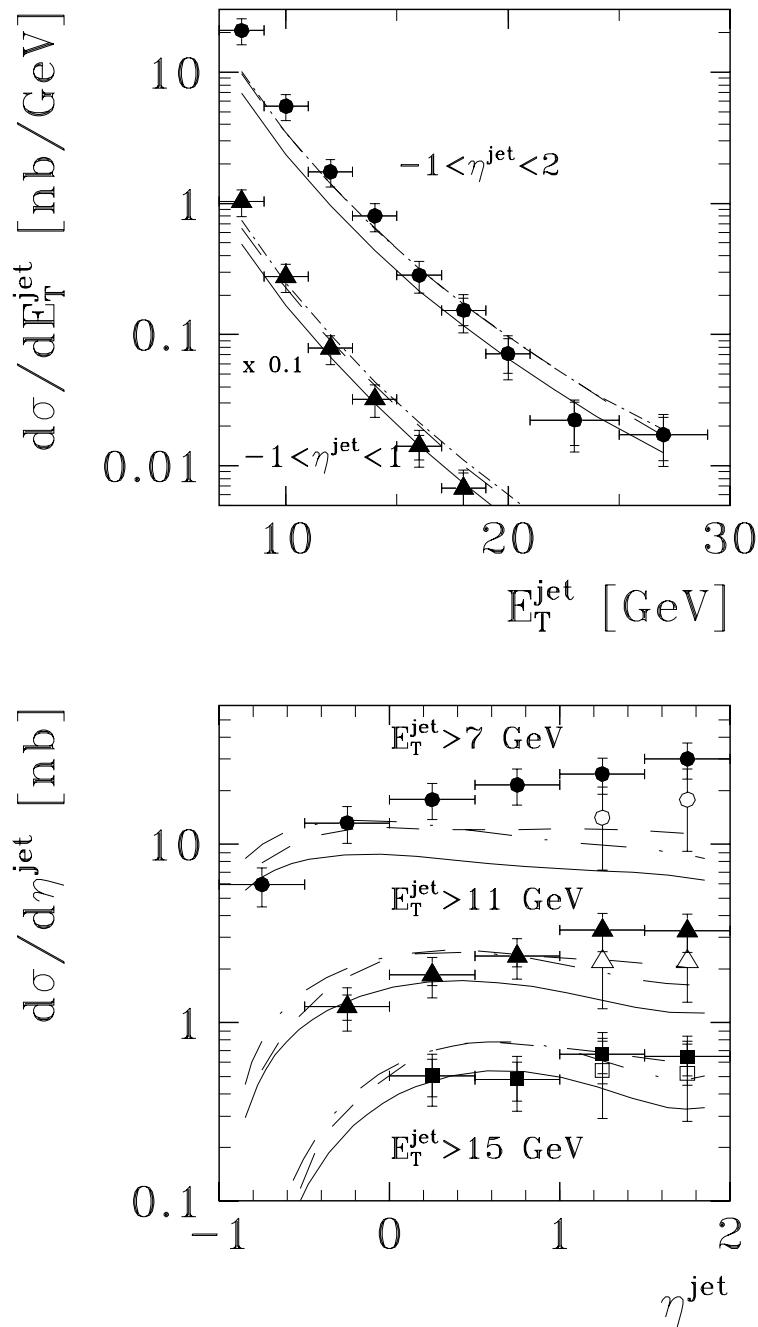


Figure 5.21: Inclusive differential jet cross-sections $d\sigma/dE_T^{\text{jet}}$ and $d\sigma/d\eta^{\text{jet}}$ compared with the next-to-leading order calculations. Solid line—calculations done with JETSAM program [89], based on the results of M. Klasen, G. Kramer, and S.G. Salesch, using GRV-HO photon structure function, and dash-dotted line—using AFG (P. Aurenche et al.) photon structure function. Dashed line—calculations of P. Aurenche, J.-Ph. Guillet and M. Fontannaz [88]. Open symbols are the data points after correction for underlying event energy.

5.5 Conclusions

Measurements of the differential cross-sections for inclusive jet photoproduction in ep collisions at $\sqrt{s_{ep}} = 296 \text{ GeV}$ in the kinematical range $Q^2 < 0.01 \text{ GeV}^{-2}$ and $0.25 < y < 0.7$ using the data collected by H1 in 1993 are presented. The jet cross-sections, $d\sigma/dE_T^{jet}$ and $d\sigma/d\eta^{jet}$, refer to hadron jets with a cone radius of one unit in $\eta - \varphi$ space. The cross-section $d\sigma/dE_T^{jet}$ has been measured in the E_T^{jet} range between 7 and 30 GeV , integrated over two η^{jet} ranges ($-1 < \eta^{jet} < 2$ and $-1 < \eta^{jet} < 1$). The cross-section $d\sigma/d\eta^{jet}$ has been measured in the η^{jet} range between -1 and 2 integrated over E_T^{jet} from various thresholds ($E_T^{jet} > 7, 11, 15 \text{ GeV}$). Leading logarithm parton shower Monte-Carlo calculations using the predictions of currently available parametrizations of the photon parton distributions are compared to the measured jet cross-sections. It is shown that the main contribution to the measured cross-section in the kinematical range studied is due to the resolved component of the photon structure function with a substantial contribution from its gluonic component. The measured cross-sections are well described by LO QCD calculations which include in addition to the matrix elements of the parton scattering processes parton showers and interactions of beam spectators. However, these effects are not well understood yet, and the predictions of various Monte-Carlo generators differ significantly. The relevant conclusions on the hard parton scattering process from the inclusive jet cross-section measurements demand a detailed understanding of underlying event energy.

The measured inclusive jet cross-sections are compared with the available next-to-leading order calculations. Calculations describe the data well at high E_T^{jet} values. The discrepancies between the measured and theoretical cross-sections at low E_T^{jet} can be explained by non-perturbative effects, namely the remnant-remnant interactions and fragmentation, which are not included in the NLO calculations.

Table 5.2: Measured differential ep cross-section $d\sigma/dE_T^{jet}$ for inclusive jet production integrated over $-1.0 \leq \eta^{jet} \leq 2.0$ in the kinematical range defined by $Q^2 < 0.01 \text{ GeV}^2$ and $0.25 < y < 0.7$.

$E_T^{jet} [\text{GeV}]$	$d\sigma/dE_T^{jet} [\text{nb/GeV}]$	<i>stat.error</i>	<i>syst.error</i>	<i>syst.overall error</i>
7.0– 9.0	20.8	0.56	4.4	5.4
9.0– 11.0	5.5	0.26	1.2	1.4
11.0– 13.0	1.74	0.12	0.37	0.45
13.0– 15.0	0.803	0.079	0.17	0.21
15.0– 17.0	0.283	0.044	0.059	0.074
17.0– 19.0	0.153	0.036	0.032	0.040
19.0– 21.0	0.0715	0.021	0.015	0.019
21.0– 25.0	0.0223	0.0081	0.0047	0.0058
25.0– 29.0	0.0172	0.0063	0.0036	0.0045

Table 5.3: Measured differential ep cross-section $d\sigma/dE_T^{jet}$ for inclusive jet production integrated over $-1.0 \leq \eta^{jet} \leq 1.0$ in the kinematical range defined by $Q^2 < 0.01 \text{ GeV}^2$ and $0.25 < y < 0.7$.

$E_T^{jet} [\text{GeV}]$	$d\sigma/dE_T^{jet} [\text{nb/GeV}]$	<i>stat.error</i>	<i>syst.error</i>	<i>syst.overall error</i>
7.0– 9.0	10.3	0.39	2.2	2.7
9.0– 11.0	2.76	0.19	0.58	0.72
11.0– 13.0	0.787	0.078	0.17	0.20
13.0– 15.0	0.322	0.049	0.067	0.084
15.0– 17.0	0.141	0.030	0.030	0.037
17.0– 19.0	0.0672	0.021	0.014	0.017
19.0– 21.0	0.0263	0.012	0.0055	0.0068

Table 5.4: Measured differential ep cross-section $d\sigma/d\eta^{jet}$ for inclusive jet production integrated over $E_T^{jet} > 7.0 \text{ GeV}$ in the kinematical range defined by $Q^2 < 0.01 \text{ GeV}^2$ and $0.25 < y < 0.7$.

η^{jet}	$d\sigma/d\eta^{jet} [\text{nb}]$	<i>stat.error</i>	<i>syst.error</i>	<i>syst.overall error</i>
-1.0 – -0.5	5.9	0.64	1.3	1.5
-0.5 – 0.0	13.2	0.86	2.8	3.4
0.0 – 0.5	17.8	1.1	3.7	4.6
0.5 – 1.0	21.6	1.1	4.5	5.6
1.0 – 1.5	24.8	1.2	5.2	6.5
1.5 – 2.0	30.1	1.3	6.3	7.8

Table 5.5: Measured differential ep cross-section $d\sigma/d\eta^{jet}$ for inclusive jet production integrated over $E_T^{jet} > 11.0 \text{ GeV}$ in the kinematical range defined by $Q^2 < 0.01 \text{ GeV}^2$ and $0.25 < y < 0.7$.

η^{jet}	$d\sigma/d\eta^{jet} [nb]$	<i>stat.error</i>	<i>syst.error</i>	<i>syst.overall error</i>
-0.5 – 0.0	1.23	0.20	0.26	0.32
0.0 – 0.5	1.85	0.24	0.39	0.48
0.5 – 1.0	2.36	0.30	0.50	0.61
1.0 – 1.5	3.30	0.35	0.69	0.86
1.5 – 2.0	3.27	0.33	0.69	0.85

Table 5.6: Measured differential ep cross-section $d\sigma/d\eta^{jet}$ for inclusive jet production integrated over $E_T^{jet} > 15.0 \text{ GeV}$ in the kinematical range defined by $Q^2 < 0.01 \text{ GeV}^2$ and $0.25 < y < 0.7$.

η^{jet}	$d\sigma/d\eta^{jet} [nb]$	<i>stat.error</i>	<i>syst.error</i>	<i>syst.overall error</i>
0.0 – 0.5	0.50	0.12	0.11	0.13
0.5 – 1.0	0.48	0.12	0.10	0.13
1.0 – 1.5	0.67	0.15	0.14	0.17
1.5 – 2.0	0.65	0.14	0.14	0.17

Table 5.7: Measured inclusive differential jet ep cross-section $d\sigma/d\eta^{jet}$ after a correction for the underlying event energy. The error bars reflect the statistical and systematic errors, added in quadrature. The kinematical range is defined by $Q^2 < 0.01 \text{ GeV}^2$ and $0.25 < y < 0.7$.

E_T^{jet} threshold [GeV]	$d\sigma/d\eta^{jet} [nb]$ for $1 < \eta^{jet} < 1.5$	$d\sigma/d\eta^{jet} [nb]$ for $1.5 < \eta^{jet} < 2$
7	14.1 ± 6.9	17.8 ± 8.7
11	2.2 ± 1.0	2.2 ± 0.9
15	0.54 ± 0.25	0.52 ± 0.24

Chapter 6

Observation of Hard Processes in Diffractive Scattering in Photoproduction

“A diffractive process occurs if and only if there is a large rapidity gap in the produced–particle phase space which is not exponentially suppressed.”

J.D.Bjorken [90]

6.1 Rapidity gap events

As was mentioned previously, HERA gives an opportunity to study the single diffractive dissociation channels $\gamma p \rightarrow Xp'$ (photon diffractive dissociation) and $\gamma p \rightarrow VX$ (proton diffractive dissociation). If the momentum transfers $(p_p - p_{p'})^2$ and $(p_\gamma - p_V)^2$ are small, then these processes proceed through the exchange of a colorless object, like a Pomeron. There is no color flow from the target particle, which stays intact, to the other final state particles. Therefore, single diffractive dissociation at high centre of mass energies can be recognized by an absence of energy in the region between the non-dissociated hadron and the particles of the dissociated system (so called *rapidity gap*)¹.

To quantify a rapidity gap we introduce the variable η_{max} , which is the pseudorapidity either of the most forward calorimetric energy deposit of more than 400 MeV or the most forward detected track with a transverse momentum $p_T > 150$ MeV.² Distributions of LAr cluster energies and transverse momenta of reconstructed tracks are shown in Fig.6.1. The results given below do not change qualitatively varying the minimum cluster energy

¹An exact method to identify a single photon diffractive dissociation process $\gamma p \rightarrow Xp'$ is to detect proton which is scattered through the very small angles. For this purpose in 1994 a special forward proton spectrometer was installed.

²In this thesis pseudorapidity gap is abbreviated to rapidity gap.

and the track p_T requirements by 30%. The largest pseudorapidity which can be observed in the H1 liquid argon calorimeter, η_{LAr} , is about 3.65 and in the forward tracker, η_{FT} , about 3. These values vary slightly according to the position of the ep event vertex.

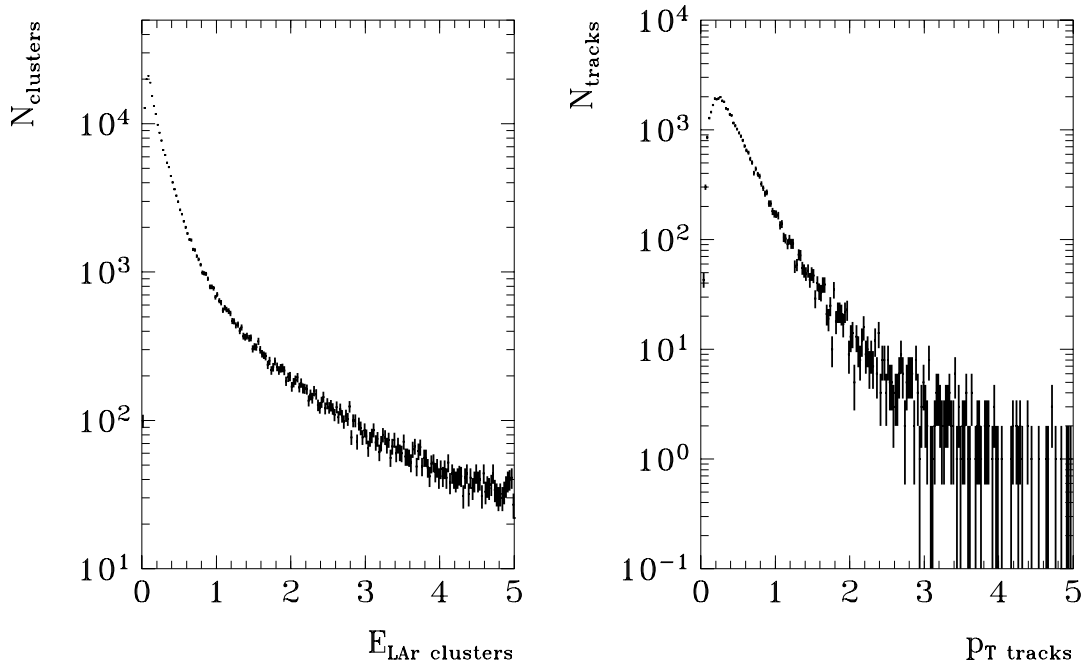


Figure 6.1: Distributions of the LAr cluster energy and transverse momentum of the tracks.

In Fig.6.2 the η_{max} spectrum is shown for the *minimum bias* sample of photoproduction events. In all figures in this chapter, the data points are not corrected for detector effects and systematic errors are not taken into account.

For most of the events, there is an energy deposit close to η_{LAr} (see Fig.6.2)³. However, there is also a class of events which have a small η_{max} value, i.e. a large empty region in the calorimeter and the tracker in the proton direction.

The η_{max} spectrum can be qualitatively understood by comparing it with model predictions for diffractive and non-diffractive processes. In order to simulate the soft diffractive and non-diffractive models, the PYTHIA Monte-Carlo was used (see for details section 3.6.1). For the non-diffractive part multiple interactions have been included. The comparison with the PYTHIA Monte Carlo predictions in Fig.6.2 shows that the events with small η_{max} are consistent with photon diffractive dissociation. The non-diffractive prediction (PYTHIA-nd; hatched histogram) exhibits a sharp fall off with increasing gap

³Values of $\eta_{max} \gtrsim 3.65$ which are outside the LAr acceptance occur when a cluster is formed by many cells around the beam-pipe in the forward direction.

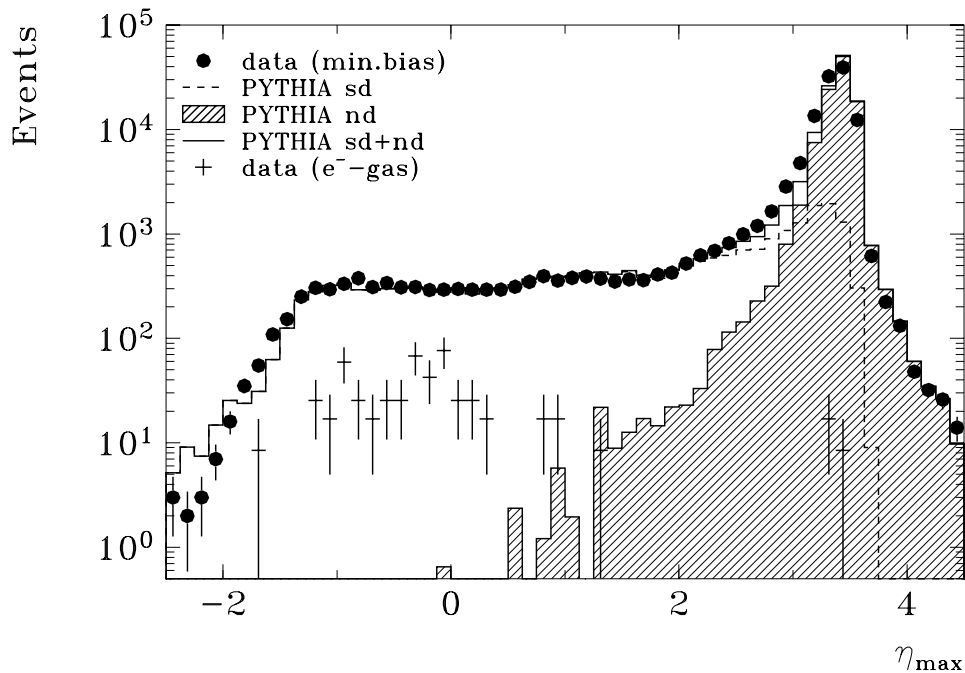


Figure 6.2: Maximum pseudorapidity η_{max} distribution in γp events compared to a single diffractive (*sd*, dashed line) and a non-diffractive (*nd*, hatched histogram) Monte Carlo model, and their sum (full line). Crosses are the expected contamination of e^- -gas background (calculated from e^- -pilot bunches).

size, i.e. decreasing η_{max} , and clearly does not account for the η_{max} tail for $\eta_{max} < 2$. The photon diffractive dissociation component (PYTHIA-*sd*; dashed line), calculated with the soft diffractive model, gives a good description of the spectrum for $\eta_{max} < 2$.

The distribution for the soft diffractive model is normalized to the region $\eta_{max} < 2$, while the distribution for the non-diffractive model is normalized to $\eta_{max} > 3$. Overall, the sum of the soft diffractive and non-diffractive γp Monte Carlo calculation (full line) accounts reasonably well for the observed η_{max} spectrum.

To study the properties of the events with a large rapidity gap, events with $\eta_{max} < 1.5$ have been selected. In addition, the selection required the energy summed over the calorimeter cells with $\eta > 1.5$ to be less than 1.0 GeV and the forward rapidity gap to be the largest in the event. The last requirements remove $\sim 7\%$ of events and do not influence the results given below but provide a clean sample. In total 7249 events survive the rapidity gap cut. This is about 6% of the total minimum bias photoproduction sample. The diffractive events, isolated by this cut, are the sum of photon single diffractive dissociation and a small proportion of double diffractive dissociation. The contamination of elastic events $\gamma p \rightarrow Vp'$ and proton single diffractive dissociation events $\gamma p \rightarrow VX$ is negligible ($< 1\%$) [19].

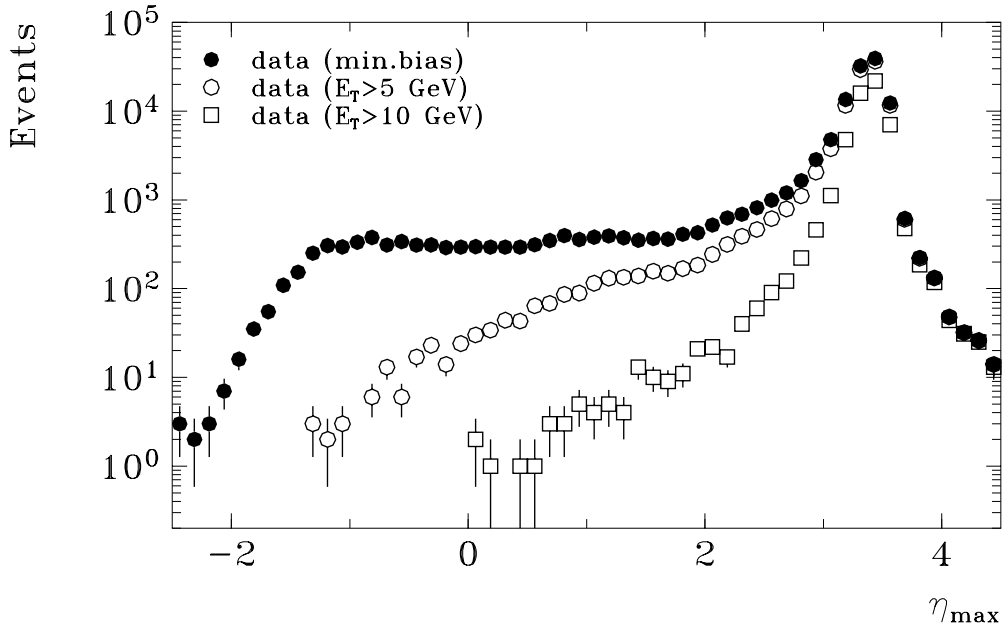


Figure 6.3: Maximum pseudorapidity η_{max} distribution in γp events for different cuts on the total transverse energy E_T .

Other Reggeon exchanges (e.g. π , $f_2(1270)$...) can give rise to rapidity gaps as well. However, due to the nature of the η_{max} cut applied here, a region of $M_x^2/s \approx x_{P/p} \lesssim 2 \times 10^{-2}$, is implicitly selected (see Fig.6.4d), where Pomeron exchange is expected to dominate over Reggeon exchange [91] (see section 3.5)⁴. (Here $x_{P/p}$ is the momentum fraction of the proton carried by the Pomeron.)

Due to the cut $\eta_{max} < 1.5$, we select diffractive events with small masses of the dissociative system M_X , namely less than about 20 GeV (see Fig.6.4a,c). This is reflected also in Fig.6.3, where the η_{max} distribution is shown for different cuts on the total transverse energy in the event. Increasing minimal E_T leads to a decrease of the tail at low η_{max} values.

The background in the rapidity gap sample, due to accidental coincidence of a proton beam gas interaction with an electron scattered at small angle in the same event is negligible. Using data taken with a non-colliding proton bunch and using the rate of the small angle electron detector alone, this background was estimated to be less than 0.1%. The remaining background from electron-gas interaction events was found to be more important. 59 events in this sample have been taken from pilot electron bunches. Taking into account the average ratio of the total beam current to the electron pilot bunch current $\langle R(e) \rangle \approx 8.3$, the contamination of this background is estimated to be $6.8 \pm 0.9\%$ and

⁴Pomeron exchange is dominant over Reggeon exchange for $x_F > 0.9$, where x_F is Feynman- x , $x_F \approx 1 - x_P$.

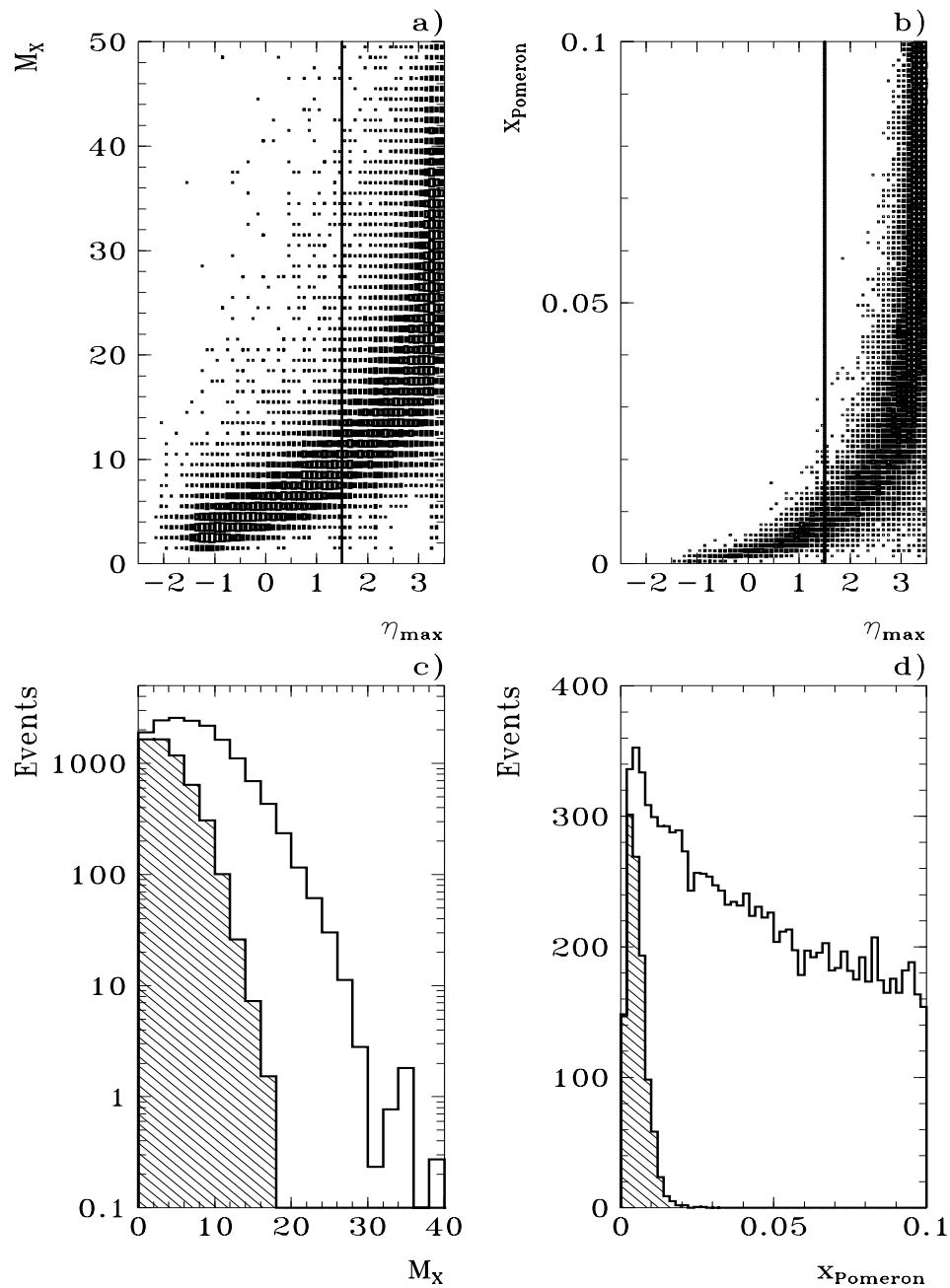


Figure 6.4: **a)** Correlation between η_{max} and generated invariant mass of diffractive system M_X ;
b) correlation between η_{max} and momentum fraction of proton carried by Pomeron x_P ;
 The straight lines in **a)** and **b)** indicate the rapidity gap cut.
c) distribution of generated invariant masses of the diffractive system M_X for all generated events and for events selected by the rapidity gap cut $\eta_{max} < 1.5$ (hatched histogram);
d) distribution of the momentum fraction of the proton carried by the Pomeron x_P for all generated events and for events selected by the rapidity gap cut (hatched histogram).

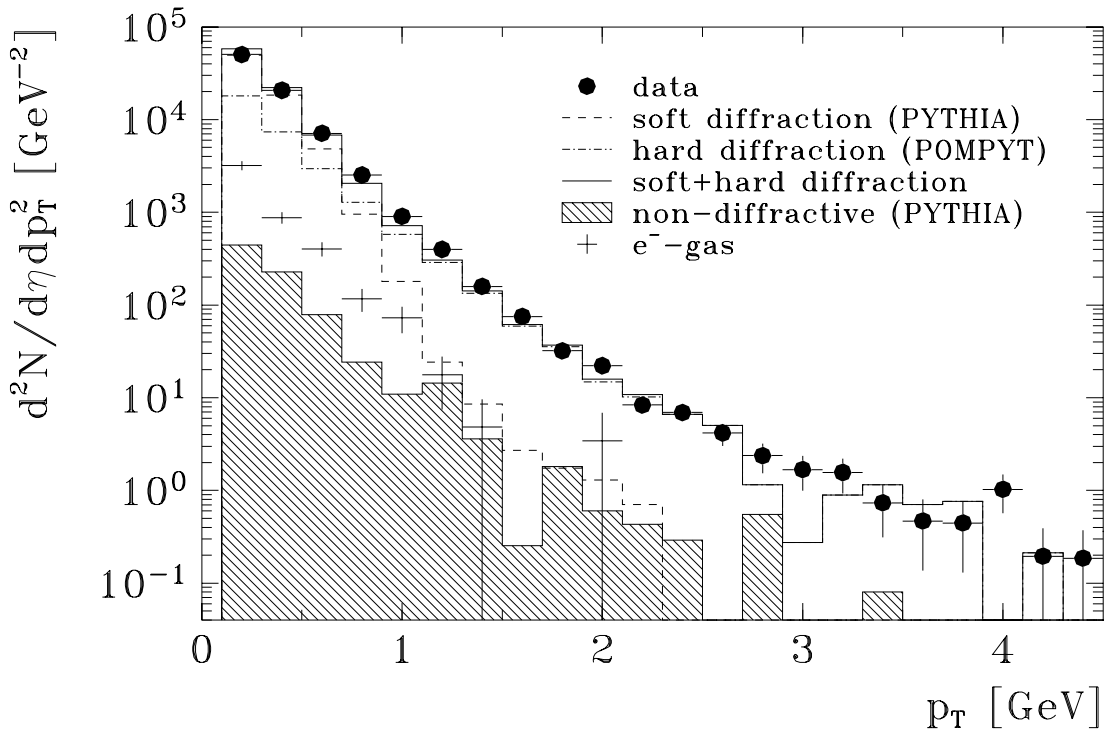


Figure 6.5: Transverse momentum distribution of charged particles in the range $-1.5 < \eta < 1.5$ for events with a large rapidity gap ($\eta_{max} < 1.5$) compared to Monte Carlo predictions.

is indicated by crosses in the Fig.6.2. The electron background depends significantly on total transverse energy in the event. For events with $E_T > 5 \text{ GeV}$ this background is less than 1%.

If diffractive dissociation involves a hard process then the corresponding underlying parton interaction can reveal itself in, for example, a large p_T tail in the inclusive single particle distribution. In Fig.6.5 the p_T spectrum for charged tracks in the range $-1.5 < \eta < 1.5$ is shown. The shape of the distribution shows an exponential fall off at small p_T values with a large tail extending to $p_T \sim 5 \text{ GeV}$. The same observation was made for the p_T spectrum measured in the total inclusive photoproduction sample [25], where the events in the tail were identified with hard scattering in γp interactions.

The transverse momentum distribution of charged particles for events with a large rapidity gap is shown in Fig.6.6 together with the uncorrected spectrum for events without rapidity gap. Distributions are normalized to the first point. Events without rapidity gap exhibit a larger tail at high p_T which can be attributed to the larger phase space available for high p_T particle production.

The shape of the p_T spectrum is compared in Fig.6.5 with the soft diffractive model pre-

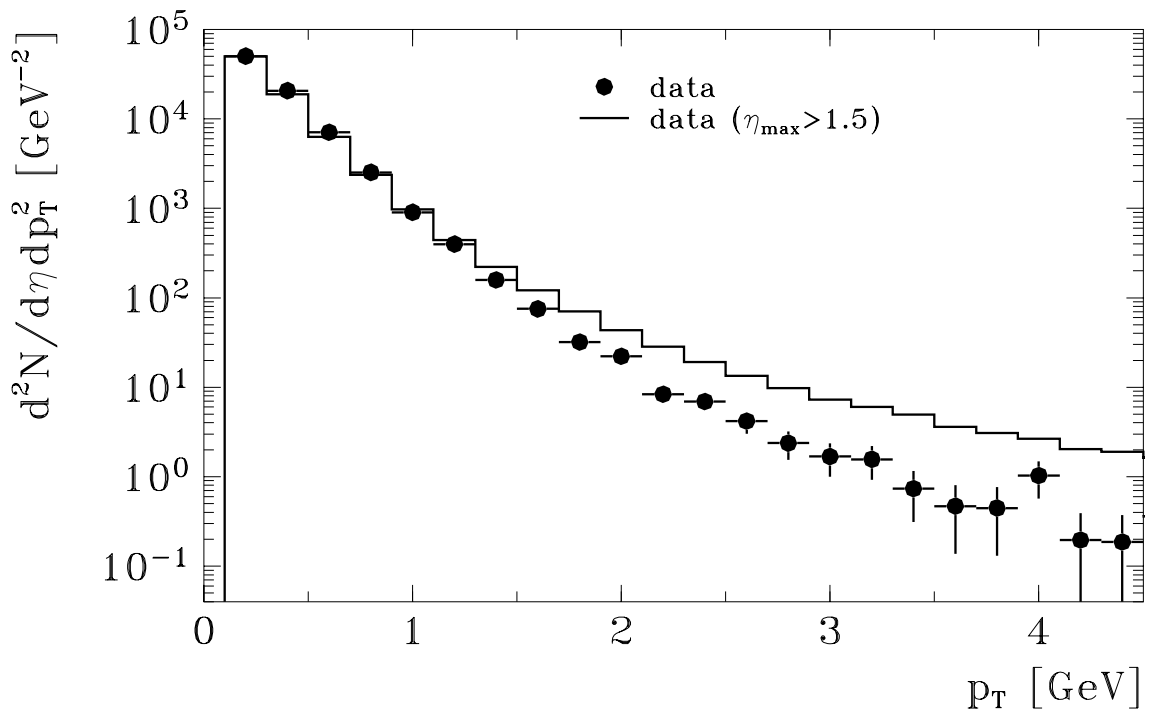


Figure 6.6: Transverse momentum distribution of charged particles for events with (points) and without (histogram) large rapidity gap ($\eta_{max} < 1.5$). (Points are the same as in Fig.6.5)

diction from PYTHIA and the diffractive hard scattering model prediction from POMPYT. Two extreme choices of parton distribution functions in POMPYT were considered in this analysis. The Pomeron was assumed to consist of gluons. The parton distribution function within the Pomeron was taken to be either “hard”, $zg(z) \sim z(1-z)$, hereafter labeled “G0”, or “soft”, $zg(z) \sim (1-z)^5$, hereafter labeled “G5”. The variable $z = x_{g/P}$ is the fraction of the Pomeron momentum carried by the struck gluon involved in the interaction. Since no essential differences are found between the predictions of POMPYT with soft and hard Pomeron distribution functions for the p_T spectrum, only POMPYT with hard gluonic structure function (G0) is shown in Fig.6.5.

The prediction of the soft diffractive model is normalized to the region $p_T < 0.5 \text{ GeV}$, the POMPYT prediction is normalized to the region $p_T > 1.5 \text{ GeV}$, and their sum is normalized to the total spectrum.

The contribution to the p_T spectrum of events from the hard interactions between the partonic content of the photon and the proton, i.e. the remaining non-diffractive events in the rapidity gap sample, is predicted to be small, namely less than 30 events. The hatched histogram and crosses in Fig.6.5 show the expected background from non-diffractive

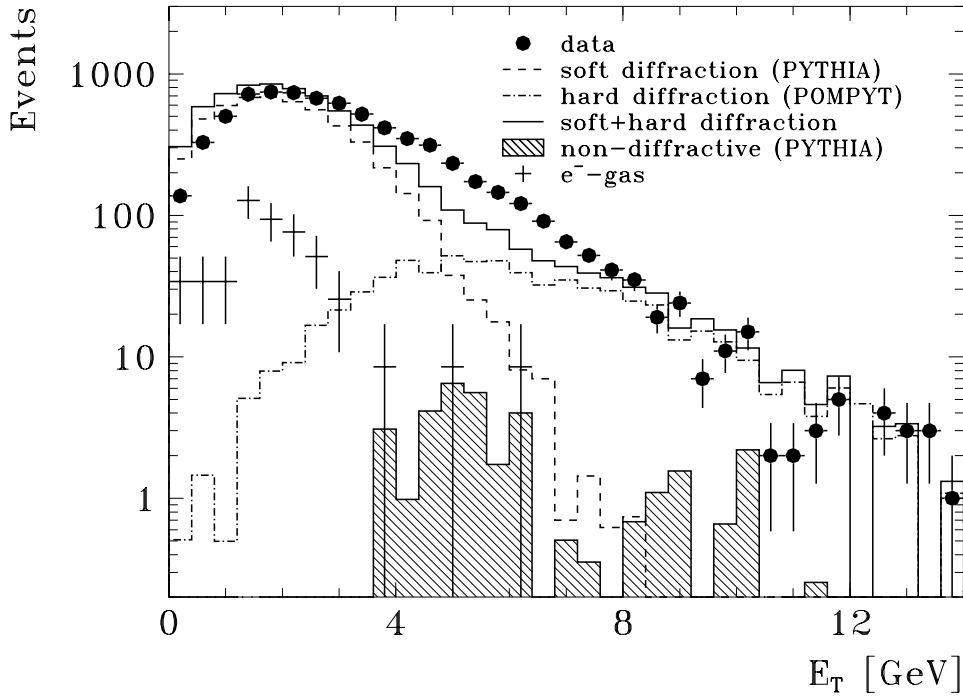


Figure 6.7: Distribution of total transverse energy for events with large rapidity gap ($\eta_{max} < 1.5$) compared to Monte Carlo predictions. Description of points and histograms are the same as for Fig.6.5.

photon–proton and electron–gas interactions, respectively. Obviously, this background accounts only for a small fraction of the observed distribution.

The soft diffraction model describes well the exponential fall of the data at small p_T , which represents the bulk of the data, but clearly cannot account for the p_T tail. POMPYT gives a satisfactory description of the large p_T region. The overall p_T distribution is well described by the sum of a soft and a hard diffractive component (full line).

Similar studies can be done in the distributions of the total transverse energy, the transverse momentum of the most energetic track and the charged track multiplicity in the events with $\eta_{max} < 1.5$ cut (Fig.6.7-6.9). The data are again compared to the soft and hard diffractive models (dashed and dash-dotted lines, respectively). The difference between the POMPYT predictions with the soft and the hard structure functions is only marginal, therefore again only the “G0” predictions are shown. The predictions of the soft diffractive model are normalized to the region of low energy and multiplicity ($E_T < 3 \text{ GeV}$ for Fig.6.7, $p_{T \text{ max}} < 0.6 \text{ GeV}$ for Fig.6.8 and $N_{\text{charged tracks}} < 5$ for Fig.6.9). POMPYT predictions are normalized to the large transverse energy and multiplicity tail ($E_T > 8 \text{ GeV}$ for Fig.6.7, $p_{T \text{ max}} > 1.0 \text{ GeV}$ for Fig.6.8 and $N_{\text{charged tracks}} > 9$ for Fig.6.9).

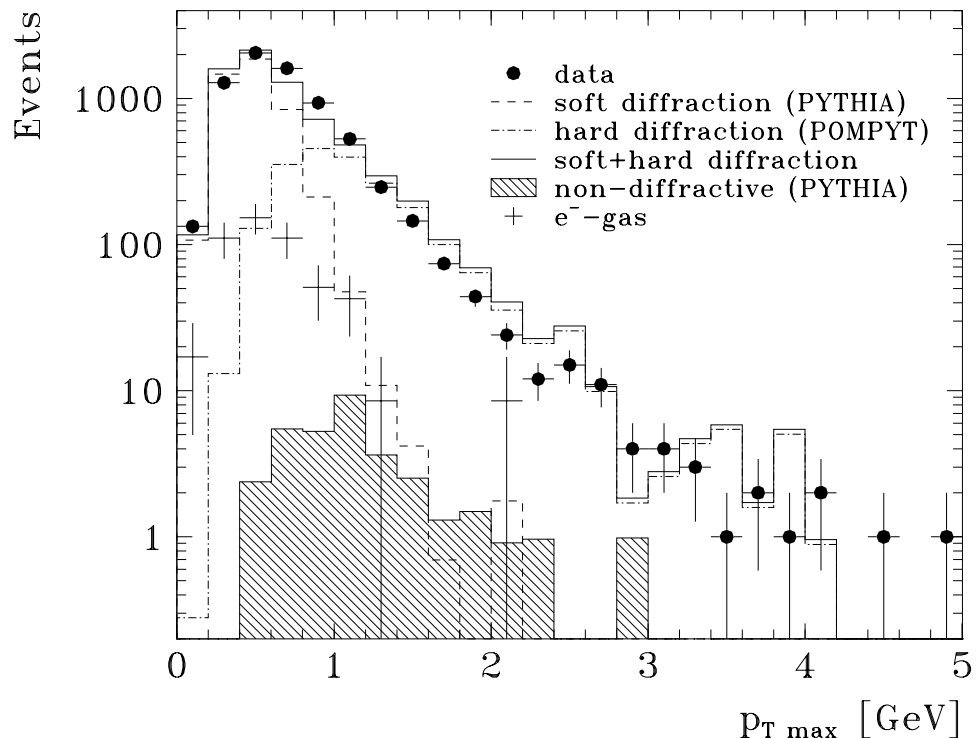


Figure 6.8: Distribution of transverse momentum of the most energetic track for events with a large rapidity gap ($\eta_{max} < 1.5$) compared to Monte Carlo predictions. Description of points and histograms are the same as for Fig.6.5.

The full line is the sum of distributions for soft and hard models, normalized to the total number of events in data. The expected contamination of non-diffractive events and electron-gas interactions are shown by the hatched histogram and crosses, respectively. The average charge multiplicity as function of E_T in the events is shown in Fig.6.10. The soft model describes well the distribution at small E_T values ($E_T < 4$ GeV), but clearly fails to describe the large E_T part. For the hard diffraction model it is vice versa. The combination of soft and hard models gives a satisfactory description of the data.

The results of this comparison are in qualitative agreement with those from the charged particle momenta distribution, however, there is a discrepancy between the data and Monte-Carlo for the transverse energy spectrum (Fig.6.7) and for the charged multiplicity (Fig.6.9) in the transition region from the soft to the hard region.

Thus, we can conclude, that data, selected by a rapidity gap cut, exhibit features of a hard scattering processes, i.e. production of high p_T particles and large transverse energies. These features can be described only with a model, which assumes hard parton-parton interactions in diffractive processes. The agreement with the diffractive hard scattering

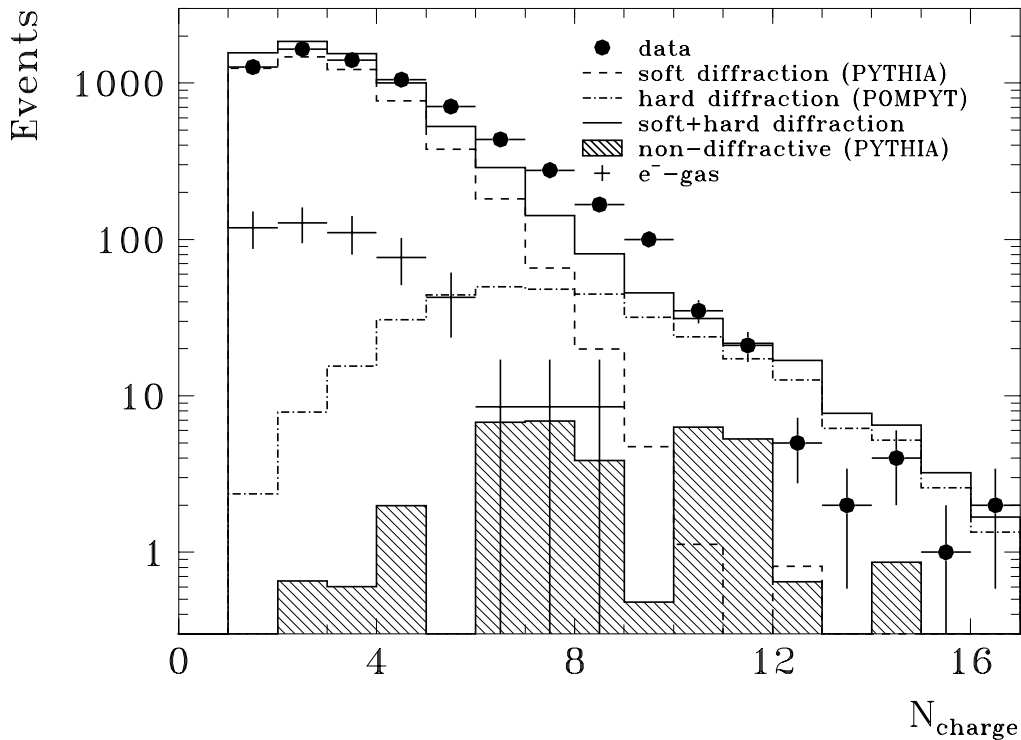


Figure 6.9: Distribution of charged multiplicity for events with large rapidity gap ($\eta_{max} < 1.5$) compared to Monte Carlo predictions. Description of points and histograms are the same as for Fig.6.5.

model may thus be taken as an indication for hard scattering at the parton level in photon diffraction.

6.2 Jets in rapidity gap events

To substantiate the above evidence for hard scattering, a search was made for jet structures in the data sample of photoproduction events with a total transverse energy larger than 5 GeV (*high E_T sample*), which used an integrated luminosity of 289 nb^{-1} . A jet finding algorithm was applied to search for jets with $E_T^{jet} > 4 \text{ GeV}$ in the range $-1 < \eta^{jet} < 1.5$. For the present study, calorimeter cells from the region $-2.0 < \eta_{cell} < 2.5$ were considered in the jet search. In total 24660 events with at least 1 jet have been found. In this sample there were no events from the electron pilot bunch, therefore background can be estimated to be less than 0.05% and is neglected in following.

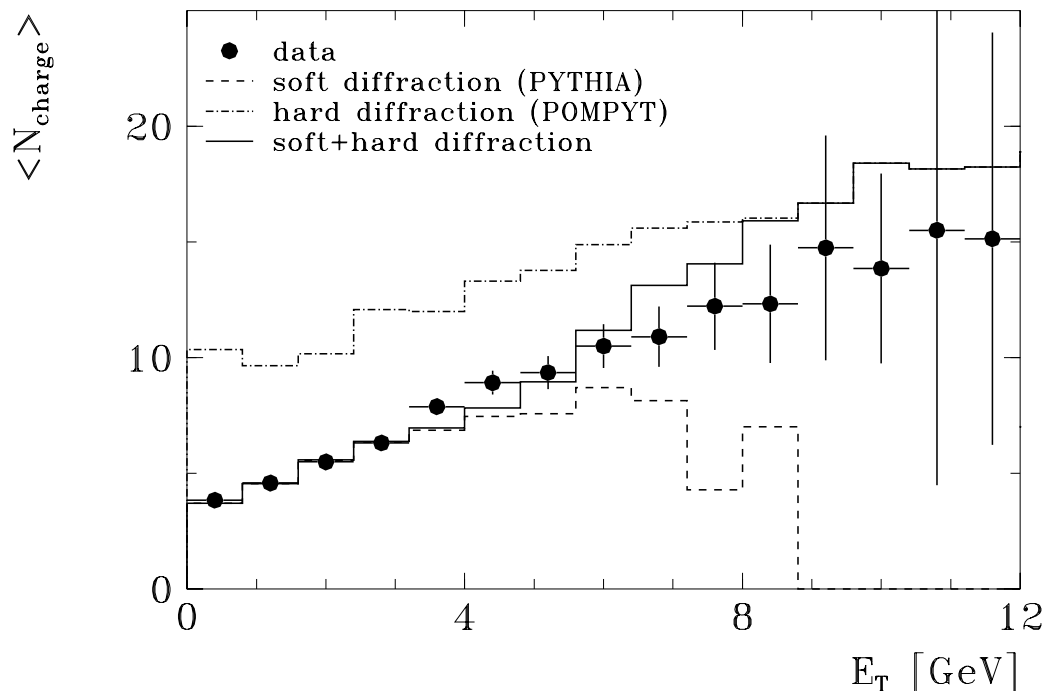


Figure 6.10: Average charged multiplicity $\langle N_{charge} \rangle$ as function of the total transverse energy in the event E_T for events with large rapidity gap ($\eta_{max} < 1.5$) compared to Monte Carlo predictions.

The η_{max} distribution for these events is shown in Fig.6.11. The distribution shows the same characteristics as Fig.6.2, namely most events have an η_{max} close to η_{Lar} , but a clear signal of events with $\eta_{max} < 2$ is observed. The reduction in the proportion of events in the $\eta_{max} < 1$ region compared to all data (see Fig.6.2) is a consequence of the reduced phase space available for jet production (see also Fig.6.3). The η_{max} cut is strongly correlated with the hadronic mass of the diffractively produced system. Requiring η_{max} to be small preferably selects small M_X events, which have less phase space for the production of jets (see Fig.6.4). In Fig.6.11 the data have been compared with non-diffractive γp (PYTHIA; hatched histogram) and diffractive hard scattering γ -Pomeron (POMPYT; dashed and full lines) predictions. The non-diffractive prediction is normalized to the total number of events, and the hard diffractive predictions are normalized to the number of events with $\eta_{max} < 2$. The non-diffractive model clearly cannot account for the η_{max} distribution at small values. The POMPYT model accounts better for the shape of the η_{max} spectrum, with a slight preference for the configuration including a hard gluon distribution (G_0) for the Pomeron.

As before, a diffractive sample is selected by selecting events with $\eta_{max} < 1.5$ with

additional requirements on this forward rapidity gap to be the largest gap in the event and demanding the calorimetric energy in the range $\eta > 1.5$ to be less than 1.0 GeV . Without the requirement for a jet to be present 1632 events are selected. In this rapidity gap sample 135 events contain jets, from which 116 events contain one jet and 19 events contain 2 jets. The contamination by the non-diffractive γp interactions in this sample is estimated to be 4 events by analysis of the non-diffractive PYTHIA Monte-Carlo (with multiple interactions) events. This contribution is not considered further.

The profiles of jets with $4 < E_T^{jet} < 6 \text{ GeV}$ and $|\eta^{jet}| < 0.5$ are shown in Fig.6.12 and compared with those of jets in photoproduction events selected as above but with the requirement that there be no large forward rapidity gap, namely $\eta_{max} > 1.5$. The profiles are observed to be similar with the exception of the large $\Delta\eta$ region ($1 < \Delta\eta < 2$ in Fig.6.12b). This discrepancy is due to the absence of energy in this region due to the rapidity gap selection. The somewhat smaller pedestal in the $\Delta\varphi$ distribution for events with rapidity gap can be explained by kinematical reasons. The total energy of the Pomeron-photon system for diffractive events is much smaller than the total energy

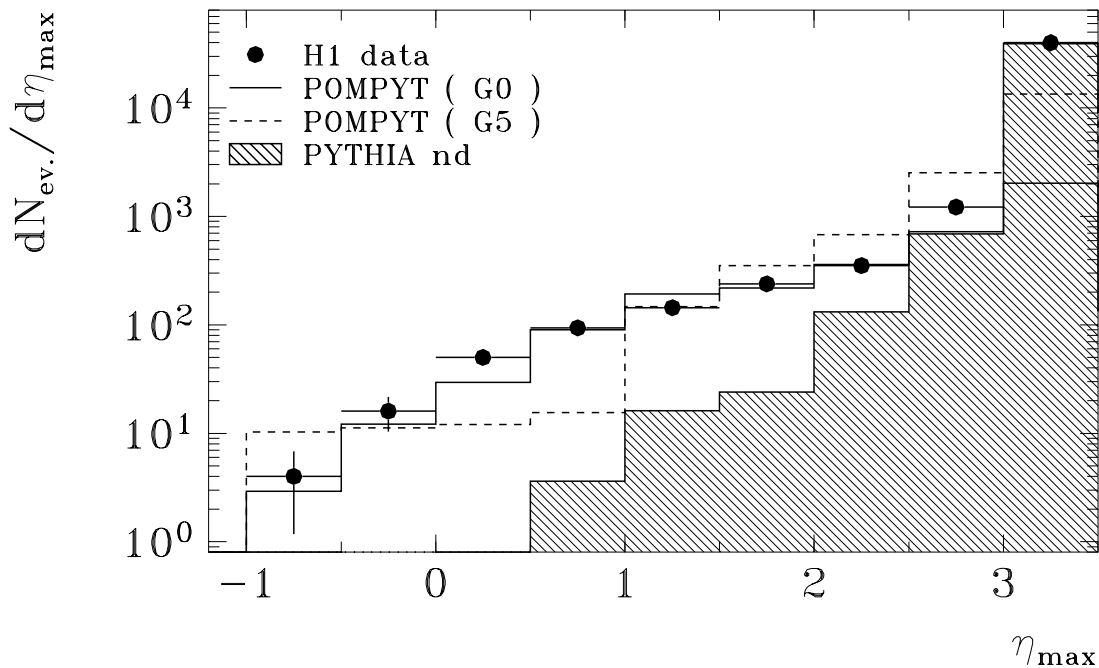


Figure 6.11: Maximum pseudorapidity η_{max} distribution in tagged γp events containing jets with $E_{T_{jet}} > 4 \text{ GeV}$ in the interval $-1.0 < \eta_{jet} < 1.5$, compared to Monte Carlo expectations from a non-diffractive process (hatched area) and a diffractive process assuming a Pomeron with hard (G0; full line) and soft (G5; dashed line) gluon momentum distribution.

of the proton-photon system for non-diffractive events, which restricts the phase space available for jet production for diffractive events. Therefore, the probability to have large hadronic activity outside the jets is obviously smaller for these events.

The diffractive hard scattering Monte Carlo calculation as given by POMPYT describes jet profiles in the rapidity gap event fairly well. An example of an event with 2 jets, with an E_T^{jet} of 7 GeV and 4 GeV for the jets, is shown in Fig.6.13. The back-to-back structure of the 2 jets is clearly observed in the adjacent transverse view of the detector and in the $E(\eta, \varphi)$ distribution.

In order to make sure that the identified jets indeed come from hard parton-parton interactions, a search was made for jets in the soft diffractive Monte-Carlo events containing more than 10 GeV total transverse energy, which is sufficient for two jets of 4 GeV. Soft interactions also can produce events where large transverse energy will be deposited within a narrow cone, which can be identified as transverse jets. But in contrast to hard interactions this “jet” is compensated by energy which is spread over a wide region in $\eta - \varphi$ space, i.e. *soft* events do not produce two-jet structures, typical for hard interactions. Moreover, the expected number of “jet” events from a soft diffractive Monte-Carlo, is low: only 6 events, compared to 135 events in the data.

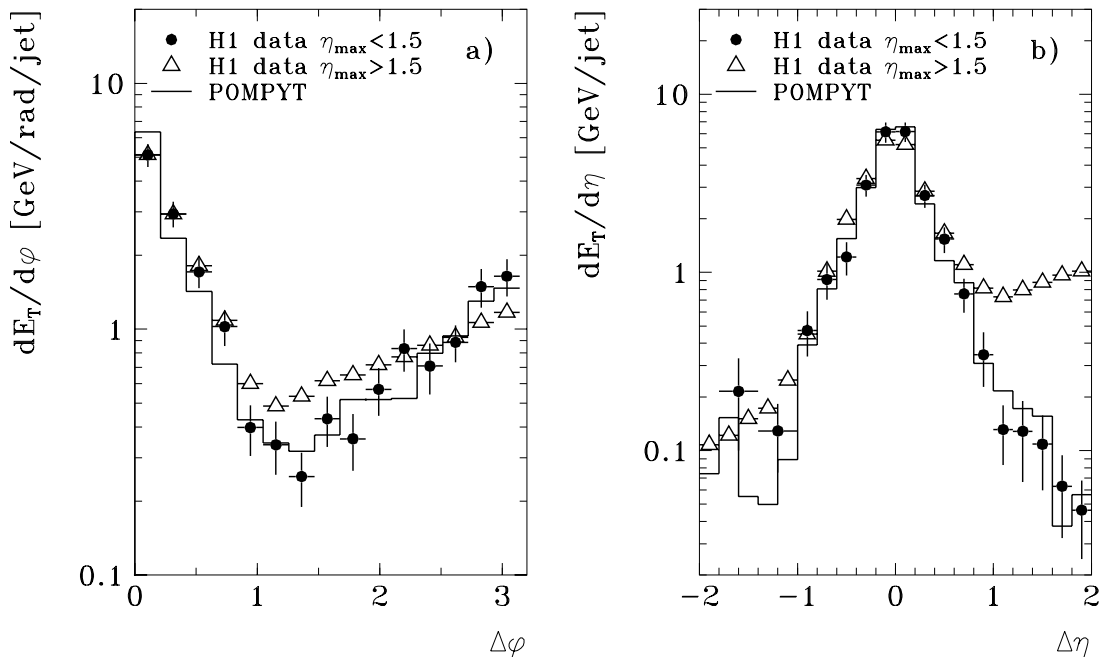


Figure 6.12: Transverse energy flow around the jet axis for jets with $4 < E_T^{jet} < 6$ GeV and $|\eta^{jet}| < 0.5$: for data with $\eta_{max} < 1.5$ (circles), for data with $\eta_{max} > 1.5$ (triangles), and for Monte Carlo events with $\eta_{max} < 1.5$ (full line).

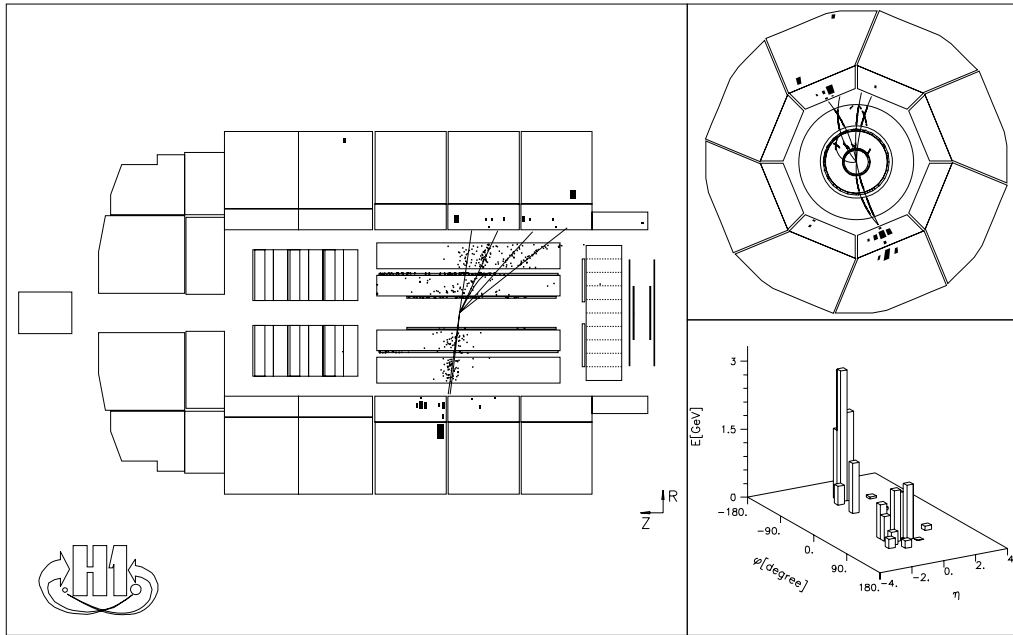


Figure 6.13: Two-jet event with a large rapidity gap in the H1 detector.

The transverse energy E_T^{jet} spectrum of all jets in the rapidity gap events is shown in Fig.6.14 as well as the distribution of the jet pseudorapidities, η^{jet} , and the azimuthal angle between the jets, $\Delta\varphi(jet1 - jet2)$, for the two jet events. For two jet events, the jets are clearly observed to be back-to-back in azimuth, a characteristic feature for a hard scattering process. The E_T^{jet} and the η^{jet} spectra are compared with the shape of the POMPYT expectation, normalized to the number of events with $\eta_{max} < 1.5$, for the hard and soft choices of the Pomeron parton distribution functions. The observed jets behave as expected from parton-parton scattering kinematics and are well described by the POMPYT Monte Carlo predictions. POMPYT with a hard gluonic parton distribution in the Pomeron ($G0$) gives a somewhat better description of the data than with a soft one ($G5$), but the soft gluon structure function cannot be excluded with the present statistics and normalization uncertainty in the model.

The dependence of the jet multiplicity on the total transverse energy E_T in event is shown in Fig.6.15a. With the given selections the fraction of jet events with respect to the total number of events is increasing with E_T . For $E_T > 12$ GeV more than 80% of the events contain at least one jet and more than 50% contain two jets. The fraction of the total transverse energy E_T carried by two jets is more than 80% and almost independent of E_T (Fig.6.15b). For events with $E_T > 5$ GeV the fraction of jet events is 8.3%. This result is compared with POMPYT predictions in Table 6.1.

It should be noted that the data sample contains a soft diffractive contribution which remains even after our cuts in this phase space region and may influence the proportion

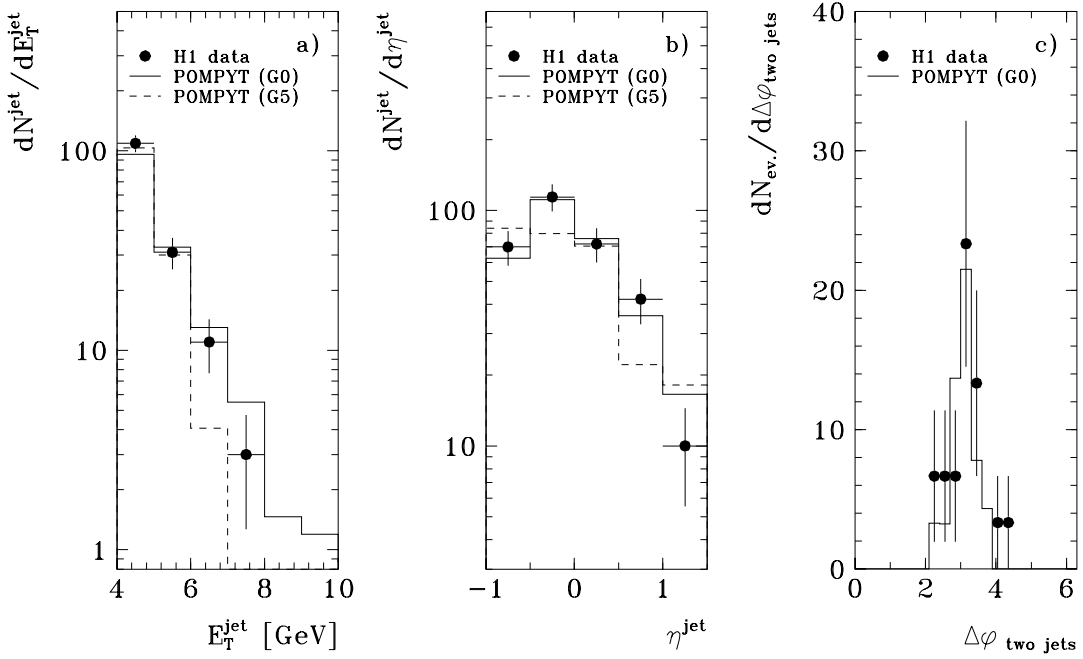


Figure 6.14: (a,b) Inclusive jet distributions for large rapidity gap events ($\eta_{max} < 1.5$): transverse energy E_T^{jet} and pseudorapidity η^{jet} . (c) Distribution of the azimuthal angle $\Delta\varphi$ between the jets for 2 jet events. The data are compared with Monte Carlo predictions assuming a Pomeron with hard ($G0$; full line) and soft ($G5$; dashed line) gluon momentum distribution.

Table 6.1: Jet rates: data compared to POMPYT Monte Carlo calculations for γp events with $E_T > 5 \text{ GeV}$ and $\eta_{max} < 1.5$, and for jets with $E_T^{jet} > 4 \text{ GeV}$ and $-1 < \eta^{jet} < 1.5$.

Sample	jet events(%)
Data (1632 events)	(135 ev.) 8.3 ± 0.7
POMPYT $G0$ ($\hat{p}_T^{min} = 2 \text{ GeV}$, 1112 ev.)	(203 ev.) 18.2 ± 1.2
POMPYT $G5$ ($\hat{p}_T^{min} = 2 \text{ GeV}$, 359 ev.)	(19 ev.) 5.3 ± 1.2

Table 6.2: Jet rates: data compared to POMPYT Monte Carlo calculations for γp events with $E_T > 9 \text{ GeV}$ and $\eta_{max} < 1.5$, and for jets with $E_T^{jet} > 4 \text{ GeV}$ and $-1 < \eta^{jet} < 1.5$.

Sample	1 jet events(%)	2 jet (%)	2-jet/1-jet
Data (142 events)	(55 ev.) 38.7 ± 4.1	(19 ev.) 13.4 ± 2.8	0.35 ± 0.09
POMPYT $G0$ (248 ev.)	(115 ev.) 46.4 ± 3.2	(25 ev.) 10.1 ± 1.9	0.22 ± 0.05
POMPYT $G5$ (33 ev.)	(9 ev.) 27.3 ± 7.7	(0 ev.) < 3	< 0.1

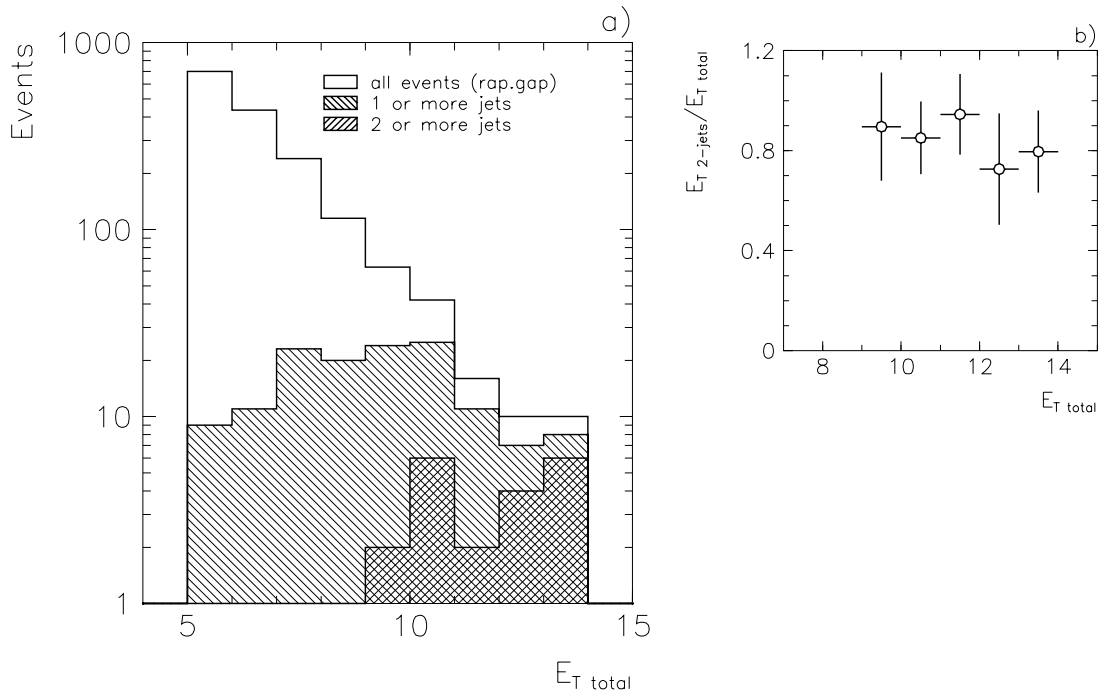


Figure 6.15: a) Jet multiplicity as function of the total transverse energy E_T in event. Open histogram shows E_T distribution for all events with rapidity gap, left hatched histogram— same distribution for events where at least one jet with $E_T^{jet} > 4 \text{ GeV}$ and $-1 < \eta^{jet} < 1.5$ is found, and right hatched histogram— same distribution for events where 2 jets are found.

b) Fraction of the total transverse energy E_T carried by two jets E_T^{2-jets} as function of E_T .

of jet events in the data and POMPYYT. The (2 jets)/(1 jets) ratio is less sensitive to this effect. In order to restrict to a region where phase space allows two-jet production and to reduce the sensitivity to the \hat{p}_T^{min} cut used in POMPYYT a comparison is made of data with these models by increasing the minimum E_T of the event.

Requiring the total E_T in the event to be more than 9 GeV , the total number of events with rapidity gap is 142. The number of one-jet events is 55, and the number of two-jet events is 19. The one and two jet fractions are then 38.7% and 13.4% respectively, and the ratio (2 jets)/(1 jets) is 0.35 ± 0.09 . These numbers are compared with POMPYYT predictions in Table 6.2. This ratio compares favorably with the prediction of a hard Pomeron parton distribution, but it should be noted that it depends somewhat on the choice of the \hat{p}_T^{min} value— changing \hat{p}_T^{min} by 500 MeV leads to a change in the ratio (2 jets)/(1 jets) of 15%.

These results depend only weakly on the uncertainty in the hadronic energy scale. Changing the scale by -5% leads to a decrease and by $+5\%$ to an increase of the pro-

portion of one and two jet events to all events and of the ratio (2 jets)/(1 jets) within statistical errors.

Thus, the ansatz of hard scattering between partons in the photon and partons in the Pomeron, as for example implemented in POMPYT, is compatible with the results of the jet analysis of the data.

6.3 Conclusions

Events with a large rapidity gap with respect to the proton direction are observed in γp interactions in H1 at HERA. These events are interpreted as diffractive dissociation of the photon. When a sample of such diffractive events is selected by means of a cut $\eta_{max} < 1.5$, features attributable to the presence of hard partonic scattering are observed. The yield of charged tracks from these events, as a function of their transverse momentum, p_T , extends to values which cannot be accounted for in a model of p_T limited phase space, characteristic of present knowledge of soft diffractive processes. A model which includes hard scattering between partons in the photon and in the Pomeron reproduces well the charged particle yield p_T and the distribution of transverse momentum of the most energetic track $p_{T\ max}$ in the data. Jets are found in the diffractive data sample. In two jet events, the jets are back-to-back in azimuth, substantiating the evidence for hard partonic scattering in diffractive collisions.

Chapter 7

Summary

At HERA ep scattering is dominated by the exchange of almost real photons ($Q^2 \ll 1 \text{ GeV}^2$). The total average energy of the photon–proton system of about $\sqrt{s_{\gamma p}} \approx 200 \text{ GeV}$ opens a new kinematical domain not accessible in previous fixed target experiments.

Photon–proton collisions are expected to follow largely the same phenomenology as hadron–hadron collisions, consequently the majority of the γp events are expected to be of rather soft nature. However, a fraction of the γp interactions exhibits hard scattering features, leading to jets with large transverse energy in the final state. Two types of processes contribute to large E_T photoproduction: the incoming photon interacts either directly with a parton in the proton (*direct component*) or the photon acts as a source of partons which collide with the partons in the proton (*resolved component*). In direct processes the full energy of the photon enters the hard subprocess, whereas in the resolved case a part of the photon energy is taken by the spectator partons, which do not contribute to a hard interaction. In case of resolved processes one can define the photon as having a structure, described by a structure function. The large centre of mass energy at HERA allows a separation of the resolved and direct components and, similar to high energy hadronic interactions, clear jet production and jet structure. It has been suggested, that assuming the parton densities in the proton are known, the measurement of these cross–sections will yield informations on the parton structure of the photon, particularly the gluon distribution, about which very little is known at present.

The underlying theoretical framework is the QCD improved parton model. The leading order (LO) QCD calculations are embedded in Monte Carlo programs which include the structure functions of the proton and photon, models for fragmentation, higher order effects, and possible additional interactions between the spectator partons.

From the data collected during 1993 with the H1 detector a sample of hard photoproduction events was selected.

The cone–type jet algorithm was applied for the jet search. Using the selected data sample the inclusive jet cross–sections $d\sigma/dE_T^{jet}$ and $d\sigma/d\eta^{jet}$ have been measured in the kinematical range $Q^2 < 10^{-2} \text{ GeV}^2$ and $0.25 < y < 0.7$. These cross–sections refer to the hadron jets with a cone radius of one unit in $\eta - \varphi$ space. The cross–section $d\sigma/dE_T^{jet}$ has been measured in the E_T^{jet} range between 7 and 30 GeV , integrated over two η^{jet}

ranges ($-1 < \eta^{jet} < 2$ and $-1 < \eta^{jet} < 1$). The cross-section $d\sigma/d\eta^{jet}$ has been measured in the η^{jet} range between -1 and 2 integrated over E_T^{jet} for various thresholds ($E_T^{jet} > 7, 11, 15 \text{ GeV}$). Leading logarithm parton shower Monte-Carlo calculations using the predictions of currently available parametrizations of the photon parton distributions are compared to the measured jet cross-sections. It was shown that the main contribution to the measured cross-section in the kinematical range studied is due to the resolved component of the photon structure function with a substantial contribution from its gluonic component. These measurements are fully consistent with LO QCD if the calculations include in addition interactions of beam spectators. It was found that the underlying event energy has a large influence on the measured jet cross-sections in the region of small transverse energies $E_T^{jet} > 7 \text{ GeV}$ and large pseudorapidities $\eta^{jet} > 1$, the kinematic region which corresponds to small momentum fractions x_γ of the parton from the proton. Conclusions on the parton scattering processes at small x_γ from the jet cross-sections therefore depend on the details of description of the underlying event.

The measured cross-sections are compared also with the available next-to-leading order (NLO) QCD calculations. LO calculations have severe disadvantages compared to the NLO calculations. They suffer from large normalization uncertainties due to the renormalization and factorization scale dependence and the calculated cross-section exhibits no dependence on the cone size implicit in the jet definition. The disadvantage of the NLO calculations is that they are not available in the form of Monte-Carlo generators so far. In order to make the comparison between the data and the NLO calculations possible the data need to be corrected for underlying event energy and the fragmentation effects, which are not included in the calculations and may play an important role at the low E_T^{jet} values. This shows also the relevance of collecting data with higher E_T^{jet} , which do not suffer from such an ambiguity. It was shown, that these effects can account for the difference between the data and the NLO calculations at low E_T^{jet} . At the higher jet energies ($E_T^{jet} > 15 \text{ GeV}$) the agreement between the theoretical calculations and experimental results with respect to shape and absolute normalization is reasonable.

Further analyses with higher statistics are needed for better understanding of the underlying event energy. The analysis of multi-jet events can prove the existence of multiple parton-parton scattering. The measurements of the inclusive jet cross-section can give significant new constraints on the parton distribution in the photon.

Hard interactions have been studied in the diffractive dissociation processes. Before HERA only the UA8 experiment at the CERN Sp \bar{p} S collider has reported an evidence of hard interactions in the diffractive dissociation.

The sample of photon diffractive dissociation events have been selected by the requirement of a large rapidity gap in the proton direction. This sample contains about 6% of the total photoproduction event sample. In these events features which can be attributed to the hard partonic scattering have been observed, for instance, the yield of charged tracks from these events, as a function of their transverse momentum, p_T , extends to values which cannot be accounted for in a model of p_T limited phase space, characteristic of present knowledge of soft diffractive processes. Jets are found in the diffractive data sample. In two jet events, the jets are back-to-back in azimuth, as expected from the hard parton-parton scattering kinematics.

These features are well described by the model which assumes hard scattering between partons in the photon and in the Pomeron. Based on this analysis, for the first time an evidence of diffractive hard scattering in photoproduction was reported [92]. A Pomeron with a hard gluonic structure function can better account for the data, but no firm conclusion can be made given the normalization uncertainty in the models and the experimental errors.

The detailed analysis of the hard diffractive scattering, for instance, the extraction of the Pomeron structure function and a test of the factorization hypothesis in the photon diffractive dissociation, was not possible with the statistics available from the 1993 data. New analyses based on the higher luminosity will shed light on the nature of the Pomeron.

Bibliography

- [1] M. Breidenbach et al., Phys. Rev. Lett. **23** (1969) 935
- [2] R.P. Feynmann, “*Photon–Hadron Interactions.*”, W.A. Benjamin Co., New York, (1972)
- [3] R. Brock et al., CTEQ Collab., “*Handbook of perturbative QCD.*”, Rev. Mod. Phys. **67** (1995) 157
- [4] H1 Collab., “*The H1 detector at HERA.*”, DESY preprint DESY-93-103 (1993)
- [5] ZEUS Collab., “*The ZEUS detector.*”, Status Report (1993)
- [6] R. Brinkmann, DESY preprint DESY-M-95-08
- [7] H1 Calorimeter Group, Nucl. Inst. Meth. **A336** (1993) 460;
H1 Calorimeter Group, Nucl. Inst. Meth. **A336** (1993) 499;
H1 Calorimeter Group, Nucl. Inst. Meth. **A350** (1994) 57
- [8] A. Campbell, “*A RISC multiprocessor event trigger for the data acquisition system of the H1 experiment at HERA.*”, Int.Conf. Real Time’91, Julich
- [9] H1 Collab., Z.Phys. **C66** (1995) 525
- [10] A. Blondel and F. Jacquet, *In Proceedings of the Study of an ep Facility for Europe*, ed. U. Amaldi, DESY-79-48 (1971) p.391
- [11] V.N. Gribov and V.N. Lipatov, Sov.J.Nucl.Phys. **15** (1972) 438;
G. Altarelli and G. Parisi, Nucl. Phys. **B126** (1977) 298;
Yu. Dokshitzer, Sov. Phys. JETP **46** (1977) 641
- [12] Ya.Ya. Balitski and V.N. Lipatov, Sov.J.Nucl.Phys. **28** (1978) 1597;
E.A. Kuraev et al., Zh.Eksp.Teor.Fiz. **72** (1977) 377;
E.A. Kuraev et al., Phys. Lett. **B60** (1975) 50
- [13] H1 Collab., Nucl. Phys. **B439** (1995) 471;
ZEUS Collab., Z. Phys. **C65** (1995) 379
- [14] H1 Collab., Phys. Lett. **B354** (1995) 494;
H1 Collab., Nucl. Phys. **B449** (1995) 3;
ZEUS Collab., Phys. Lett. **B345** (1995) 576

- [15] H1 Collab., Phys. Lett. **B356** (1995) 118
- [16] H1 Collab., Z.Phys. **C63** (1994) 377
- [17] A.I. Lebedev, *In Proceedings of the HERA Workshop, Hamburg 1991*, eds. W. Buchmüller and G. Ingelman, p.1991;
A. Rostovtsev and V. Soloshenko, H1 internal report H1-08/93-309 (1993)
- [18] C.F. Weizsäcker, Z.Phys. **88** (1934) 612;
E.J. Williams, Phys.Rev. **45** (1934) 729
- [19] H1 Collab., DESY preprint DESY-95-162
- [20] ZEUS Collab., Z. Phys. **C63** (1994) 391
- [21] T.H. Bauer et al., Rev. Mod. Phys. **50** (1978) 2
- [22] G. Schuler and T. Sjöstrand, Nucl. Phys. **B407** (1993) 169
- [23] H1 Collab., Phys. Lett. **B297** (1992) 205
- [24] H1 Collab., Phys. Lett. **B314** (1993) 436
- [25] H1 Collab., Phys. Lett. **B328** (1994) 176
- [26] H1 Collab., Nucl. Phys., **B445** (1995) 195
- [27] ZEUS Collab., Phys. Lett. **B297** (1992) 404
- [28] ZEUS Collab., Phys. Lett. **B322** (1994) 287
- [29] ZEUS Collab., Phys. Lett. **B342** (1995) 417
- [30] W.J. Stirling, *In Proceedings of the HERA Workshop, Hamburg 1987*, ed. R.D. Peccei, p.185;
G. Schuler, *In Proceedings of the HERA Workshop, Hamburg 1991*, eds. W. Buchmüller and G. Ingelman, p.461
- [31] B.L. Combridge et al., Phys. Lett. **70B** (1977) 234;
E. Berger et al., Nucl. Phys. **B239** (1984) 522;
D.W. Duke and J.F. Owens, Phys. Rev. **D26** (1982) 1601
- [32] T. Sjöstrand, FERMILAB-PUB-85/119-T (1985)
- [33] PLUTO Collab., Z.Phys. **C26** (1984) 353 (1984);
PLUTO Collab., Phys. Lett. **B142** (1984) 111;
PLUTO Collab., Phys. Lett. **B149** (1984) 421;
PLUTO Collab., Nucl. Phys. **B281** (1987) 365
- [34] TASSO Collab., Z.Phys. **C31** (1986) 527
- [35] JADE Collab., Z.Phys. **C24** (1984) 231

- [36] CELLO Collab., Phys. Lett. **126B** (1983) 391 ;
CELLO Collab., *Contribution to the XXV International Conference on HEP, Singapore, 1990*
- [37] TPC/2 γ Collab., Phys. Rev. Lett. **54** (1985) 763;
TPC/2 γ Collab., Phys. Rev. Lett. **58** (1987) 97;
TPC/2 γ Collab., Z.Phys. **C34** (1987) 1
- [38] OPAL Collab., Z. Phys. **C61** (1994) 199
- [39] DELPHI Collab., CERN-PPE/95-97
- [40] Ch. Berger and W. Wagner, Phys. Rep. **146** (1987) 1
- [41] H. Abramowicz et al., Intern. J.Mod. Phys. **A8** (1993) 1005
- [42] E. Witten, Nucl. Phys. **B120** (1977) 189
- [43] AMY Collab., Phys. Lett. **B252** (1990) 491;
AMY Collab., Phys. Lett. **B325** (1994) 248;
AMY Collab., KEK Preprint 94-184;
TOPAZ Collab., Phys. Lett. **B314** (1993) 149
- [44] M. Drees and K. Grassie, Z.Phys., **C28** (1985) 451
- [45] H. Abramowicz, K. Charchula and A. Levy, Phys. Lett. **B269** (1991) 458
- [46] M. Glück, E. Reya and A. Vogt, Z. Phys. **C53** (1992) 127
- [47] M. Glück, E. Reya and A. Vogt, Phys. Rev. **D46** (1992) 1973
- [48] P.D.B. Collins, “*An introduction to Regge theory and high energy physics.*”, Cambridge Univ. Press, UK, 1977
- [49] K. Goulianos, Phys. Rep. **101** (1983) 169
- [50] A. Donnachie and P.V. Landshoff, Phys. Lett. **B296** (1992) 227
- [51] D. Amati et al., Nuovo Cimento **26** (1962) 896
- [52] F.E. Low, Phys. Rev. **D12** (1975) 163;
S. Nussinov, Phys. Rev. Lett. **34** (1975) 1286
- [53] G. Ingelman and P. Schlein, Phys. Lett. **B152** (1985) 256
- [54] A. Donnachie and P.V. Landshoff, Phys. Lett. **B191** (1987) 309;
A. Donnachie and P.V. Landshoff, Nucl.Phys. **B303** (1988) 634
- [55] N.N. Nikolaev and B.G. Zakharov, Z. Phys. **C53** (1992) 331

- [56] J.D. Bjorken, “*Hadron Final States in Deep Inelastic Processes.*”, In *Current Induced Reactions: International Summer Institute in Theoretical Particle Physics in Hamburg 1975*, eds. J.G. Kröner, G. Kramer, and D. Schildknecht, Lecture Notes in Physics, Springer Verlag, 1976.
- [57] P. Bruni and G. Ingelman, DESY preprint DESY-93-187 (1993)
- [58] E. Berger et al., Nucl. Phys. **B286** (1987) 704
- [59] K.H. Streng, *In Proceedings of the HERA Workshop, Hamburg 1987*, ed. R.D. Peccei, p.365
- [60] A. Donnachie and P.V. Landshoff, Phys. Lett. **B285** (1992) 172
- [61] J.C. Collins, L. Frankfurt and M. Strikman, Phys. Lett. **B307** (1993) 161
- [62] UA8 Collab., Phys. Lett. **B297** (1992) 417;
UA8 Collab., Phys. Lett. **B211** (1988) 239
- [63] R. Brun et al., “*GEANT3 User’s guide.*”, CERN-DD/EE-84-1, Geneva (1987)
- [64] T. Sjöstrand, CERN-TH-6488 (1992), Comput. Phys. Commun. **82** (1994) 74
- [65] I. Abt and J.R. Smith, H1 internal reports H1-10/92-249 (1992), H1-05/93-290 (1993)
- [66] T. Sjöstrand and M. Bengtsson, Comput. Phys. Commun. **43** (1987) 367 ;
B. Andersson, G. Gustafson and T. Sjöstrand, Phys. Lett. **B94** (1980) 211;
B. Andersson et al., Phys. Rep. **97** (1983) 31
- [67] H. Cheng and T.T. Wu, Phys. Rev. Lett. **24** (1970) 1456
- [68] AFS Collab., Z. Phys. **C34** (1987) 163;
UA2 Collab., Phys. Lett. **B268** (1991) 145;
CDF Collab., Phys. Rev. **D47** (1993) 4857
- [69] UA5 Collab., Z.Phys. **C43** (1989) 357
- [70] UA1 Collab., Nucl. Phys. **B335** (1990) 261
- [71] UA1 Collab., Nucl. Phys. **B309** (1988) 405
- [72] T. Sjöstrand and M. van Zijl, Phys. Rev. **D36** (1987) 2019
- [73] H1 Collab., DESY preprint DESY-95-219
- [74] E612 Collab., Phys. Rev. **D31** (1985) 17
- [75] R. Engel, *In Proceedings of the XXIXth Rencontre de Moriond*, ed. J. Tran Thanh Van, (Editions Frontieres, 1994), p.321
- [76] A. Capella et al., Phys.Rep. **236** (1994) 227

- [77] R. Engel, Z.Phys. **C66** (1995) 203
- [78] P. Aurenche et al., Phys. Rev. **D45** (1992) 92
- [79] G. Marchesini, B.R. Webber et al., Comp. Phys. Comm. **67**(1992) 465;
G. Marchesini and B.R. Webber, Nucl. Phys. **B310** (1988) 461
- [80] UA5 Collab., Nucl. Phys. **B291** (1987) 445
- [81] J.E. Huth et al., “*Towards a standardization of jet definition.*” Fermilab-Conf-90/249-E (1990)
- [82] UA1 Collab., Phys. Lett. **B123** (1983) 115;
UA1 Collab., Phys. Lett. **B132** (1983) 223
- [83] S.D. Ellis, *In Proceedings “QCD and High Energy Hadronic Interactions”, XXVIIIth Rencontre de Moriond*, ed. J. Tran Thanh Van, (Editions Frontieres, 1993), p.235
- [84] G. Kramer and S.G. Salesch, Z. Phys. **C61** (1994) 277;
D. Bödeker, G. Kramer and S.G. Salesch, Z. Phys. **C63** (1994) 471;
M. Klasen, G. Kramer, S.G. Salesch, DESY-94-232 (1994)
- [85] L.E. Gordon and J.K. Storrow, Phys. Lett. **B291** (1994) 320
- [86] M. Greco and A. Vicini, Nucl. Phys. **B415** (1994) 386
- [87] P. Aurenche, J.-Ph. Guillet and M. Fontannaz, Phys. Lett. **B338** (1994) 98
- [88] Calculations based on ref.[87], August 1995
- [89] S.G. Salesch, “*JETSAM 3.1.*” , Program based on ref.[84], August 1995
- [90] J.D. Bjorken, “*Hard Diffraction and Deep Inelastic Scattering.*” SLAC-PUB-6477, April 1994
- [91] G. Alberi and G. Goggi, Phys. Rep. **74** (1981) 1
- [92] H1 Collab., Nucl. Phys. **B435** (1995) 3

Acknowledgements

This work would not have been possible without the effort and great support of many people.

I am deeply indebted to my supervisor Prof. B. Naroska for her assistance and constant encouragement throughout this work and for her careful reading of the manuscript.

I owe special thanks to Dr. A. Rostovtsev for giving me the idea of this analysis. His infectious enthusiasm and permanent interest in the progress of my work were of great help.

I am very grateful to Dr. G. Knies for numerous comments and suggestions. His experience in the subject and the fruitful discussions throughout the analysis were indispensable.

I wish to thank R. Engel. He patiently helped in all kinds of struggles with theory. Without the many discussions I had with him the analysis would not be complete.

I would like to thank Dr. A. Semenov for a careful reading of the manuscript and for many memorable discussions.

I thank the many members of the H1 Photoproduction and Diffraction working groups. The discussions inside the working groups made this work possible. I also appreciate the support I received from Prof. J. Dainton, Dr. M. Erdmann and Dr. S. Levonian. They provided useful advice and ideas whenever asked for.

I highly enjoyed being a member of the H1 collaboration, and I would like to thank all my colleagues for the pleasant working atmosphere they created.

It is a pleasure to express my gratitude to Prof. V. Sörgel and Prof. A. Amatuni for giving me the opportunity of working at the DESY laboratory and for a steady interest in the progress of my work.

I am very grateful to Dr. J. Feltesse for the opportunity to write this PhD thesis and for the great support during the completion of the thesis.

Finally, I wish to thank the directorates of DESY and YerPhI for giving me the opportunity to complete my PhD thesis at DESY. In particular I thank Prof. A. Wagner and Dr. G. Söhngen for their constant encouragement and the financial support.